Linear Stability Analysis of Flow in an Internally Heated Rectangular Duct

M. Uhlmann

Department of Aeronautics and Astronautics
Graduate School of Engineering
University of Kyoto
Yoshida-Honmachi, Sakyo-Ku, Kyoto 606-8501, Japan
uhlmann@kuaero.kyoto-u.ac.jp

July 13, 2004

Abstract

The linear stability of flow in a vertical rectangular duct subject to homogeneous internal heating, constant-temperature no-slip walls and a driving pressure gradient is investigated numerically. A full Chebyshev-based Galerkin method is found to be more reliable than a collocation method, both including the elimination of the pressure and the streamwise velocity from the system of equations and making use of the full symmetry properties. A classification of the mean flow—obtained as a function of Grashof and Reynolds numbers and the geometrical aspect ratio—in terms of its inflectional properties is proposed. It is found that the flow loses stability at all aspect ratios for a combination of finite thermal buoyancy and pressure forces with opposed signs. In the square duct, the unstable region coincides with the range where additional inflection lines are observed in the mean velocity profile. Unstable eigenfunctions are obtained for all basic symmetry modes and their structure can be described as slightly elongated pockets of cross-stream-vortical motion, trailing each other along the streamwise direction.

Contents

Chapter 1

Introduction

In all but a few cases the dynamics of the transition from laminar to turbulent flow are still eluding a detailed mechanistical description. On the other hand, a profound understanding of the transitional process is often of fundamental importance for technical applications where integral flow quantities such as drag or heat exchange need to be controlled precisely.

Isothermal flows. Much effort has been devoted to gain insight into the mechanism responsible for transition in unidirectional shear flows, which is now believed to develop from an instability with respect to finite-amplitude disturbances. In plane Poiseuille flow (PPF) the linearly most unstable mode [1] has been used to trace traveling wave solutions back to critical Reynolds numbers which are close to experimentally observed values [2]. In the case of plane Couette flow (PCF), which is linearly stable, it proved to be judicious to "embed" the problem within the related, more general class of rotating Taylor-Couette flow. Subsequently, approaching the limit of zero rotation enabled Nagata [3] to find three-dimensional steady solutions for the original problem of PCF at low Reynolds number, providing an upper bound for transition. In the third "canonical" shear flow case, Hagen-Poiseuille flow (HPF), which is also linearly stable, no non-trivial steady solution has so far been discovered, albeit much current interest [4].

The above mentioned cases are either planar or axisymmetric and, therefore, the base flow is one-dimensional. In practice, however, less idealized, spanwise bounded geometries are encountered. Those have received much less attention in the past, although they are of considerable industrial interest. In [5] the basic steady solution for developed flow in a duct with rectangular cross-section of arbitrary aspect ratio ("rectangular Poiseuille flow", RPF hereafter) is derived. It has not been until 1990 that an investigation of the linear stability of this configuration has appeared in the literature [6], presumably due to the fact that the numerical solution of the eigenvalue problem for a genuinely two-dimensional base flow was—and still is—a computationally demanding task. The authors of [6] concluded that the flow loses stability above a value for the critical aspect ratio of approximately 3.2, where the critical Reynolds number is an order of magnitude higher than in PPF. In particular, this means that the square duct case is stable to linear perturbations. These results were recently confirmed at higher numerical resolution [7]. To our knowledge, no studies of the non-linear stability of RPF have been reported so far.

Internally heated flow. In the presence of a homogeneously distributed internal heat source, the parabolic cross-stream temperature distribution leads to an inflectional velocity profile in a plane vertical channel under the Boussinesq hypothesis. In the limit of vanishing Prandtl number, the stability of the system is then entirely determined by the hydrodynamical problem. The study of this plane configuration has shown that the inflectional base flow does lead to a supercritical bifurcation, giving rise to two-dimensional states which in turn are linearly unstable to further three-dimensional perturbations [8]. It should be noted that, on the contrary, in the cases of PCF and PPF the velocity profile lacks inflection points and the respective bifurcations are subcritical. In the subcritical situation it can then be very difficult to track the non-linear problem since the nature of the solution tends to change abruptly near the bifurcation point, and a reasonable initial guess for the iterative method of solving the non-linear problem cannot be readily provided (cf. [3]). From this past experience, it can be expected that the bifurcation in the case of internally heated flow in a rectangular duct ("heated rectangular Poiseuille flow", HRPF hereafter) will be of supercritical nature and that the established methods of non-linear analysis will be tractable.

Present objective. The objective of the present study is to investigate the linear stability of flow in a rectangular duct in the presence of an internal heat source. It will be shown that the modification of the mean flow which is thereby induced makes the flow linearly unstable at all aspect ratios for sufficiently high values of the Grashof number and the Prandtl number.

Outline. The present report is organized as follows. In chapter §2 the formulation of the problem and its geometry are given, followed by a detailed account of the mean flow characteristics, particularly in terms of inflectional properties. The linear stability problem is formulated and its symmetry properties are discussed. The numerical solution method is presented in §3, where both a collocation and a Galerkin technique are compared and an extensive validation study is documented. In §4 the results of our computations are presented and discussed before concluding with §5.

Chapter 2

Mathematical formulation

We are considering the flow in a duct with rectangular cross-section and infinite streamwise extension. The cartesian coordinates are (x, y, z) with x being the streamwise direction and the corresponding normal vectors are $\mathbf{i}$, $\mathbf{j}$, $\mathbf{k}$ with the origin located in the center of the duct (cf. figure 2.1). The flow domain is $\Omega = \mathbb{R} \times [-\hat{b}, \hat{b}] \times [-\hat{c}, \hat{c}]$. Gravity acts in the negative streamwise direction, i.e. $\hat{\mathbf{g}} = -\hat{g}\mathbf{i}$. The aspect ratio $A = \hat{c}/\hat{b}$ will take the following values: $0 \leq 1/A \leq 1$; the inferior limit corresponds to plane Poiseuille flow (for finite $\hat{b}$) and the upper limit to the flow in a square duct.

In the range of validity of the Boussinesq approximation, the equations of motion take the following form:

$$\begin{aligned} \partial_{\hat{t}}\hat{\mathbf{u}} + (\hat{\mathbf{u}} \cdot \hat{\nabla})\hat{\mathbf{u}} &= -\frac{1}{\hat{\rho}}\hat{\nabla}\hat{p} + \hat{g}\hat{\alpha}\hat{T}\mathbf{i} + \hat{\nu}\hat{\nabla}^2\hat{\mathbf{u}}\,, &\text{(2.1a)}\\ \hat{\nabla} \cdot \hat{\mathbf{u}} &= 0\,, &\text{(2.1b)}\\ \partial_{\hat{t}}\hat{T} + (\hat{\mathbf{u}} \cdot \hat{\nabla})\hat{T} &= \hat{\kappa}\hat{\nabla}^2\hat{T} + \hat{q}\,, &\text{(2.1c)} \end{aligned}$$

where $\hat{\mathbf{u}}$ is the velocity vector, $\hat{\rho}$ the reference fluid density, $\hat{p}$ the pressure, $\hat{\alpha}$ the coefficient of thermal expansion, $\hat{T}$ the temperature variation w.r.t. some reference temperature, $\hat{\nu}$ the kinematic viscosity, $\hat{\kappa}$ the thermal conductivity and $\hat{q}$ the volume strength of a homogeneous internal heat source (i.e. $\hat{q}$ is constant in space and time). All variables with a superposed ˆ are dimensional quantities. The boundary conditions are homogeneous Dirichlet for velocity and temperature.

2.1 Non-dimensional form

We define the length, time, velocity, temperature and pressure scales as follows:

$$\hat{b}, \quad \frac{\hat{b}^2}{\hat{\nu}}, \quad \frac{\hat{\nu}}{\hat{b}}, \quad \frac{\hat{q}\hat{b}^2}{2\hat{\kappa}Gr}, \quad \frac{\hat{\rho}\hat{\nu}^2}{\hat{b}^2}\,, \tag{2.2}$$

where we have introduced the Grashof number

$$Gr = \frac{\hat{g}\hat{\alpha}\hat{q}\hat{b}^5}{2\hat{\nu}^2\hat{\kappa}}\,. \tag{2.3}$$

Let us further define the Prandtl number

$$Pr = \frac{\hat{\nu}}{\hat{\kappa}}\,, \tag{2.4}$$

and the Reynolds number as

$$Re = \frac{\hat{U}_{max}\hat{b}}{\hat{\nu}}\,, \tag{2.5}$$

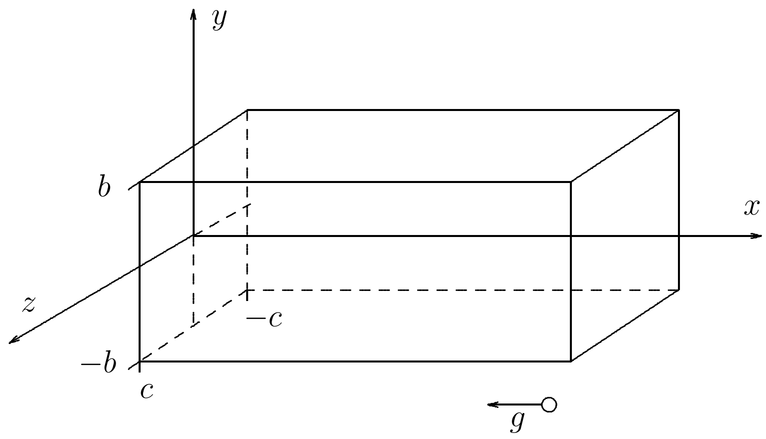

Figure 2.1: Schematic of the rectangular duct configuration. The flow domain is $\Omega = \mathbb{R} \times [-b, b] \times [-c, c]$ with $\mathbf{x} = (x, y, z) \in \Omega$. Note that gravity acts in the negative x-direction, i.e. $\mathbf{g} = -g\mathbf{i}$.

where $\hat{U}_{max}$ is the maximum velocity obtained in isothermal flow ($Gr = 0$) flow driven by the mean streamwise pressure gradient

$$\partial_{\hat{x}}\hat{\bar{p}} = -\frac{\hat{\rho}\hat{\nu}\hat{U}_{max}\,\chi(A)}{4\hat{b}^2 A}\,, \tag{2.6}$$

or, in non-dimensional form:

$$\partial_x \bar{p} = -Re\frac{\chi(A)}{4A}\,. \tag{2.7}$$

As explained in § A, the function $\chi(A)$ represents the influence of the aspect ratio upon the mean wall shear integral in isothermal flow. It needs to be evaluated numerically in order to be useful and can be considered as a tabulated function.

Substituting the scales (2.2) and the definitions of the non-dimensional parameters into (2.1), the system of equations can be written in non-dimensional form as follows:

$$\partial_t \mathbf{u} + (\mathbf{u}\cdot\nabla)\mathbf{u} = -\nabla p + T\mathbf{i} + \nabla^2\mathbf{u}\,, \tag{2.8a}$$

$$\nabla\cdot\mathbf{u} = 0\,, \tag{2.8b}$$

$$\partial_t T + (\mathbf{u}\cdot\nabla)T = \frac{1}{Pr}\nabla^2 T + \frac{2Gr}{Pr}\,. \tag{2.8c}$$

2.2 Mean flow field

Here we are concerned with finding the steady laminar base flow field. We assume that the velocity and the temperature have the form $\mathbf{u} = \mathbf{i}\,\bar{U}(y,z)$, $T = \bar{T}(y,z)$, whereby all temporal and convective terms vanish and the continuity equation is automatically satisfied. Therefore, these solutions are governed by the following two equations:

$$(\partial_{yy} + \partial_{zz})\bar{U} = -\bar{T} - Re\,\frac{1}{4A}\,\chi(A)\,, \tag{2.9a}$$

$$(\partial_{yy} + \partial_{zz})\bar{T} = -2\,Gr\,, \tag{2.9b}$$

together with the boundary conditions

$$\bar{U}(y=\pm 1) = \bar{U}(z=\pm A) = 0\,, \quad \bar{T}(y=\pm 1) = \bar{T}(z=\pm A) = 0\,. \tag{2.10}$$

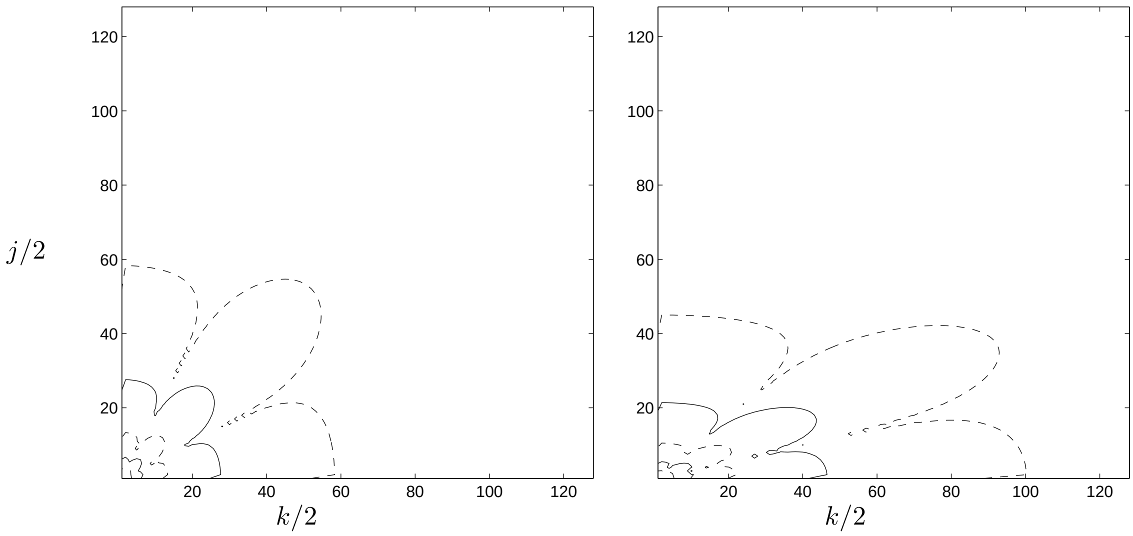

Figure 2.2: Iso-contours of the two-dimensional Chebyshev power-spectral density of the even coefficients of the mean velocity profile expanded as: $\bar{U} = \sum_{j=0}^{256} \sum_{k=0}^{256} \bar{U}_{jk} T_j(y) T_k(z)$. The mean profile corresponds to $A = 1$, $Gr = 0$ (left) and $A = 5$, $Gr = 0$ (right). The values of the contours indicate $\log(\bar{U}_{jk}^2 / \max(\bar{U}_{jk}^2)) = \{-20, -16, -12, -8, -4\}$. The maximum value is located at the origin of the graph in both cases.

A	1	2	3	4	5	10	20	30
U_b/Re	0.47704	0.50206	0.53658	0.56380	0.58310	0.62465	0.64566	0.65266
$-\dfrac{\mathrm{d}\bar{p}}{\mathrm{d}x}\dfrac{1}{Re}$	3.39345	2.19545	2.03778	2.00774	2.00160	2.00000	2.00000	2.00000

Table 2.1: Mean flow characteristics in the isothermal case: mean bulk velocity U_b and non-dimensional mean pressure-gradient $\mathrm{d}\hat{p}/\mathrm{d}x$ as a function of the aspect ratio A. These values were obtained by means of Chebyshev-Galerkin inversion of the Laplace operator and using 256 modes in both directions. The agreement with reference [6] is complete.

It can be seen that the mean temperature is obtained independently from the mean velocity profile by means of a Poisson equation with constant right-hand-side (analogous to the mean velocity in isothermal flow). The velocity obeys a Poisson equation with the right-hand-side being a function of the spatially varying mean temperature.

The solution for $\bar{U}$ and $\bar{T}$ is obtained numerically by inverting the two-dimensional Laplace operator for a full Chebyshev-Galerkin approximation with a modified basis due to Shen [9]. This method has spectral convergence and reduced roundoff errors. The mean profiles were pre-computed and stored using 256×256 modes, which is more than sufficient as can be seen by inspection of the two-dimensional spectral energy-density plots in figures 2.2-2.3. In these cases, approximately 40 modes (i.e. 20 even polynomials) are necessary to capture contributions down to an order of 10^{-12}.

2.2.1 Mean flow in the isothermal case ($Gr = 0$)

This case corresponds to the one studied in reference [6]. The mean flow characteristics are given here for completeness and to demonstrate the agreement with the former study in [6].

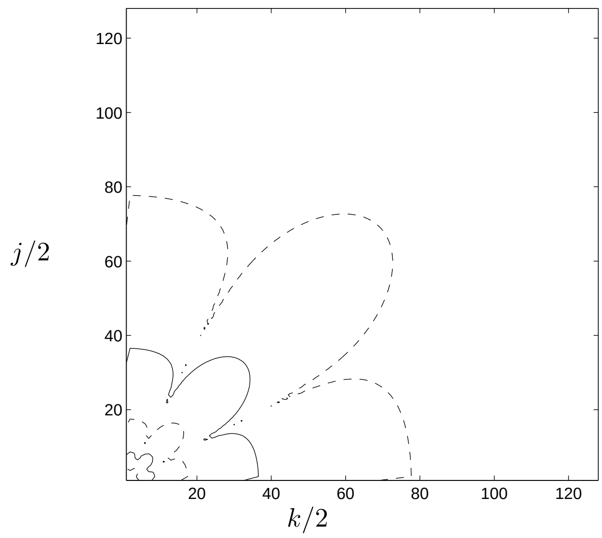

Figure 2.3: As figure 2.2, but the mean profile corresponds to $A = 1$, $Gr = 3000$, $Re = -400$.

Let us define the bulk velocity as follows:

$$U_b = \frac{1}{4A}\int_{-1}^{+1}\int_{-A}^{A}\bar{U}(y,z)\mathrm{d}y\,\mathrm{d}z\,. \tag{2.11}$$

For different aspect ratios the bulk velocity and the mean streamwise pressure gradient are listed in table 2.1. For the purpose of comparison, both quantities are normalized by the Reynolds number. Figure 2.4 shows the corresponding variation. The pressure gradient rapidly approaches its asymptotic value of 2 whereas the bulk velocity goes slowly towards 2/3 when increasing the aspect ratio A.

A further characteristic of the mean profile with relevance to stability analysis is the existence of inflection points. While the determination of an inflection point is clear in one dimension it needs further definition in the two-dimensional case. Here we will adopt the definition of reference [10]: we call inflection points those locations where the second derivative of a scalar in the direction of its gradient is zero, viz.

$$\frac{\mathrm{d}^2\bar{U}}{\mathrm{d}\mathbf{n}^2} = 0 \quad . \tag{2.12}$$

The unit vector is defined as $\mathbf{n} = \nabla\bar{U}/|\nabla\bar{U}|$. The figure 2.5 shows the zero-valued contour of (2.12) for the square duct. It can be observed that inflectional curves with elliptic shape can be found in each of the four corner regions. This becomes more obvious when looking at a profile of the mean velocity along the diagonal of the domain (figure 2.6) which clearly shows inflection points. By comparison, a simple cross-section of the mean velocity along one of the symmetry lines is very similar to a parabolic (plane Poiseuille) profile (cf. figure 2.6) and, hence, free from inflection points.

2.2.2 Mean flow with internal heat source

The integral over the cross section of the equation of the mean velocity leads to:

$$\frac{\Phi(\bar{U})}{4A} = -T_b - \frac{Re}{4A}\chi(A) \quad , \tag{2.13}$$

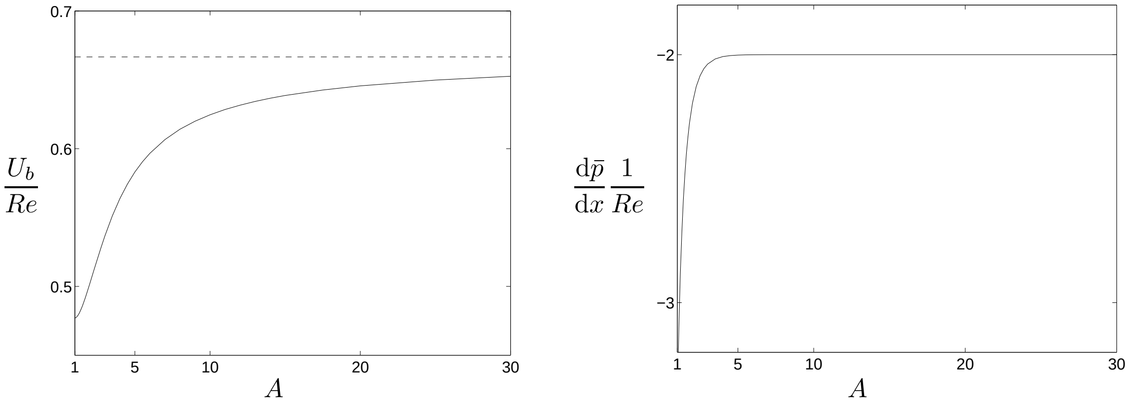

Figure 2.4: Bulk velocity U_b (left) and non-dimensional mean pressure-gradient $\mathrm{d}\hat{p}/\mathrm{d}x$ (right) as a function of the aspect ratio A for the isothermal case.

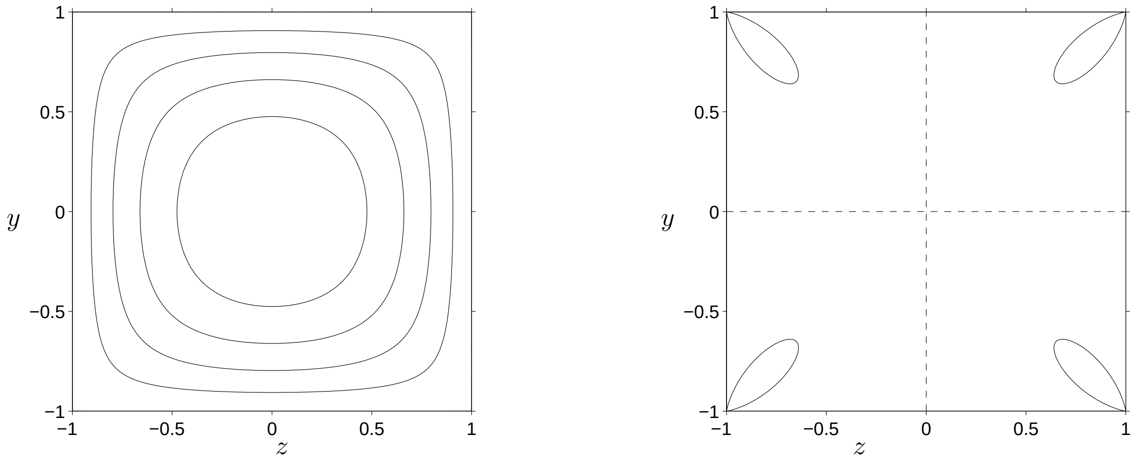

Figure 2.5: Isothermal case ($Gr = 0$). Isocontours of the mean velocity $\bar{U}$ (left) at values $\bar{U}/U_{max} = 0 : 0.2 : 1$; isocontours of $\mathrm{d}^2\bar{U}/\mathrm{d}\mathbf{n}^2 = 0$ (right) indicating inflectional lines in the corner regions.

where we have defined the bulk temperature

$$T_b = \frac{1}{4A} \int_{-1}^{+1} \int_{-A}^{A} \bar{T}(y, z) \mathrm{d}y \, \mathrm{d}z \,, \tag{2.14}$$

and the mean wall-stress integral

$$\Phi(\bar{U}) = \int_{-A}^{+A} \left[\partial_y \bar{U}\right]_{y=-1}^{y=+1} \mathrm{d}z + \int_{-1}^{+1} \left[\partial_z \bar{U}\right]_{z=-A}^{z=+A} \mathrm{d}y \,. \tag{2.15}$$

The bulk temperature is a linear function of the Grashof number and varies with the aspect ratio in the same way as the bulk velocity in the isothermal case (cf. figure 2.4).

Figure 2.7 shows the mean flow and the corresponding inflection curves for the case with $A = 1$, $Re = -450$, $Gr = 4000$. It can be seen that reverse flow occurs and that—in addition to the previously seen inflection curves in each corner—various new inflection curves appear around the central "cone" and along the lateral "ridges" of the mean profile.

2.2.2.1 Inflectional properties

Since the shape of the mean flow changes quite considerably in (Gr, Re, A)-parameter space, we propose two quantitative criteria for its classification w.r.t. inflectional properties.

Firstly, we compute the sum of the arclengths of all the inflection curves for a given mean flow and then plot it versus the parameter values. This quantity is shown for the square channel ($A = 1$) and for $A = 5$ in figure 2.8. It can be seen that in both cases large changes occur along two straight lines.

Secondly, we determine the number of disjoint inflection curves for a given mean profile. Except for some degenerate cases this discrete quantity allows to determine the appearance of additional inflectional properties for a given combination of parameters. Figure 2.9 shows a map of the number of inflection curves for $A = 1$ and $A = 5$.

The parameter range chosen for the presentation of figures 2.8 and 2.9 only includes the second quadrant of the (Gr, Re)-plane. This is because in the first and third quadrant both parameters have the same sign and therefore bouyancy and pressure gradient terms have the same direction and no additional inflection properties can be generated. In the fourth quadrant results are symmetric w.r.t. the origin of the (Gr, Re)-plane.

As we have seen in the two graphs, the region of additional inflection curves is bounded by the axis $Re = 0$ and an inclined line through the origin ($Gr = a \cdot Re$) with a slope of $a \approx -5.7$ ($A = 1$), $a \approx -0.8$ ($A = 4$) and $a \approx -0.63$ ($A = 5$) respectively. This should be compared to a value of $a = -2$ in the case of plane channel flow, as studied in reference [8].

Figure 2.9 also indicates the region in (Gr, Re)-space where reverse flow is obtained. This region is limited by the following approximate bounds:

$$\begin{array}{ll} -7.7 \cdot Re \leq Gr \leq -60 \cdot Re & (A = 1) \\ -2.4 \cdot Re \leq Gr \leq -20 \cdot Re & (A = 5) \end{array} \tag{2.16}$$

which should be compared to the (analytic) bounds for the case of plane channel flow:

$$-2.4 \cdot Re \leq Gr \leq -3 \cdot Re \quad \text{(plane)} \,. \tag{2.17}$$

The bounds of the region were additional inflection lines appear will be useful for our discussion of stability results in §4.

2.3 Linear Perturbation equations

We first introduce a decomposition of the velocity, the pressure and the temperature into mean (steady, two-/one-dimensional) and perturbation parts, viz.

$$\mathbf{u}(\mathbf{x},t) = \bar{\mathbf{U}}(y,z) + \mathbf{u}'(\mathbf{x},t) = \mathbf{i}\,\bar{U}(y,z) + \mathbf{u}'(\mathbf{x},t)\,, \tag{2.18a}$$

$$p(\mathbf{x},t) = p_0 + \frac{\mathrm{d}\bar{p}}{\mathrm{d}x}\cdot x + p'(\mathbf{x},t)\,. \tag{2.18b}$$

$$T(\mathbf{x},t) = \bar{T}(y,z) + \theta'(\mathbf{x},t)\,. \tag{2.18c}$$

Substituting the above decomposition into the system of equations (2.8), using the equations for the mean velocity and temperature (2.9) and neglecting the non-linear terms $(\mathbf{u}'\cdot\nabla)\mathbf{u}'$ and $(\mathbf{u}'\cdot\nabla)\theta'$, we obtain the following system of equations, valid for small amplitude perturbations:

$$\partial_t\mathbf{u}' + (\bar{\mathbf{U}}\cdot\nabla)\mathbf{u}' + (\mathbf{u}'\cdot\nabla)\bar{\mathbf{U}} = -\nabla p' + \nabla^2\,\mathbf{u}' + \theta'\mathbf{i}\,, \tag{2.19a}$$

$$\nabla\cdot\mathbf{u}' = 0\,, \tag{2.19b}$$

$$\partial_t\theta' + (\bar{\mathbf{U}}\cdot\nabla)\theta' + (\mathbf{u}'\cdot\nabla)\bar{T} = \frac{1}{Pr}\nabla^2\,\theta'\,, \tag{2.19c}$$

or after evaluation of the advection terms:

$$\partial_t\mathbf{u}' + \bar{U}\partial_x\mathbf{u}' + (v'\partial_y\bar{U} + w'\partial_z\bar{U})\mathbf{i} = -\nabla p' + \nabla^2\,\mathbf{u}' + \theta'\mathbf{i}\,, \tag{2.20a}$$

$$\nabla\cdot\mathbf{u}' = 0\,. \tag{2.20b}$$

$$\partial_t\theta' + \bar{U}\partial_x\theta' + v'\partial_y\bar{T} + w'\partial_z\bar{T} = \frac{1}{Pr}\nabla^2\,\theta'\,, \tag{2.20c}$$

The boundary conditions are again no-slip and constant temperature for the perturbations at the four walls, viz.

$$\mathbf{u}'(y=\pm1) = \mathbf{u}'(z=\pm A) = 0\,, \qquad \theta'(y=\pm1) = \theta'(z=\pm A) = 0\,. \tag{2.21}$$

2.4 Normal mode analysis

We consider perturbations which are streamwise travelling waves with exponential growth in time, viz.

$$\mathbf{q}'(\mathbf{x},t) = \Re\left\{\mathbf{q}(y,z)\cdot\exp(I\alpha(x-ct))\right\}\,, \tag{2.22}$$

with the variable vector*:

$$\mathbf{q} = \begin{pmatrix} u \\ v \\ w \\ p \\ \theta \end{pmatrix} \quad . \tag{2.23}$$

Here α is a real streamwise wavenumber, c is the complex phase velocity and $I = \sqrt{-1}$. $\Re(c)$ is the streamwise propagation velocity of the travelling wave and $\alpha\Im(c)$ is the temporal growth rate of the perturbation. Therefore, $\Im(c) > 0$ corresponds to an unstable (amplified) perturbation and $\Im(c) < 0$ to a stable (damped) perturbation; perturbations with $\Im(c) = 0$ are neutrally stable. Please note that with the present viscous scaling (cf. reference quantities 2.2) the non-dimensional time t, and consequently the complex phase velocity c, differ by a factor of Re from the "outer scaling" which is often used in studies of the isothermal case (cf. [6]).

*The symbols for the coefficients of the perturbation components are the same as the ones for the full fields (except for the temperature which otherwise would coincide with the usual symbol for Chebyshev polynomials). However, this should not lead to any confusion in the following because of the context.

Upon substitution of (2.22) into (2.20), the perturbation equations take the following form:

$$\begin{aligned}
I\alpha c\, u &= \left[I\alpha\bar{U} + \alpha^2 - \partial_{yy} - \partial_{zz}\right] u + I\alpha\, p + (\partial_y\bar{U})\, v + (\partial_z\bar{U})\, w - \theta\,, && (2.24a)\\
I\alpha c\, v &= \left[I\alpha\bar{U} + \alpha^2 - \partial_{yy} - \partial_{zz}\right] v + \partial_y\, p\,, && (2.24b)\\
I\alpha c\, w &= \left[I\alpha\bar{U} + \alpha^2 - \partial_{yy} - \partial_{zz}\right] w + \partial_z\, p\,, && (2.24c)\\
0 &= I\alpha\, u + \partial_y\, v + \partial_z\, w\,, && (2.24d)\\
Pr\, I\alpha c\, \theta &= \left[I\alpha\bar{U}Pr + \alpha^2 - \partial_{yy} - \partial_{zz}\right] \theta + Pr(\partial_y\bar{T})\, v + Pr(\partial_z\bar{T})\, w\,. && (2.24e)
\end{aligned}$$

The boundary conditions are expressed as:

$$\underline{y = \pm 1}: \quad u=0, \quad v=0, \quad w=0, \quad \theta=0, \qquad \underline{z = \pm A}: \quad u=0, \quad v=0, \quad w=0, \quad \theta=0. \tag{2.25}$$

It should be noted that no boundary conditions are necessary for the pressure.

2.5 Symmetries

The system of linear equations given by (2.24) only admits solutions with certain symmetries. Taking into account that the base velocity and temperature profiles $\bar{U}$, $\bar{T}$ both have even parity in both coordinate directions y and z, the five equations (2.24) lead to the following equations for the parity of pressure, streamwise velocity and temperature:

$$\begin{aligned}
\mathcal{P}(u) &= [\mathcal{P}_y(v)^{-1}, \mathcal{P}_z(v)] + [\mathcal{P}_y(w), \mathcal{P}_z(w)^{-1}] + \mathcal{P}(\theta) && (2.26a)\\
\mathcal{P}(p) &= [\mathcal{P}_y(v)^{-1}, \mathcal{P}_z(v)] && (2.26b)\\
\mathcal{P}(p) &= [\mathcal{P}_y(w), \mathcal{P}_z(w)^{-1}] && (2.26c)\\
\mathcal{P}(u) &= [\mathcal{P}_y(v)^{-1}, \mathcal{P}_z(v)] + [\mathcal{P}_y(w), \mathcal{P}_z(w)^{-1}] && (2.26d)\\
\mathcal{P}(\theta) &= [\mathcal{P}_y(v)^{-1}, \mathcal{P}_z(v)] + [\mathcal{P}_y(w), \mathcal{P}_z(w)^{-1}] && (2.26e)
\end{aligned}$$

In our notation, $\mathcal{P}(\phi)$ designates the parity vector of the variable ϕ, and $\mathcal{P}_x(\phi)$ the parity of the x-component of the variable ϕ; $\mathcal{P}_x(\phi)^{-1}$ is used to express the opposite parity of $\mathcal{P}_x(\phi)$.

In order for the pressure to be consistent with both equations (2.26b) and (2.26c), solutions for velocity components v and w need to fulfill the following two requirements:

$$\begin{aligned}
\mathcal{P}_y(v)^{-1} &= \mathcal{P}_y(w)\,, && (2.27a)\\
\mathcal{P}_z(v) &= \mathcal{P}_z(w)^{-1}\,. && (2.27b)
\end{aligned}$$

These can only be met by four combinations of odd/even parity of v, w. Furthermore, the fulfillment of (2.27) leads to the symmetry of the streamwise velocity through (2.26d). Because of (2.26e), both equations (2.26d) and (2.26a) are consistent and temperature, streamwise velocity and pressure have identical parities. As a final result, the following four solution modes are obtained:

$$\begin{array}{rlllll}
\text{I:} & u(\text{o,e}) & v(\text{e,e}) & w(\text{o,o}) & p(\text{o,e}) & \theta(\text{o,e})\\
\text{II:} & u(\text{o,o}) & v(\text{e,o}) & w(\text{o,e}) & p(\text{o,o}) & \theta(\text{o,o})\\
\text{III:} & u(\text{e,e}) & v(\text{o,e}) & w(\text{e,o}) & p(\text{e,e}) & \theta(\text{e,e})\\
\text{IV:} & u(\text{e,o}) & v(\text{o,o}) & w(\text{e,e}) & p(\text{e,o}) & \theta(\text{e,o})
\end{array} \tag{2.28}$$

In the above table—as an example—the notation (o,e) stands for an odd parity in y and an even parity in z. Please note that these modes are the same as in reference [6] for the hydrodynamic part.

2.6 Elimination of pressure and streamwise velocity

The system (2.24) can be reduced to three equations by solving the continuity equation (2.24d) for u, solving the streamwise momentum equation (2.24a) for p and substituting both into (2.24b) and (2.24c). This leads to the following system for the unknowns v, w and θ:

$$
\begin{aligned}
&\left[I\alpha\bar{U}+\alpha^2-2\partial_{yy}-\partial_{zz}-\frac{I\bar{U}}{\alpha}\partial_{yy}+\frac{1}{\alpha^2}\partial_{yyyy}+\frac{1}{\alpha^2}\partial_{zzyy}+\frac{I}{\alpha}(\partial_{yy}\bar{U})\right]v-\left[\frac{I}{\alpha}\partial_y\right]\theta \\
&\quad+\left[-\frac{I(\partial_y\bar{U})}{\alpha}\partial_z-\frac{I\bar{U}}{\alpha}\partial_{zy}-\partial_{zy}+\frac{\partial_{zyyy}}{\alpha^2}+\frac{\partial_{zzzy}}{\alpha^2}+\frac{I(\partial_{zy}\bar{U})}{\alpha}+\frac{I(\partial_z\bar{U})}{\alpha}\partial_y\right]w \;= \\
&\qquad\qquad c\left[-\frac{I}{\alpha}\partial_{yy}+I\alpha\right]v+c\left[-\frac{I}{\alpha}\partial_{zy}\right]w\,, \qquad (2.29a)
\end{aligned}
$$

$$
\begin{aligned}
&\left[I\alpha\bar{U}+\alpha^2-\partial_{yy}-2\partial_{zz}-\frac{I\bar{U}}{\alpha}\partial_{zz}+\frac{1}{\alpha^2}\partial_{zzyy}+\frac{1}{\alpha^2}\partial_{zzzz}+\frac{I}{\alpha}(\partial_{zz}\bar{U})\right]w-\left[\frac{I}{\alpha}\partial_z\right]\theta \\
&\quad+\left[-\frac{I(\partial_z\bar{U})}{\alpha}\partial_y-\frac{I\bar{U}}{\alpha}\partial_{zy}-\partial_{zy}+\frac{\partial_{zyyy}}{\alpha^2}+\frac{\partial_{zzzy}}{\alpha^2}+\frac{I(\partial_{zy}\bar{U})}{\alpha}+\frac{I(\partial_y\bar{U})}{\alpha}\partial_z\right]v \;= \\
&\qquad\qquad c\left[-\frac{I}{\alpha}\partial_{zz}+I\alpha\right]w+c\left[-\frac{I}{\alpha}\partial_{zy}\right]v\,, \qquad (2.29b)
\end{aligned}
$$

$$
\begin{aligned}
&\left[I\alpha\bar{U}Pr+\alpha^2-\partial_{yy}-\partial_{zz}\right]\theta+\left[Pr(\partial_y\bar{T})\right]v+\left[Pr(\partial_z\bar{T})\right]w \;= \\
&\qquad\qquad c\left[Pr\,I\alpha\right]\theta\,. \qquad (2.29c)
\end{aligned}
$$

The above system contains fourth derivatives of v in the direction y, and of w in the direction z; otherwise the highest derivatives are of second order. Therefore, the appropriate boundary conditions are the following:

$$
\underline{y=\pm1}:\quad v=0,\quad w=0,\quad \partial_y v=0,\quad \theta=0,\qquad\qquad \underline{z=\pm A}:\quad v=0,\quad w=0,\quad \partial_z w=0,\quad \theta=0. \qquad (2.30)
$$

Equations (2.29a) and (2.29b) are equivalent to the formulation used for the purely hydrodynamical case considered in reference [6].

2.7 Poloidal-toroidal decomposition

The poloidal-toroidal decomposition (cf. appendix F) can be used alternatively. However, since it leads to a sixth-order differential system it has not been considered further in the present study.

2.8 Limit of vanishing Prandtl number

The limit of vanishing Prandtl number has been considered in the past in the framework of plane Poiseuille flow [8]. Although we do not restrict our present study to this limit, we will consider it below for the purpose of validation.

First, we observe that as $Pr \to 0$, the mean field (2.9) is not affected. Secondly, we notice that the equation for temperature (2.8c) reduces to the equation for the mean temperature in that limit, i.e. $T = \bar{T}$. Therefore, the problem becomes purely hydrodynamic and in that case we will only need to consider equations (2.29a-2.29b), i.e. the analysis becomes analogous to the one carried out in reference [6] except for a different basic velocity profile.

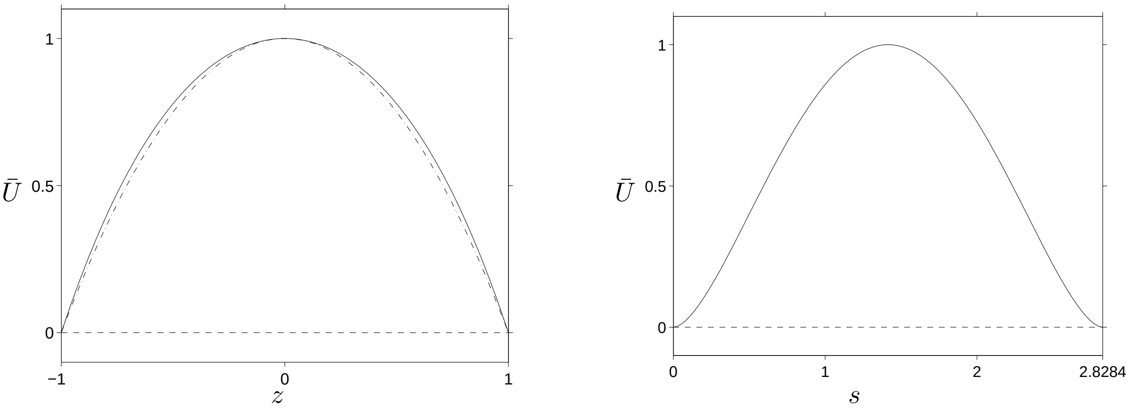

Figure 2.6: Isothermal case ($Gr = 0$), $A = 1$. Mean velocity profile $\bar{U}$ along the symmetry axis $y = 0$ (left). The chain-dotted line corresponds to the parabola $1 - z^2$. The graph on the right shows the mean velocity profile along the corner bi-sector as a function of $s = \sqrt{(y+1)^2 + (z+1)^2}$, indicating the inflectional characteristic of the mean profile in that region.

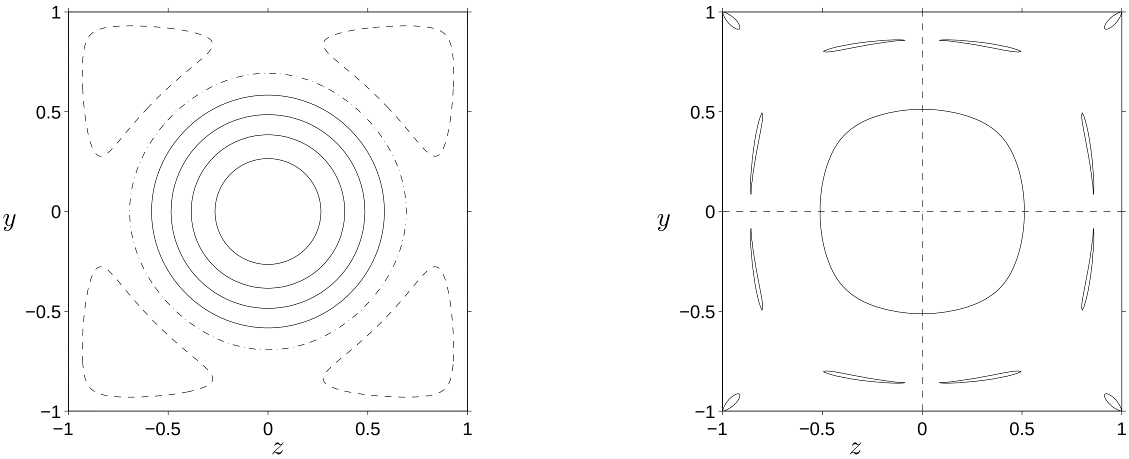

Figure 2.7: Case: $A = 1$, $Re = -450$, $Gr = 4000$. Isocontours of the mean velocity $\bar{U}$ (left) at values $\bar{U}/U_{max} = -1 : 0.2 : 1$; negative values are plotted as - - - - , the zero value is plotted as —·— . Isocontours of $\mathrm{d}^2\bar{U}/\mathrm{d}\mathbf{n}^2 = 0$ (right) indicating inflectional lines in the corner regions as well as around the central cone and on the ridges of the negative velocity zones near the walls.

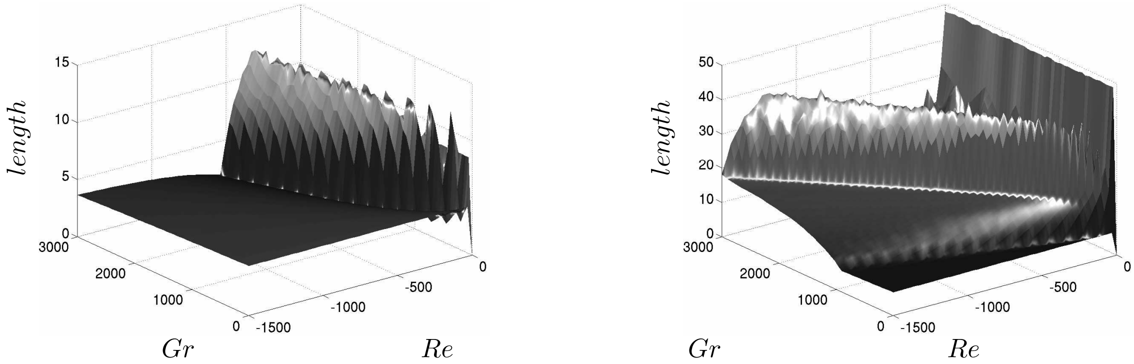

Figure 2.8: Sum of the arclength of all inflection curves as a function of Grashof and Reynolds number for $A = 1$ (left) and $A = 5$ (right).

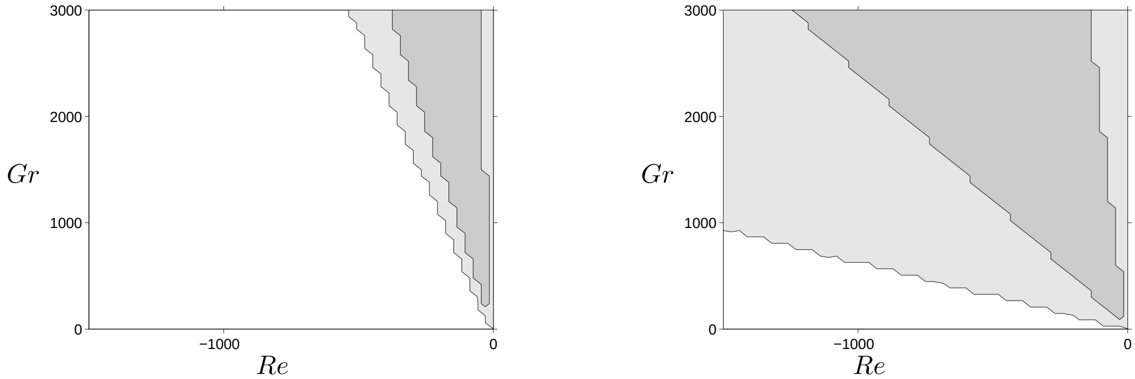

Figure 2.9: Map of the number of disjoint inflection curves as a function of the Grashof and Reynolds number: $A = 1$ (left), $A = 5$ (right). In the white area, four curves are detected; in the lightly shaded area, more than four curves are detected. The dark shading indicates the presence of reverse flow.

Chapter 3

Numerical approach

3.1 Mapping

In order to be able to use classical orthogonal polynomials, we map our rectangular cross-section to a square by introducing the following linear mapping function (rescaling):

$$\eta(z) = \frac{z}{A} \qquad (-1 \leq \eta \leq +1)\,. \tag{3.1}$$

Since we have

$$\frac{\mathrm{d}\eta}{\mathrm{d}z} = \frac{1}{A}\,, \quad \frac{\mathrm{d}^n\eta}{\mathrm{d}z^n} = 0 \quad \forall\, n \geq 2\,, \tag{3.2}$$

derivatives with respect to z can be expressed as:

$$\frac{\partial^n u(\eta(z),\ldots)}{\partial z^n} = \frac{\partial^n u(\eta,\ldots)}{\partial \eta^n} \cdot \left(\frac{\mathrm{d}\eta}{\mathrm{d}z}\right)^n \quad \forall\, n = 1,\ldots\,. \tag{3.3}$$

3.2 Spatial discretization

In the following we are concerned with the discretization of the system of two fourth order equations for v and w given by (2.29). Both methods which are to be presented are based upon expansions in terms of modified Chebyshev polynomials. These basis functions satisfy the symmetries of the governing equations (cf. 2.28) and its boundary conditions (2.30) identically. Thereby we obtain the smallest possible size for the final algebraic system and eliminate spurious eigenvalues which often appear as a consequence of explicit high-order boundary conditions, especially when using the tau method [11, 12].

3.2.1 Modified Chebyshev basis

As end-point conditions we need either one of the following: unconstrained, homogeneous Dirichlet, homogeneous Dirichlet and Neumann. It is straightforward to enforce several conditions simultaneously at the end-points by linear combination of Chebyshev polynomials; e.g. for two conditions and even parity the following *ansatz* can be made:

$$\phi_i(x) = T_{2i}(x) + a \cdot T_0(x) + b \cdot T_2(x) \quad . \tag{3.4}$$

Then, requiring that $\phi_i(\pm 1) = 0$ and $\phi_i'(\pm 1) = 0$ and using the well-known Chebyshev identities $T_i(\pm 1) = (\pm 1)^i$ and $T_i'(\pm 1) = (\pm 1)^{i+1} \cdot i^2$ we obtain:

$$\phi_i(x) = T_{2i}(x) + (i^2 - 1)\,T_0(x) - i^2 \cdot T_2(x) \quad \forall\; i = 2, 3, \ldots \quad . \tag{3.5}$$

	unconstrained	hom. Dirichlet	hom. Dirichlet & Neumann
		$\phi_i(\pm 1) = 0$	$\phi_i(\pm 1) = \phi_i'(\pm 1) = 0$
	$i = 0, 1, 2, 3, \ldots$	$i = 1, 2, 3, \ldots$	$i = 2, 3, \ldots$
even	$T_{2i}(x)$	$T_{2i}(x) - T_0(x)$	$T_{2i}(x) + (i^2 - 1)T_0(x) - i^2 T_2(x)$
odd	$T_{2i+1}(x)$	$T_{2i+1}(x) - T_1(x)$	$T_{2i+1}(x) + \frac{i^2+i-2}{2} T_1(x) - \frac{i^2+i}{2} T_3(x)$

Table 3.1: One-dimensional basis functions $\phi_i(x)$ based upon Chebyshev polynomials $T_k(x)$ for even/odd parity and either one of the following end-point conditions: unconstrained, homogeneous Dirichlet, homogeneous Dirichlet and Neumann. Note that the lower bound for the index i changes according to the end-point condition.

Due to the fact that the number of degrees of freedom has been reduced by two while imposing two boundary conditions, the lower index bound of i is 2 in the above example.

Table 3.1 lists the six different basis functions needed in the present context. These combinations have previously been used in reference [13] in the context of the one-dimensional Orr-Sommerfeld equations. Table 3.2 sums up for each variable which condition applies in either one of the two spatial directions and helps together with table 3.1 to select the adequate basis function. The final basis function is simply the product of the one-dimensional functions. The truncated series then reads e.g.

$$v(y, z) = \sum_{i=2}^{N_y} \sum_{j=1}^{N_z} \hat{v}_{ij} \cdot \phi_i^N(y)\, \phi_j^M(\eta(z))\,, \tag{3.6}$$

and analogously for the other variables (cf. table 3.2 for the naming conventions ϕ^N etc.). One needs to take special care when assembling the discrete system because each variable has not only a different type of basis function but also a different lower index bound.

3.2.2 Collocation method

In the collocation approach, the governing equations are enforced at each of the collocation points of the numerical grid in physical space. In other words, if a continuous equation is written in operator form as

$$\mathcal{L}(u(\mathbf{x})) = 0 \quad , \tag{3.7}$$

	unconstrained ϕ^C	hom. Dirichlet ϕ^M	hom. Dirichlet & Neumann ϕ^N
$\bar{U}$, $\bar{T}$		y, z	
v		z	y
w		y	z
u, θ		y, z	
ω_x, p	y, z		

Table 3.2: Matrix of end-point conditions for the different variables appearing in the governing equations $(\bar{U}, \bar{T}, v, w, \theta)$ and for those being reconstructed in a post-processing stage after the solution of the equations (u, ω_x, p), indicating which of the basis functions of table 3.1 apply in the respective spatial direction.

then it can be discretely enforced by requiring that

$$\mathcal{L}(u(\mathbf{x}_{ij})) = 0 \qquad \forall\ i,j \quad . \tag{3.8}$$

It now remains to define adequate collocation points for our present case. Here we have chosen the Chebyshev-Gauss-Lobatto points (extrema grid) on the half-interval ($y_i, \eta_j \in [0,1]$), viz.

$$y_i = \cos\left(\frac{\pi i}{2N_y+1}\right) , \qquad \eta_j = \cos\left(\frac{\pi j}{2N_z+1}\right) , \tag{3.9}$$

and $z_j = A \cdot \eta_j$. In reference [11], a subset of the Chebyshev-Gauss points (root-grid) was used for a similar fourth order problem. Here we choose the extrema grid instead because it achieves a slightly better accumulation of points near the boundary.

The indices for the discrete representation of the three dependent variables v, w, θ and, consequently, for the two momentum equations and te temperature equation are as follows:

$$\begin{array}{lll} \underline{v,\ y\text{-momentum}}: & 2\leq i \leq N_y, & 1\leq j \leq N_z, \\ \underline{w,\ z\text{-momentum}}: & 1\leq i \leq N_y, & 2\leq j \leq N_z, \\ \underline{\theta,\ \text{temperature}}: & 1\leq i \leq N_y, & 1\leq j \leq N_z. \end{array} \tag{3.10}$$

Since the index bounds differ for the two equations, it is obvious that the cross-terms contain the variables evaluated at collocation points outside those index bounds (e.g. the y-momentum equation contains $w(y_i, z_1)$ whereas the expansion of w does not contain the index $j = 1$). Therefore, these values need to be implicitly reconstructed through the use of the respective end-point conditions. More specifically, we need to carry out operations like

$$R_y^{w\to v} \cdot w_N \cdot (R_z^{w\to v})^T = \tilde{w}_N \quad , \tag{3.11}$$

where w_N is the matrix of the values of w at its collocation points and $\tilde{w}_N$ the matrix of the values of w at the collocation points of v (i.e. those of the y-momentum equation). The transform matrix $R_y^{w\to v}$ simply deletes the values of w with $i = 1$; the transform matrix $R_z^{w\to v}$ reconstructs those with $j = 1$ by making use of the fact that $w(z = \pm A) = w'(\pm A) = 0$.

The algebraic system of equation can then be written as follows:

$$\begin{aligned} I\alpha\bar{U}_N^v \boxtimes v_N + \alpha^2 v_N - 2D_{yy}^v v_N - v_N (D_{zz}^v)^T \frac{1}{A^2} - \frac{I}{\alpha}\bar{U}_N^v \boxtimes (D_{yy}^v v_N) + \frac{1}{\alpha^2} D_{yyyy}^v v_N \\ + \frac{1}{\alpha^2 A^2} D_{yy}^v v_N (D_{zz}^v)^T + \frac{I}{\alpha}(\partial_{yy}\bar{U})_N^v \boxtimes v_N - \frac{I}{\alpha} D_y^{\theta\to v}\theta_N (R_z^{\theta\to v})^T \\ - \frac{I}{\alpha A}(\partial_y \bar{U})_N^v \boxtimes (R_y^{w\to v} w_N (D_z^{w\to v})^T) - \frac{I}{\alpha A}\bar{U}_N^v \boxtimes (D_y^{w\to v} w_N (D_z^{w\to v})^T) \\ - \frac{1}{A} D_y^{w\to v} w_N (D_z^{w\to v})^T + \frac{1}{\alpha^2 A} D_{yyy}^{w\to v} w_N (D_z^{w\to v})^T + \frac{1}{\alpha^2 A^3} D_y^{w\to v} w_N (D_{zzz}^{w\to v})^T \\ + \frac{I}{\alpha}(\partial_{yz}\bar{U})_N^v \boxtimes (R_y^{w\to v} w_N (R_z^{w\to v})^T) + \frac{I}{\alpha}(\partial_z \bar{U})_N^v \boxtimes (D_y^{w\to v} w_N (R_z^{w\to v})^T) \quad = \\ I\alpha c v_N - \frac{Ic}{\alpha} D_{yy}^v v_N - \frac{Ic}{\alpha A} D_y^{w\to v} w_N (D_z^{w\to v})^T \end{aligned} \tag{3.12a}$$

$$
\begin{aligned}
I\alpha \bar{U}^w_N \boxtimes w_N + \alpha^2 w_N - D^w_{yy} w_N - w_N (D^w_{zz})^T \frac{2}{A^2} - \frac{I}{\alpha A^2} \bar{U}^w_N \boxtimes (v_N (D^w_{zz})^T) \\
+ \frac{1}{\alpha^2 A^2} D^w_{yy} w_N (D^w_{zz})^T + \frac{1}{\alpha^2 A^4} w_N (D^w_{zzzz})^T + \frac{I}{\alpha} (\partial_{zz} \bar{U})^w_N \boxtimes w_N - \frac{I}{\alpha} R^{\theta\to w}_y \theta_N (D^{\theta \to w}_z)^T \\
- \frac{I}{\alpha} (\partial_z \bar{U})^w_N \boxtimes (D^{v\to w}_y v_N (R^{v\to w}_z)^T) - \frac{I}{\alpha A} \bar{U}^w_N \boxtimes (D^{v\to w}_y v_N (D^{v\to w}_z)^T) \\
- \frac{1}{A} D^{v\to w}_y v_N (D^{v\to w}_z)^T + \frac{1}{\alpha^2 A} D^{v\to w}_{yyy} v_N (D^{w\to v}_z)^T + \frac{1}{\alpha^2 A^3} D^{v\to w}_y v_N (D^{w\to v}_{zzz})^T \\
+ \frac{I}{\alpha} (\partial_{yz} \bar{U})^w_N \boxtimes (R^{v\to w}_y v_N (R^{v\to w}_z)^T) + \frac{I}{\alpha A} (\partial_y \bar{U})^w_N \boxtimes (R^{v\to w}_y v_N (D^{v\to w}_z)^T) \quad = \\
I\alpha c w_N - \frac{Ic}{\alpha A^2} w_N (D^w_{zz})^T - \frac{Ic}{\alpha A} D^{v\to w}_y v_N (D^{v\to w}_z)^T \qquad (3.12b)
\end{aligned}
$$

$$
\begin{aligned}
Pr\, I\alpha \bar{U}^\theta_N \boxtimes \theta_N + \alpha^2 \theta_N - D^\theta_{yy} \theta_N - \theta_N (D^\theta_{zz})^T \frac{1}{A^2} + Pr\, (\partial_y \bar{T})^\theta_N \boxtimes (R^{v\to\theta}_y v_N (R^{v\to\theta}_z)^T) \\
+ Pr\, (\partial_z \bar{T})^\theta_N \boxtimes (R^{w\to\theta}_y w_N (R^{w\to\theta}_z)^T) \quad = \\
Pr\, I\alpha c \theta_N \qquad (3.12c)
\end{aligned}
$$

Here, the $R^{v\to w}_y$ etc. are the transformation matrices from one set of collocation points to another, as described above. D_y, D_z are the collocation derivative matrices in the y and z direction, D_{yy}, D_{zz} the second derivative matrices etc. The superscript indicates at which set of collocation points an entity is evaluated: D^w_y is the y-derivative matrix for w evaluated at its own set of collocation points, $D^{v\to w}_y$ is the y-derivative matrix for v evaluated at the set of collocation points of w. v_N, w_N are matrices of the variables evaluated at their own set of collocation points, e.g. an element of v_N is defined as $(v_N)_{ij} = v(y_i, z_j)$. $\bar{U}^v_N$ is the mean flow evaluated at the set of collocation points for v, and similarly for the derivatives of $\bar{U}$ and the mean temperature $\bar{T}$. Finally, $a \boxtimes b$ is the pointwise product of the matrices a and b, i.e. if we set $c = a \boxtimes b$ then the elements are $(c)_{ij} = (a)_{ij} \cdot (b)_{ij}$ (no summation). More details of how to compute the matrices appearing in (3.12) can be found in the appendix C.

The system (3.12) can be written in the form of a generalized eigenvalue system

$$
A \cdot q_N = c\, B \cdot q_N \quad , \qquad (3.13)
$$

with q_N the variable *vector* with the following shape:

$$
q_N = \left[v(y_2, z_1), v(y_3, z_1), \dots v(y_{N_y}, z_{N_z}), w(y_1, z_2), \dots w(y_{N_y}, z_{N_z}), \theta(y_1, z_1), \dots \theta(y_{N_y}, z_{N_z}) \right]^T \quad . \qquad (3.14)
$$

A, B are square matrices of size $N_{sys} = (N_y - 1) N_z + N_y (N_z - 1) + N_y N_z$. All quantities in (3.13) are complex.

3.2.3 Galerkin method

Referring to the model problem (3.7), the Galerkin method enforces the equation in an integral sense by requiring:

$$
\int_\Omega \mathcal{L}(u(\mathbf{x}))\, \psi_{ij}(\mathbf{x})\, \mathcal{W}(\mathbf{x})\, \mathrm{d}\mathbf{x} = 0 \quad \forall\ i, j\,, \qquad (3.15)
$$

where $\mathcal{W}(\mathbf{x})$ is an appropriate weight function. In the present case the weight function is the usual Chebyshev weight, viz.

$$
\mathcal{W}(y, \eta) = W(y) \cdot W(\eta)\,, \qquad W(x) = \frac{1}{\sqrt{1 - x^2}}\,. \qquad (3.16)
$$

Additionally, in a genuine Galerkin method the so-called test functions $\psi_{ij}(\mathbf{x})$ are equal to the trial functions used for the expansion of the variables (cf. equation 3.6). This means that we test the y-momentum equation with the expansion functions of v, the z-momentum equation with the functions used for expanding w, and the temperature equation with θ's base functions, i.e. we operate as follows:

$$\int_{-1}^{+1}\int_{-1}^{+1}(2.29\text{a})\,\phi_k^N(y)\,\phi_l^M(\eta)\,W(y)\,W(\eta)\,\mathrm{d}y\mathrm{d}\eta \quad \forall\; 2\le k\le N_y\,,\quad 1\le l\le N_z\,, \tag{3.17a}$$

$$\int_{-1}^{+1}\int_{-1}^{+1}(2.29\text{b})\,\phi_k^M(y)\,\phi_l^N(\eta)\,W(y)\,W(\eta)\,\mathrm{d}y\mathrm{d}\eta \quad \forall\; 1\le k\le N_y\,,\quad 2\le l\le N_z\,, \tag{3.17b}$$

$$\int_{-1}^{+1}\int_{-1}^{+1}(2.29\text{c})\,\phi_k^M(y)\,\phi_l^M(\eta)\,W(y)\,W(\eta)\,\mathrm{d}y\mathrm{d}\eta \quad \forall\; 1\le k\le N_y\,,\quad 1\le l\le N_z\,, \tag{3.17c}$$

where it is understood that the mapping $z\to\eta$ of § 3.1 has been substituted into the equations first. The resulting system reads:

$$\begin{aligned}
&\sum_{i=2}^{N_y}\sum_{j=1}^{N_z}\hat{v}_{ij}\Big[I\alpha\mathcal{T}_{kilj}^{vv(0,0,0,0)}(\bar{U})+\alpha^2\mathcal{D}_{kilj}^{vv(0,0)}-2\mathcal{D}_{kilj}^{vv(2,0)}-\frac{1}{A^2}\mathcal{D}_{kilj}^{vv(0,2)}-\frac{I}{\alpha}\mathcal{T}_{kilj}^{vv(0,2,0,0)}(\bar{U})\\
&\qquad+\frac{1}{\alpha^2}\mathcal{D}_{kilj}^{vv(4,0)}+\frac{1}{\alpha^2A^2}\mathcal{D}_{kilj}^{vv(2,2)}+\frac{I}{\alpha}\mathcal{T}_{kilj}^{vv(2,0,0,0)}(\bar{U})\Big]+\sum_{i=1}^{N_y}\sum_{j=1}^{N_z}\hat{\theta}_{ij}\Big[-\frac{I}{\alpha}\mathcal{D}_{kilj}^{\theta v(1,0)}\Big]\\
&+\sum_{i=1}^{N_y}\sum_{j=2}^{N_z}\hat{w}_{ij}\Big[-\frac{I}{\alpha A}\mathcal{T}_{kilj}^{wv(1,0,0,1)}(\bar{U})-\frac{I}{\alpha A}\mathcal{T}_{kilj}^{wv(0,1,0,1)}(\bar{U})-\frac{1}{A}\mathcal{D}_{kilj}^{wv(1,1)}+\frac{1}{\alpha^2A}\mathcal{D}_{kilj}^{wv(3,1)}\\
&\qquad+\frac{1}{\alpha^2A^3}\mathcal{D}_{kilj}^{wv(1,3)}+\frac{I}{\alpha A}\mathcal{T}_{kilj}^{wv(1,0,1,0)}(\bar{U})+\frac{I}{\alpha A}\mathcal{T}_{kilj}^{wv(0,1,1,0)}(\bar{U})\Big]\\
&\quad=\sum_{i=2}^{N_y}\sum_{j=1}^{N_z}\hat{v}_{ij}\Big[I\alpha\mathcal{D}_{kilj}^{vv(0,0)}-\frac{I}{\alpha}\mathcal{D}_{kilj}^{vv(2,0)}\Big]\cdot c+\sum_{i=1}^{N_y}\sum_{j=2}^{N_z}\hat{w}_{ij}\Big[-\frac{I}{\alpha A}\mathcal{D}_{kilj}^{wv(1,1)}\Big]\cdot c\\
&\qquad\forall\; 2\le k\le N_y\,,\quad 1\le l\le N_z\,,
\end{aligned} \tag{3.18a}$$

$$\begin{aligned}
&\sum_{i=1}^{N_y}\sum_{j=2}^{N_z}\hat{w}_{ij}\Big[I\alpha\mathcal{T}_{kilj}^{ww(0,0,0,0)}(\bar{U})+\alpha^2\mathcal{D}_{kilj}^{ww(0,0)}-\mathcal{D}_{kilj}^{ww(2,0)}-\frac{2}{A^2}\mathcal{D}_{kilj}^{ww(0,2)}-\frac{I}{\alpha A^2}\mathcal{T}_{kilj}^{ww(0,0,0,2)}(\bar{U})\\
&\qquad+\frac{1}{\alpha^2A^4}\mathcal{D}_{kilj}^{ww(0,4)}+\frac{1}{\alpha^2A^2}\mathcal{D}_{kilj}^{ww(2,2)}+\frac{I}{\alpha A^2}\mathcal{T}_{kilj}^{ww(0,0,2,0)}(\bar{U})\Big]+\sum_{i=1}^{N_y}\sum_{j=1}^{N_z}\hat{\theta}_{ij}\Big[-\frac{I}{\alpha\,A}\mathcal{D}_{kilj}^{\theta w(0,1)}\Big]\\
&+\sum_{i=2}^{N_y}\sum_{j=1}^{N_z}\hat{v}_{ij}\Big[-\frac{I}{\alpha A}\mathcal{T}_{kilj}^{vw(0,1,1,0)}(\bar{U})-\frac{I}{\alpha A}\mathcal{T}_{kilj}^{vw(0,1,0,1)}(\bar{U})-\frac{1}{A}\mathcal{D}_{kilj}^{vw(1,1)}+\frac{1}{\alpha^2A}\mathcal{D}_{kilj}^{vw(3,1)}\\
&\qquad+\frac{1}{\alpha^2A^3}\mathcal{D}_{kilj}^{vw(1,3)}+\frac{I}{\alpha A}\mathcal{T}_{kilj}^{vw(1,0,1,0)}(\bar{U})+\frac{I}{\alpha A}\mathcal{T}_{kilj}^{vw(1,0,0,1)}(\bar{U})\Big]\\
&\quad=\sum_{i=1}^{N_y}\sum_{j=2}^{N_z}\hat{w}_{ij}\Big[I\alpha\mathcal{D}_{kilj}^{ww(0,0)}-\frac{I}{\alpha A^2}\mathcal{D}_{kilj}^{vv(0,2)}\Big]\cdot c+\sum_{i=2}^{N_y}\sum_{j=1}^{N_z}\hat{v}_{ij}\Big[-\frac{I}{\alpha A}\mathcal{D}_{kilj}^{vw(1,1)}\Big]\cdot c\\
&\qquad\forall\; 1\le k\le N_y\,,\quad 2\le l\le N_z\,.
\end{aligned} \tag{3.18b}$$

$$\sum_{i=1}^{N_y}\sum_{j=1}^{N_z}\hat{\theta}_{ij}\left[I\alpha\,Pr\,\mathcal{T}_{kilj}^{\theta\theta(0,0,0,0)}(\bar{U})+\alpha^2\mathcal{D}_{kilj}^{\theta\theta(0,0)}-\mathcal{D}_{kilj}^{\theta\theta(2,0)}-\frac{1}{A^2}\mathcal{D}_{kilj}^{\theta\theta(0,2)}\right]$$
$$+\sum_{i=2}^{N_y}\sum_{j=1}^{N_z}\hat{v}_{ij}\left[Pr\,\mathcal{T}_{kilj}^{v\theta(1,0,0,0)}(\bar{T})\right]+\sum_{i=1}^{N_y}\sum_{j=2}^{N_z}\hat{w}_{ij}\left[Pr\,\mathcal{T}_{kilj}^{w\theta(0,0,1,0)}(\bar{T})\right]$$
$$=\sum_{i=1}^{N_y}\sum_{j=1}^{N_z}\hat{\theta}_{ij}\left[Pr\,I\alpha\mathcal{D}_{kilj}^{\theta\theta(0,0)}\right]\cdot c\qquad\forall\;1\le k\le N_y\,,\quad 1\le l\le N_z\,.\tag{3.18c}$$

The Galerkin method has generated double and triple integrals of the basis functions, which are defined as follows:

$$\mathcal{D}_{kilj}^{ab(\alpha\beta)}=\int_{-1}^{+1}\phi_i^{a(\alpha)}(y)\phi_k^b(y)W(y)\mathrm{d}y\int_{-1}^{+1}\phi_j^{a(\beta)}(\eta)\phi_l^b(\eta)W(\eta)\mathrm{d}\eta\,,\tag{3.19a}$$

$$\mathcal{T}_{kilj}^{ab(\alpha\beta\gamma\delta)}(\bar{U})=\sum_{m=1}^{N_y}\sum_{n=1}^{N_\eta}\hat{U}_{mn}\underbrace{\int_{-1}^{+1}\phi_i^{a(\beta)}(y)\phi_k^b(y)\phi_m^{U(\alpha)}(y)W(y)\mathrm{d}y}_{A_{ikm}}\times\underbrace{\int_{-1}^{+1}\phi_j^{a(\delta)}(\eta)\phi_l^b(\eta)\phi_n^{U(\gamma)}(\eta)W(\eta)\mathrm{d}\eta}_{B_{jln}}\,,\tag{3.19b}$$

where a superscript in parenthesis $^{(\alpha)}$ means an order-α derivative. The superscripts outside parenthesis indicate the variable whose basis function is to be substituted, e.g. $\mathcal{D}^{vw(1,3)}$ means that inside (3.19a) $\phi^a(y)=\phi^N(y)$, $\phi^a(\eta)=\phi^M(\eta)$ and $\phi^b(y)=\phi^M(y)$, $\phi^b(\eta)=\phi^N(\eta)$ according to table 3.2. Assembly of triple matrices involving the mean temperature $\bar{T}$ is completely analogous.

The assembly of the matrices (3.19) is straightforward when using the identities given in appendix D (cf. equation D.2) and the orthogonality of the Chebyshev polynomials. However, two points need to be carefully considered.

Remark 3.2.1 The expressions for the fourth derivative are of the order $\mathcal{O}((2N+1)^7)$ which rapidly leads to overflow in a practical computation. When using the re-arrangment of the fourth derivative term as suggested in [14, p.196] overflow is obtained for $N>76$ and 64bit arithmetic. This limit seems acceptable for the present purposes.

Remark 3.2.2 The time needed for the “naive” assembly of the triple matrices can be prohibitive. This is due to the fact that the integrals in (3.19b) contain a large number of terms due to the use of the modified bases. Therefore, we assemble each one of the third-order tensors A_{ikm}, B_{jln} separately, requiring $\mathcal{O}(N_y^3)$ and $\mathcal{O}(N_z^3)$ operations, respectively. Note that the constant coefficients of the latter two operation counts are very large. Then we assemble the final triple matrix as:

$$\mathcal{T}_{kilj}^{ab(\alpha\beta\gamma\delta)}(\bar{U})=\sum_{m=1}^{N_y}\sum_{n=1}^{N_z}\hat{U}_{mn}\,A_{ikm}\,B_{jln}\,,\tag{3.20}$$

which takes $\mathcal{O}(N_y^3\cdot N_z^3)$ operations, with a coefficient of order unity. Thereby the large number of terms in the expansion is not felt and we obtain the minimum overall operation count for a Galerkin method. This count should be compared to $\mathcal{O}(N_y^2\cdot N_z^2)$ when employing the collocation method. However, when using the QZ algorithm for the eigensolution—as we presently do—this is not an important drawback, since the latter scales as $\mathcal{O}(N_y^3\cdot N_z^3)$ anyway. Timing of our code will be presented below in § 3.4.

The system (3.18a-3.18b) is again written in the form of a generalized eigenvalue system

$$A\cdot\hat{q}_N=c\,B\cdot\hat{q}_N\quad,\tag{3.21}$$

$N_z \times N_y$	N_{sys}	assembly [sec]	eigensolution [sec]	$\sum$ [sec]
10×20	370	2.16	5.09	7
15×30	855	31.94	55.83	87
20×40	1540	149.20	364.85	514
25×50	2425	541.90	2247.90	2790
30×60	3510	2526.79	7476.95	10004

Table 3.3: Execution time of linear stability analysis (Galerkin-discretized system 3.18a-3.18b) without computation of eigenvectors and not considering temperature perturbations ($Pr = 0$), i.e. the system size is $N_{sys} = (N_y - 1)N_z + N_y(N_z - 1)$. The machine was an Intel-Pentium-IV-based system running at 3GHz and using a compiler from Intel; the eigensolver was `ZGGEV` from LAPACK. Note that the overall scaling is roughly $\mathcal{O}(N_{sys}^3)$.

with $\hat{q}_N$ the coefficient *vector* with the following shape:

$$\hat{q}_N = \left[\hat{v}_{2,1}, \hat{v}_{3,1}, \ldots \hat{v}_{N_y,N_z}, \hat{w}_{1,2}, \ldots \hat{w}_{N_y,N_z}, \hat{\theta}_{1,1}, \ldots \hat{\theta}_{N_y,N_z}\right]^T \quad . \tag{3.22}$$

A, B are again square matrices of size $N_{sys} = (N_y - 1)N_z + N_y(N_z - 1) + N_yN_z$ and all quantities are of complex type.

Since the stability problem is formulated in terms of the coefficients of the expansion, the eigenfunctions—when computed—are obtained in coefficient space. Therefore, a back-transform to physical space needs to be carried out. Similarly, the base profile—when available in physical space—needs to be transformed to coefficient space ($\bar{U}_{mn}$,$\bar{T}_{mn}$) before the assembly of the system (3.18a-3.18b) in order to evaluate the triple integrals. Please refer to appendix B for the details of the transform between physical space and modified Chebyshev space.

3.3 Solution of the eigenvalue problem

3.3.1 QZ algorithm

We wish to compute the "full spectrum" of eigenvalues of our linear system for use in the subsequent analysis. Therefore, we choose a QZ-algorithm-based method. In reality, however, only a part of the obtained eigenvalues are of use since the accuracy decreases with the magnitude of the eigenvalue.

In particular, we use the function `ZGGEV` from the LAPACK library [15]. The results are virtually identical to the ones obtained when using functions from NAG and EISPACK, but in terms of execution speed LAPACK's function was found to be fastest on Intel Pentium-based machines.

3.4 Timing

Table 3.3 shows the execution time of a typical linear stability analysis without computation of eigenvectors and not considering temperature perturbations ($Pr = 0$) as a function of the truncation level when employing the Galerkin method of § 3.2.3. It can be seen that the time needed for assembling the matrices is a non-negligible fraction of the total execution time (between 30%-40%). Contrarily, when using the collocation method, time for assembly is negligible. Here, the overall scaling with the system size is still roughly $\mathcal{O}(N_{sys}^3)$.

3.5 Validation

3.5.1 Plane Poiseuille flow, isothermal

Since it is a standard benchmark problem following the results of Thomas [16], we computed the linear stability of plane Poiseuille flow. For this purpose we solved the z-momentum equation alone for w, setting all y-derivatives to zero. Table 3.4 shows the results for Orszag's [1] least stable mode at various truncation levels for both the collocation and the Galerkin methods. The agreement is complete. We note that the collocation method needs a slightly higher truncation level than the Galerkin method for convergence.

There is one eigenvalue which has not been listed in the paper by Orszag as pointed out in [17]. Both our present methods do obtain this mode. Table 3.5 shows the 36 least stable modes for this case, as obtained by the Galerkin method. They are in complete agreement with Orszag's results, except for the additional mode at position 18.

3.5.2 Plane Poiseuille flow with internal heating

In reference [8] plane Poiseuille flow with internal heating was considered in the limit of vanishing Prandtl number and in [18] for finite Prandtl number, but zero pressure-gradient ($Re = 0$). In the plane case with z the wall-normal coordinate, the mean flow and mean temperature take the following form:

$$\bar{U}(z) = \frac{Gr}{12}(z^4 - 6z^2 + 5) + Re\,(1 - z^2)\,, \tag{3.23a}$$

$$\bar{T}(z) = Gr\,(1 - z^2)\,. \tag{3.23b}$$

For $Re = 0$ the critical values for the Grashof number and the streamwise wavenumber are reported as [8, 18]:

$$\begin{array}{lll} Pr = 0: & Gr_c = 2906.3637\,, & \alpha_c = 1.247\,, \\ Pr = 0.71: & Gr_c = 2848.0201\,, & \alpha_c = 1.2529\,, \\ Pr = 7: & Gr_c = 2799.1968\,, & \alpha_c = 1.2548\,. \end{array} \tag{3.24}$$

Here, we first solved the z-momentum equation alone for w, setting all y-derivatives to zero as in § 3.5.1. Our results using 32 basis functions in conjunction with the Galerkin method are shown in table 3.6. We fixed the wavenumber α and determined the critical value for the Grashof number individually. The agreement with the values in (3.24) is very good.

	Galerkin		collocation	
N_z	$\Re(c)$	$\Im(c)$	$\Re(c)$	$\Im(c)$
8	0.22440098	0.11441970E-1	0.22966184	-0.34496949E-2
16	0.23754535	0.37188124E-2	0.23755963	0.36536676E-2
32	0.23752649	0.37396706E-2	0.23752649	0.37396695E-2
64	0.23752649	0.37396706E-2	0.23752649	0.37396706E-2

Table 3.4: Least stable eigenvalue of plane Poiseuille flow for $\alpha = 1$ and $Re = 10000$ as computed in reference [1]. The reference value is: $\Re(c) = 0.23752649$, $\Im(c) = 0.00373967$. Note that for this mode, w is an even function in the wall-normal direction. The table shows results obtained by means of the present collocation and Galerkin methods for various truncation levels.

number	parity	$\Re(c)$	$\Im(c)$
1	e	0.23752649	0.0037396706
2	o	0.96463092	-0.035167278
3	e	0.96464251	-0.035186584
4	o	0.27720434	-0.050898727
5	o	0.93631654	-0.063201496
6	e	0.93635178	-0.063251569
7	o	0.90798305	-0.091222735
8	e	0.90805633	-0.091312862
9	o	0.87962729	-0.11923285
10	e	0.87975570	-0.11937073
11	e	0.34910682	-0.12450198
12	o	0.41635102	-0.13822653
13	o	0.85124584	-0.14723393
14	e	0.85144938	-0.14742560
15	o	0.82283504	-0.17522868
16	e	0.82313696	-0.17547807
17	e	0.19005925	-0.18282193
18	o	0.21272578	-0.19936069
19	o	0.79438839	-0.20322066
20	e	0.79481839	-0.20352914
21	o	0.53204521	-0.20646522
22	e	0.47490119	-0.20873122
23	o	0.76587681	-0.23118599
24	e	0.76649408	-0.23158507
25	e	0.36849848	-0.23882483
26	o	0.73741577	-0.25871708
27	e	0.73811501	-0.25969189
28	o	0.63671937	-0.25988572
29	o	0.38398761	-0.26510650
30	e	0.58721293	-0.26716171
31	o	0.71231586	-0.28551475
32	e	0.51291620	-0.28662504
33	e	0.70887467	-0.28765535
34	e	0.68286339	-0.30761173
35	o	0.52222816	-0.31429706
36	o	0.69415685	-0.31949825

Table 3.5: The 36 least stable eigenvalues of plane Poiseuille flow for $\alpha = 1$ and $Re = 10000$ computed with the present Galerkin method and a truncation level of $N_z = 64$. These are in full agreement with reference [1], except for our mode 18 which is missing therein. This missing eigenvalue was previously discovered in reference [17]. The parity indicated in the table is that of w.

Pr	α	Gr_c	$\Re(c)$	$\Im(c)$
0.0	1.247	2906.3719	437.35461	-1.4880966e-8
0.71	1.2529	2848.0206	430.68766	+5.6513633e-8
7.0	1.2548	2799.2668	424.62409	-4.6909381e-8

Table 3.6: Complex phase velocity c for internally heated plane Poiseuille flow at zero pressure-gradient ($Re = 0$). The parity of the wall-normal velocity is even. The computation was carried out with the Galerkin method, solving the w-equation alone, suppressing derivatives in the z-direction and using 32 modes (the equivalent of 64 modes in references [8, 18]). While the streamwise wavenumber was kept costant, the Grashof number was varied such as to determine its critical value.

Next, we solve the full two-dimensional problem for the following base profiles:

$$\bar{U}(y,z) = \left(\frac{Gr}{12}\,(y^4 - 6y^2 + 5) + Re\,(1 - y^2)\right)(1 - \frac{z^2}{A^2})\,, \tag{3.25a}$$

$$\bar{T}(y,z) = Gr\,(1 - y^2)\,(1 - \frac{z^2}{A^2})\,, \tag{3.25b}$$

and setting the aspect ratio of the rectangular channel to $A = 100000$. Thereby, the domain approaches that of a plane channel closely and gradients in the z-direction become very small. We used $N_y = N_z = 32$ modes and the Galerkin method of § 3.2.3, obtaining the following values for the critical Grashof number (for fixed values of α):

$$\begin{array}{lll} Pr = 0\,, & \alpha = 1.247: & Gr_c = 2908.02\,, \\ Pr = 0.71\,, & \alpha = 1.2529: & Gr_c = 2849.64\,, \\ Pr = 7\,, & \alpha = 1.2548: & Gr_c = 2800.85\,. \end{array} \tag{3.26}$$

Considering the fact that the gradients in the "spanwise" direction z are not strictly zero, the correspondence with the results from the one-dimensional computations is good.

3.5.3 Rectangular duct, isothermal

Here we perform the validation of our methods for cases with a two-dimensional base flow at zero Grashof and zero Prandtl number.

3.5.3.1 Parabolic base flow

We consider the artificial base profile

$$\bar{U}(y,z) = (1 - y^2)\left(1 - \left(\frac{z}{A}\right)^2\right)\,, \tag{3.27}$$

which is very similar to the "real" laminar profile obtained when solving the Poisson equation (A.1). However, using an analytic expression is more convenient for the purpose of validation since it eliminates a potential source of error and allows for more consistent future comparison.

We choose $A = 1$ (square duct) and $Re = 10000$, $\alpha = 1$. Figure 5.1 shows the eigenvalue spectrum at two truncation levels N_y=N_z=20 and N_y=N_z=45. It can be seen that a considerable number of modes with large phase velocity $|c| \sim \mathcal{O}(10)$ are obtained with the collocation method; these modes appear in all four quadrants of the complex plane and the corresponding eigenfunctions are non-physical. The Galerkin method, on the other hand, only generates stable modes in quadrant IV. A zoom in the "zone of interest", i.e. the region around $\Im(c) = 0$ and for $\Re(c) > 0$

$N_y = N_z$	$\Re(c)$	$\Im(c)$
10	0.52941648	$+0.30545132E-1$
12	0.63809100	$+0.63138137E-2$
14	0.71240084	$-0.14254168E-1$
16	0.94966465	$-0.21451699E-1$
18	0.95173487	$-0.22327513E-1$
20	0.95148598	$-0.22634588E-1$
22	0.95147155	$-0.22581841E-1$
24	0.95147636	$-0.22584224E-1$
26	0.95147598	$-0.22584340E-1$
28	0.95147600	$-0.22584318E-1$
30	0.95147600	$-0.22584322E-1$

Table 3.7: Convergence series for the least stable eigenvalue of symmetry mode I at $A = 1$, $\alpha = 1$, $Re = 10000$ for the analytic mean profile $\bar{U} = (1 - y^2)(1 - z^2)$; the Galerkin method and 64 bit arithmetic were used.

(cf. figure 5.2) shows that the eigenvalues obtained by the two methods do converge to the same values there.

A look at some selected eigenfunctions (figure 5.3) shows that indeed the results obtained by the collocation and Galerkin methods match for these modes. However, close inspection reveals that at a truncation level of N_y=N_z=20 the eigenfunctions obtained by collocation are slightly oscillatory whereas those obtained by the Galerkin method are smooth.

The present result can be summed up as follows: the Galerkin method yields reasonable eigenvalues and eigenfunctions; the collocation method leads to what could be called "spurious eigenvalues" and has a lower resolving efficiency. Therefore, we will use the Galerkin method from hereon.

Finally, we present a convergence series of the most unstable eigenvalue at the present parameter values, obtained with the Galerkin method (table 3.7). Convergence to within 6 significant digits can be observed for a truncation level of $N_y = N_z = 30$.

3.5.3.2 Real base flow: Tatsumi's case

Here we revisit the analysis of reference [6] for the purpose of quantitative validation of the present Galerkin method. We focus upon the aspect ratio $A = 5$ and the "critical parameters" $Re = 10400$, $\alpha = 0.91$. Table 3.8 shows the convergence of the least stable eigenvalue with parity I (this mode is the most unstable of the four parities). Please note that—for the purpose of comparison—the phase velocity has been divided by Re to match the non-dimensional form used in reference [6] (cf. § 2.4). Reference [6] uses 20×30 modified Legendre polynomials in this case, making use of the symmetry properties; this mode is found to be "neutral". Our present finding is that at a truncation level of 20×30 the real part of the phase velocity is determined up to three significant digits.

Theofilis [19] has published a convergence sequence for this mode, however without a detailed description of his numerical discretization. Therein, Arnoldi's method is used for the solution of the eigensystem and the least stable mode at a truncation level (in our notation) of $N_y = 20$, $N_z = 30$ yields the eigenvalue $c = 0.21167 + I \cdot 0.00001$. Given the fact that the eigensolution procedure is of quite different nature, the correspondence is reasonable.

Figures 5.5-5.6 show the eigenvalue spectrum of our present results for various truncation levels. It can be seen that a considerable number of non-converged eigenvalues are obtained at all typical truncation levels. These modes have a negative growth rate but it is of similar magnitude as the

$N_z \times N_y$	$\Re(c)$	$\Im(c)$
10×20	0.559622	0.22787675E-1
15×30	0.232026	0.10520835E-3
20×30	0.232165	0.13115827E-3
20×35	0.232342	-0.12105729E-4
25×40	0.232386	-0.24038751E-4
30×45	0.232392	-0.22714486E-4
35×50	0.232392	-0.22017663E-4
40×60	0.232392	-0.21974008E-4

Table 3.8: Convergence of the least stable mode (symmetry I) for iso-thermal flow in a rectangular duct of aspect ratio $A = 5$ at $Re = 10400$ and $\alpha = 0.91$.

"critical" mode. This shows that for the present type of flow configuration special care needs to be taken as to assure that a numerical results reflects a converged eigenvalue, i.e. refinement studies need to be carried out systematically.

Finally, the eigenfunction corresponding to the "critical" mode is shown in figure 5.7. A staggering of flat, streamwise elongated high- and low-speed regions can be observed near the corner for all velocity components. Thereby, very thin elliptically-shaped zones of high shear are found in a cross-sectional plane. As pointed out in reference [6], these shear-layers coincide approximately with the location of the critical layers of the base profile. This latter feature is visible in figure 5.8 which shows isocontours of the eigenfunctions in a cross-section at arbitrary phase.

3.5.4 Rectangular duct, non-isothermal

Table 3.9 shows the complex phase velocity obtained for the most unstable mode with symmetry I in the square duct ($A = 1$) at finite values for the Prandtl, Grashof and Reynolds numbers ($Pr = 7$, $Gr = 3000$, $Re = -400$) and increasing truncation levels. This corresponds to an unstable mode (cf. figure 5.10 below) with a very smooth spatial structure. Convergence to within 7 digits seems to be reached at $N_y = N_z = 22$. For higher truncation levels the eigenvalue slowly deviates from its value at $N_y = N_z = 22$. Compared to the purely hydrodynamic case (cf. table 3.7), the increased system size by approximately a factor of 1.5 (through the consideration of the temperature equation) probably leads to the appearance of round-off effects at lower truncation levels.

$N_y = N_z$	$\Re(c)$	$\Im(c)$
10	$-0.42009479E2$	$0.45720136E1$
12	$-0.42009484E2$	$0.45720172E1$
14	$-0.42009484E2$	$0.45720174E1$
16	$-0.42009484E2$	$0.45720174E1$
18	$-0.42009483E2$	$0.45720175E1$
20	$-0.42009483E2$	$0.45720160E1$
22	$-0.42009486E2$	$0.45720160E1$
24	$-0.42009481E2$	$0.45720239E1$
26	$-0.42009478E2$	$0.45720153E1$
28	$-0.42009479E2$	$0.45720114E1$
30	$-0.42009499E2$	$0.45719596E1$

Table 3.9: Convergence series for the least stable eigenvalue of symmetry mode I at $A = 1$, $\alpha = 1$, $Pr = 7$, $Gr = 3000$, $Re = -400$, using the Galerkin method and 64 bit arithmetic.

Chapter 4

Results

4.1 The square duct at finite (high) Prandtl number

Figure 5.9 shows neutral surfaces in (Gr,Re,α)-space for the square duct ($A = 1$) at a relatively high value for the Prandtl number ($Pr = 7$). A truncation level of $N_y = N_z = 20$ and a relatively coarse grid of 15, 15, 11 discrete values, respectively, in parameter space was used. The range of parameters is the following:

$$0 \leq Gr \leq 5000 \tag{4.1}$$

$$-10^4 \leq Re \leq 0 \tag{4.2}$$

$$0.5 \leq \alpha \leq 1.5 \tag{4.3}$$

Figure 5.9 demonstrates several facts:

- The flow loses stability in a limited region at relatively low Reynolds numbers. The exact location of this region will be further discussed below.
- The dependence upon the value of the streamwise wavenumber is small in the region which we have investigated. We will therefore mostly concentrate upon a fixed value of $\alpha = 1.0$ in our further discussion.
- Although instability was detected for all three symmetry modes, the unstable region is largest for mode I; depending on the location in parameter space, either mode II or III have the smallest growth rate. Correspondingly, mode I has the largest growth rate at a given unstable point in parameter space. Consequently, we can concentrate mainly upon mode I in the following discussion.

Figure 5.10 shows the stability properties of the square duct at $Pr = 7$, $\alpha = 1$ w.r.t. symmetry mode I in the (Gr,Re)-plane, i.e. data in a single plane of the parameter space shown in figure 5.9. Here, a truncation level of $N_y = N_z = 25$ was used and the density of the discrete parameter points was increased near the unstable region. It can be observed that the only unstable points are approximately located in the wedge-shaped region corresponding to the inflectional properties of the mean-flow discussed in § 2.2. More precisely, we refer to the region where the mean flow exhibits additional inflection lines according to definition (2.12). Interestingly, in the neighboring region where we have reverse mean flow *and* additional inflection lines, only few unstable points were found. It should also be noted that the unstable region approaches the origin in (Gr,Re)-space closely (at the present value for the Prandtl number) but does not include it, nor does it include the abscissa $Gr = 0$ or the ordinate $Re = 0$.

4.1.1 Structure of the unstable eigenfunctions

Figure 5.11 shows the mean flow for $A = 1$, $Gr = 5050$ and $Re = -714.3$. The mean flow has 16 disjoint inflection lines but no reverse flow ($-95.062 \leq \bar{U} \leq 0$). The corresponding unstable eigenfunction for $Pr = 7$ and symmetry mode I has the complex phase velocity $c = -91.205 + 6.543\,I$. It is interesting to note that the perturbation propagates at a velocity which is close to the maximum mean flow velocity. Some unstable modes were found to exceed the maximum of $\bar{U}$ by several percent, a phenomenon which has been observed e.g. by Joseph [20]. He also derives rigorous bounds for the phase velocity in circular pipe flow. In the future, his analysis could be performed for the present rectangular configuration.

Figure 5.12 shows a vector plot of flow in a cross-sectional plane involving the streamwise direction and the y axis. Two zones of recirculating flow—spanning the full channel height—can be observed. Figure 5.13 shows contour-lines of the perturbations of the three velocity components and temperature in a cross-sectional plane at arbitrary phase; figure 5.14 depicts the same quantities in three dimensions over one full period in the streamwise direction. It can be seen that the structure resembles a pair of vortices or pockets of vorticity with the main vorticity contribution lying in the cross-sectional plane. Also, temperature perturbations are very similar in shape to those of the streamwise velocity.

The following figures 5.15-5.18 show the corresponding plots of the eigenfunctions for symmetry modes I and II at the same point in parameter space. They are similar in shape, except for the obvious changes due to symmetry constraints.

4.2 Dependence upon Prandtl number

The first question we would like to address here is: are there unstable modes for the square duct in the limit of vanishing Prandtl number? We have swept the parameter space for $A = 1$, $Pr = 0$ in the following range:

$$-5 \cdot 10^4 \leq Re \leq 0 \tag{4.4}$$

$$0 \leq Gr \leq 8000 \tag{4.5}$$

$$0.5 \leq \alpha \leq 2.0 \tag{4.6}$$

for all three different parities and using a truncation level of up to $N_y = N_z = 35$. No unstable modes could be detected.

Figures 5.19 and 5.20 show stability diagrams in the (Gr,Re)-plane (like figure 5.10) for $Pr = 3$ and $Pr = 0.71$, respectively. It is evident that a decrease of the Prandtl number reduces the region where unstable modes are obtained. At the same time, all unstable modes remain within the approximate bounds which were discussed above for the case of $Pr = 7$.

Figure 5.22 shows the neutral curve for fixed Grashof number $Gr = 9000$ and varying both the Reynolds number (in the appropriate range, cf. figure 5.21) and the Prandtl number. The value for the Prandtl number where instability is first observed is $Pr = 0.3$. It should be noted, however, that at such high values of the Grashof number the assumption of small density variations underlying the Boussinesq hypothesis become questionable. Therefore, it was not attempted to search further for any global critical value of the Prandtl number.

4.3 Dependence upon aspect ratio

The stability of flow in a rectangular duct was investigated setting $A = 4$. At this aspect ratio, the truncation level of our expansion was set to $N_y = 20$, $N_z = 30$. The Prandtl number was fixed at $Pr = 7$. Figure 5.23 shows again the stability diagram in the (Gr,Re)-plane for symmetry mode I. The range where unstable modes are obtained is larger than for the corresponding case in the square duct (cf. figure 5.10). Again we have a correspondence between the location of the unstable points and the inflectional properties of the mean flow. However, in the present case, these unstable points are concentrated around the boundary between the zones of additional inflection lines and reverse flow.

Figure 5.24 shows the mean flow and figures 5.25-5.30 the shape of three different unstable eigenfunctions with successively increasing Grashof and Reynolds number. At the lowest value of

Gr and Re, the shape of the perturbations is similar to the square duct case, i.e. we observe a pair of slightly elongated pockets of vortical motion, trailing each other along the streamwise direction. In the two following cases, these structures become more elongated and their arrangement is staggered in the cross-flow direction z. At the highest values for Grashof and Reynolds number, the structures are slightly bent towards the center of the channel. Furthermore, the absolute value of the phase velocity of the perturbations decreases relative to the maximum absolute value of the mean flow when increasing Gr and Re simultaneously.

Chapter 5

Conclusions

We have investigated the linear stability—under the assumption of the Boussinesq hypothesis—of flow in a rectangular, vertically oriented duct which is subject to a constant streamwise pressure gradient and homogeneous internal heating.

In the first part of the present study, the mean-flow characteristics were presented and a classification of different regimes in terms of inflectional properties was proposed. For this purpose the appearance of additional inflection lines and of reverse flow was mapped in the two-dimensional parameter space spanned by the Grashof and Reynolds numbers. For fixed aspect ratio of the channel geometry, these two characteristics occur in wedge-shaped regions starting at the origin and being located in the second and fourth quadrant of the Gr-Re diagram (i.e. when buoyancy and pressure forces are opposed).

Secondly, the linear stability problem was formulated in terms of normal modes and its symmetry properties were found to be the same as those of the corresponding purely hydrodynamic case. The numerical discretization of the minimal system (streamwise velocity and pressure eliminated, symmetries imposed) was realized by means of a collocation method and a Galerkin method. In both cases, modified Chebyshev expansion functions which satisfy the boundary conditions of the respective variables were employed. It was found that both methods consistently deliver the relevant eigenvalues, but that the collocation method yields additional spurious modes; the latter was therefore not further considered. Extensive validation steps were carried out. Our method is consistent with previous results for plane Poiseuille flow, pressure-driven rectangular duct flow and internally-heated plane Poiseuille flow.

Our computations have shown the following facts:

- The flow in the square duct loses stability in a region closely related to the inflectional properties of the mean flow.
- All three symmetry modes are unstable, mode I is most unstable.
- For vanishing Prandtl number, no unstable modes could be found.
- The critical value for the Prandtl number decreases with increasing Grashof number. A global minimum was not determined due to the limitations of the Boussinesq hypothesis.
- The neutral region increases when the aspect ratio is increased.
- The unstable eigenfunctions have the shape of slightly elongated pockets of vortical motion, trailing each other along the streamwise direction. Temperature perturbations closely resemble those of streamwise velocity.

Outlook. In the future we will proceed the study of the transition in the present configuration along two separate lines. On one hand, the "sequence-of-bifurcations" approach will be pursued. For this purpose linearly unstable perturbations obtained herein will be used as initial values for a non-linear iterative procedure. Non-linear solutions can be tracked in parameter space. The linear stability of the non-linear solutions will then be investigated, which in turn feeds into a further non-linear iterative procedure and so on.

On the other hand, a fully spectral direct numerical simulation (DNS) code has been developed in a related study. With the aid of that tool, the temporal evolution of any of the above mentioned perturbations can be investigated in detail.

Bibliography

[1] S.A. Orszag. Accurate solution of the Orr-Sommerfeld equation. *J. Fluid Mech.*, 50:689–703, 1971.

[2] U. Ehrenstein and W. Koch. Three-dimensional wavelike equilibrium states in plane Poiseuille flow. *J. Fluid Mech.*, 228:111–148, 1991.

[3] M. Nagata. Three-dimensional finite-amplitude solutions in plane Couette flow: bifurcation from infinity. *J. Fluid Mech.*, 217:519–527, 1990.

[4] D.R. Barnes and R.R. Kerswell. New results in rotating Hagen-Poiseuille flow. *J. Fluid Mech.*, 417:103–126, 2000.

[5] L. Rosenhead, editor. *Laminar boundary layers*, chapter III. Oxford U. Press, 1963.

[6] T. Tatsumi and T. Yoshimura. Stability of the laminar flow in a rectangular duct. *J. Fluid Mech.*, 212:437–449, 1990.

[7] V. Theofilis, P.W. Duck, and J. Owen. Viscous linear stability analysis of rectangular duct and cavity flows. *J. Fluid Mech.*, 505:249–286, 2004.

[8] M. Nagata and S. Generalis. Transition in convective flows heated internally. *J. Heat Transfer*, 124(4):635–642, 2002.

[9] J. Shen. Efficient spectral-Galerkin method II. Direct solvers of second and fourth order equations by using Chebyshev polynomials. *SIAM J. Sci. Comput.*, 16(1):74–87, 1995.

[10] G. Kawahara, J. Jiménez, M. Uhlmann, and A. Pinelli. The instability of streaks in near-wall turbulence. *CTR Res. Briefs*, pages 155–170, 1998.

[11] N.Y. Lee, W.W. Schulz, and J.P. Boyd. Stability of fluid in a rectangular enclosure by spectral method. *Int. J. Heat Mass Transfer*, 32(3):513–520, 1989.

[12] J.P. Boyd. *Chebyshev and Fourier spectral methods*. Dover, 2000.

[13] G.B. McFadden, B.T. Murray, and R.F. Boisvert. Elimination of spurious eigenvalues in the Chebyshev tau spectral method. *J. Comput. Phys.*, 91:228–239, 1990.

[14] C. Canuto, M.Y. Hussaini, A. Quarteroni, and T.A. Zang. *Spectral methods in fluid dynamics*. Springer, 1988.

[15] E. Anderson, Z. Bai, C. Bischof, S. Blackford, J. Demmel, J. Dongarra, J. Du Croz, A. Greenbaum, S. Hammarling, A. McKenney, and D. Sorensen. *LAPACK Users' Guide*. SIAM, Philadelphia, PA, 1999.

[16] L.H. Thomas. The stability of plane Poiseuille flow. *Phys. Review*, 91(4):780–791, 1953.

[17] J.J. Dongarra, B. Straughan, and D.W. Walker. Chebyshev tau - QZ algorithm methods for calculating spectra of hydrodynamic stability problems. *J. Appl. Num. Math.*, 22(4):399–435, 1996.

[18] S. Generalis and M. Nagata. Transition in homogeneously heated inclined plane parallel shear flows. *J. Heat Transfer*, 125:795–803, 2003.

[19] V. Theofilis. Linear instability analysis in two spatial dimensions. In K.D. Papailiou, D. Tsahalis, J. Périaux, C. Hirsch, and M. Pandolfi, editors, *4th ECCOMAS CFD Conf.*, volume 2, pages 547–552. Wiley, 1998.

[20] D.D. Joseph. Eigenvalue bounds for the Orr-Sommerfeld equation. Part 2. *J. Fluid Mech.*, 36(4):721–734, 1969.

[21] S. Chandrasekhar. *Hydrodynamic and hydromagnetic stability.* Dover, New York, 1961.

[22] R.M. Clever and F.H. Busse. Transition to time-dependent convection. *J. Fluid Mech.*, 65(4):625–645, 1974.

Figures

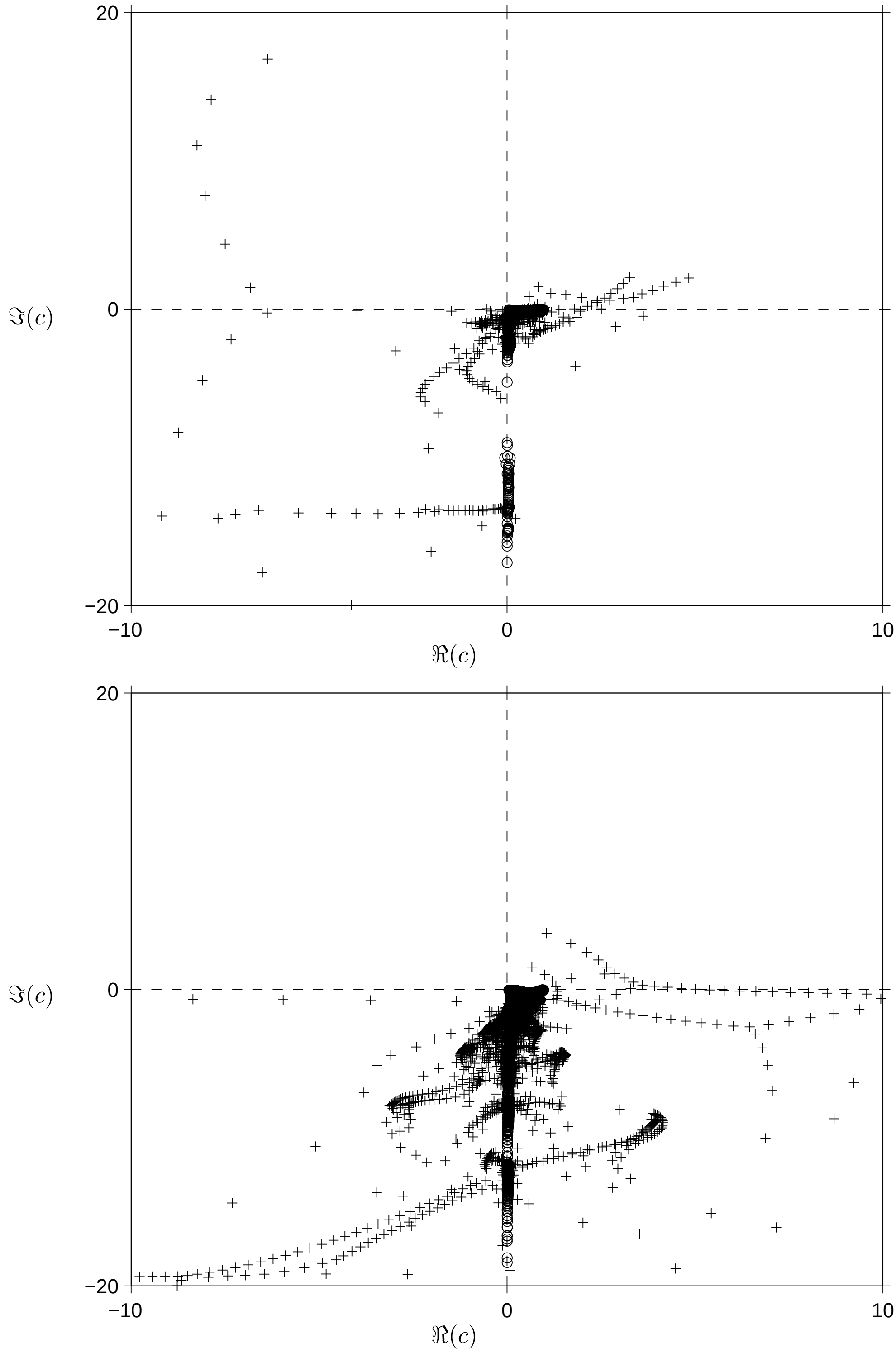

Figure 5.1: Eigenvalue spectrum for isothermal flow in a square duct with a parabolic base profile, Re = 10000, α = 1 and solution parity I. The markers + refer to results from the collocation method, the $\circ$ to Galerkin. The truncation level was N_y=N_z=20 (top), N_y=N_z=45 (bottom).

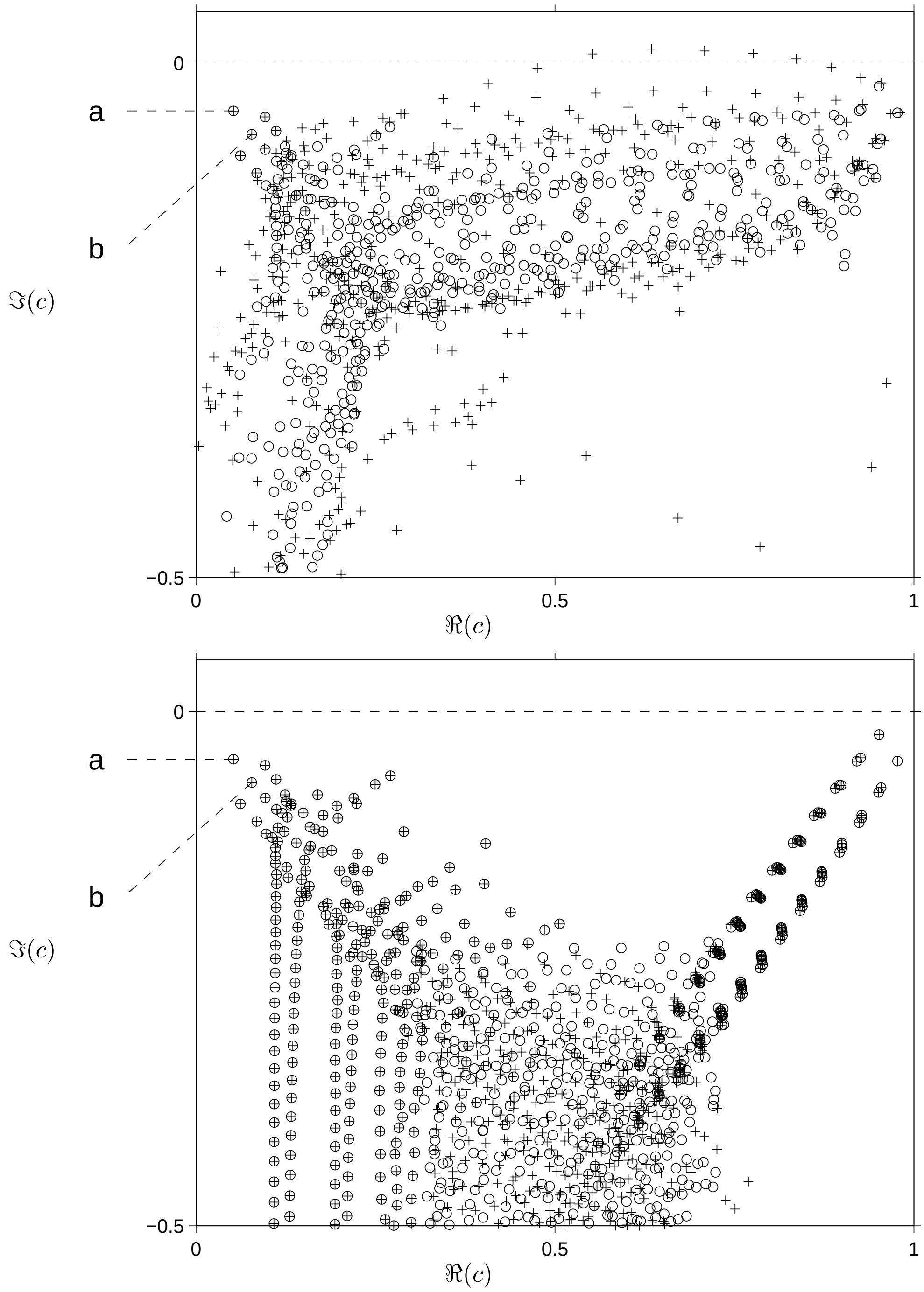

Figure 5.2: As figure 5.1, but showing a zoom of both axes near the origin. Two eigenvalues are labelled ("a", "b") for reference in the text and below.

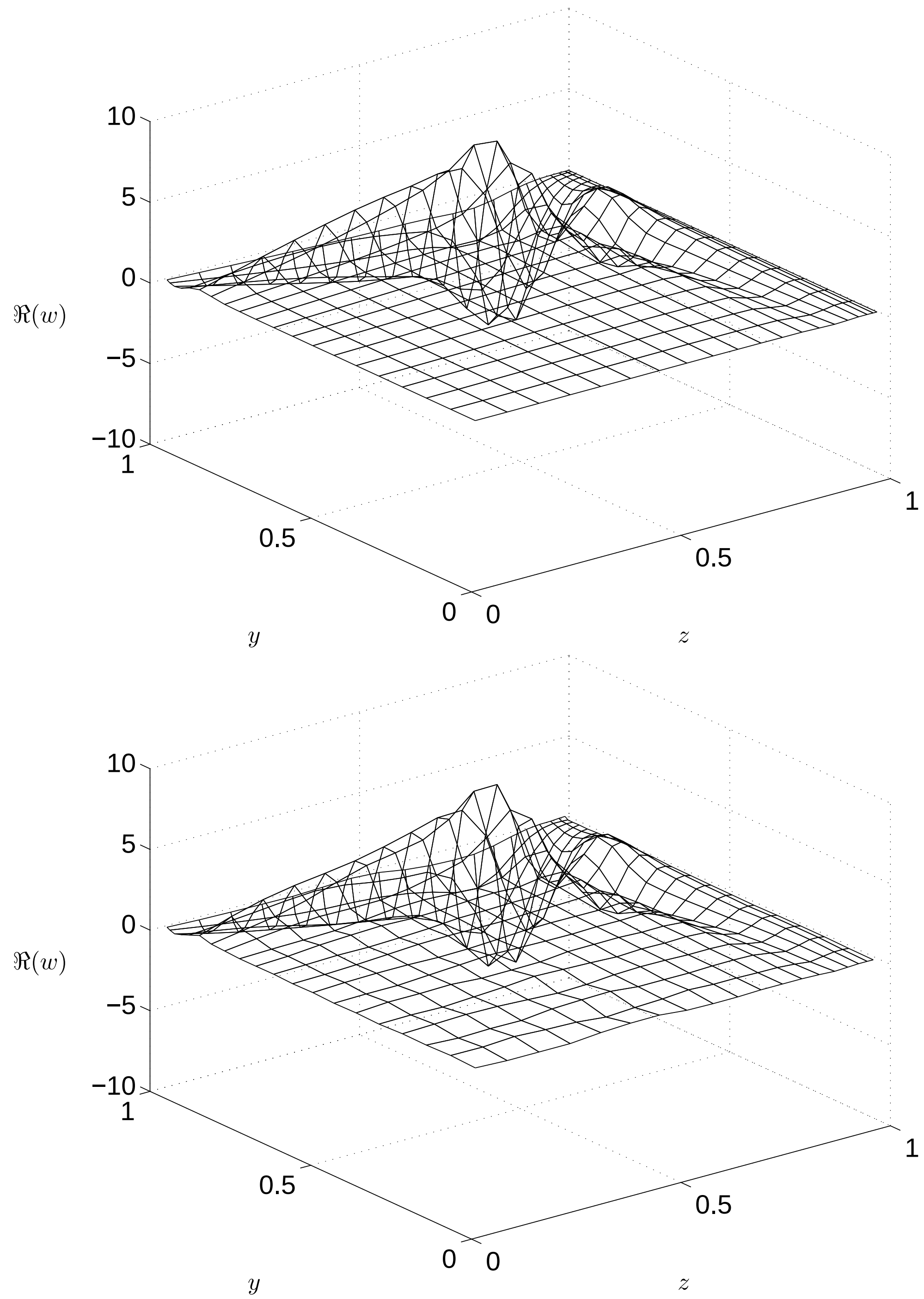

Figure 5.3: Real part of the velocity component w of the eigenfunction marked "a" in figure 5.1. The top figure shows the result from the Galerkin method, the bottom the result obtained by collocation. The eigenfunction has been normalized such that $\Re(w(y_4, z_5)) = 1$ and $\Im(w(y_4, z_5)) = 0$, where y_i, z_j are Gauss-Lobatto points (3.9). The truncation level is N_y=N_z=20.

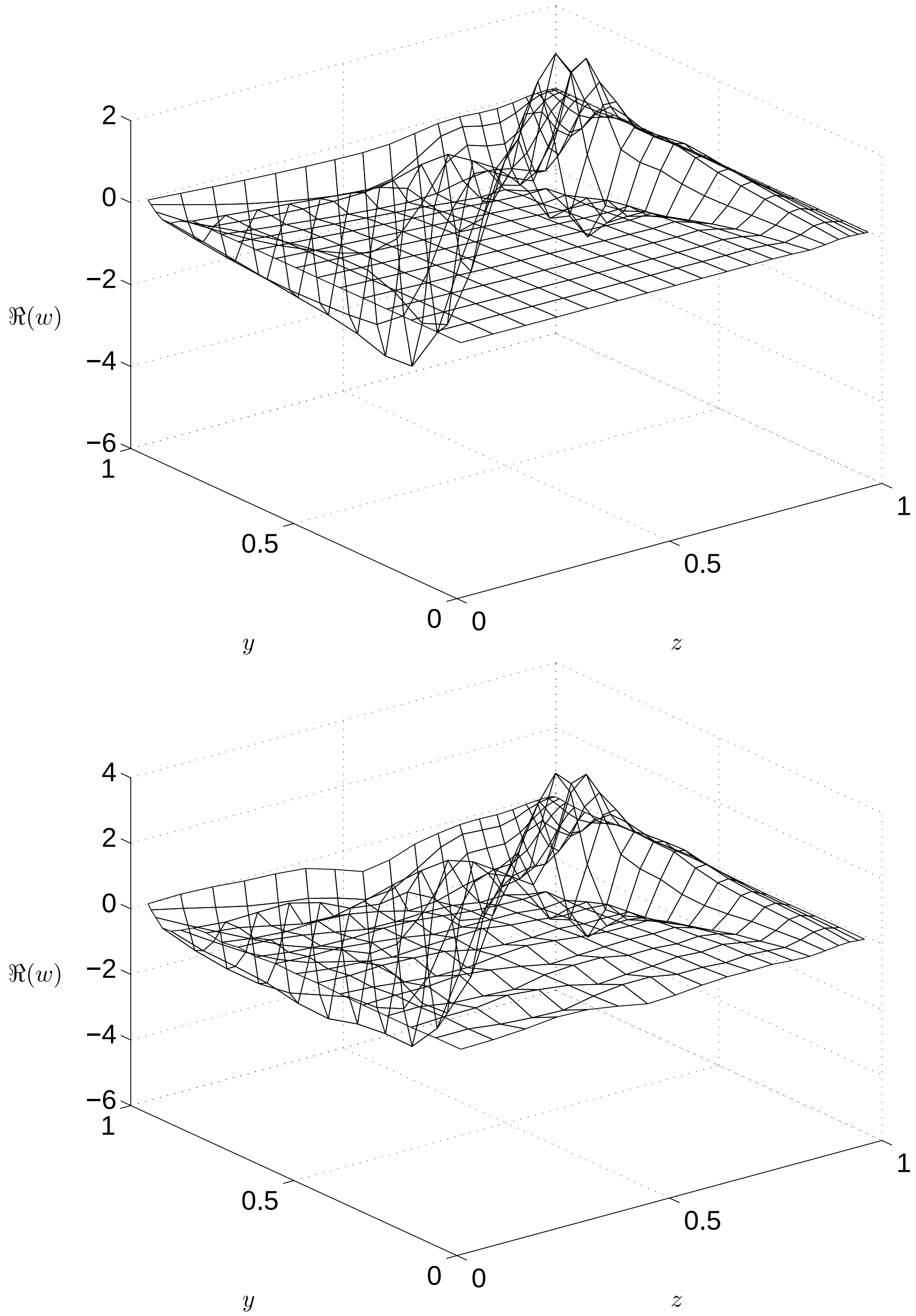

Figure 5.4: Real part of the velocity component w of the eigenfunction marked “b” in figure 5.1. The top figure shows the result from the Galerkin method, the bottom the result obtained by collocation. The eigenfunction has been normalized such that $\Re(w(y_4, z_5)) = 1$ and $\Im(w(y_4, z_5)) = 0$, where y_i, z_j are Gauss-Lobatto points (3.9). The truncation level is N_y=N_z=20.

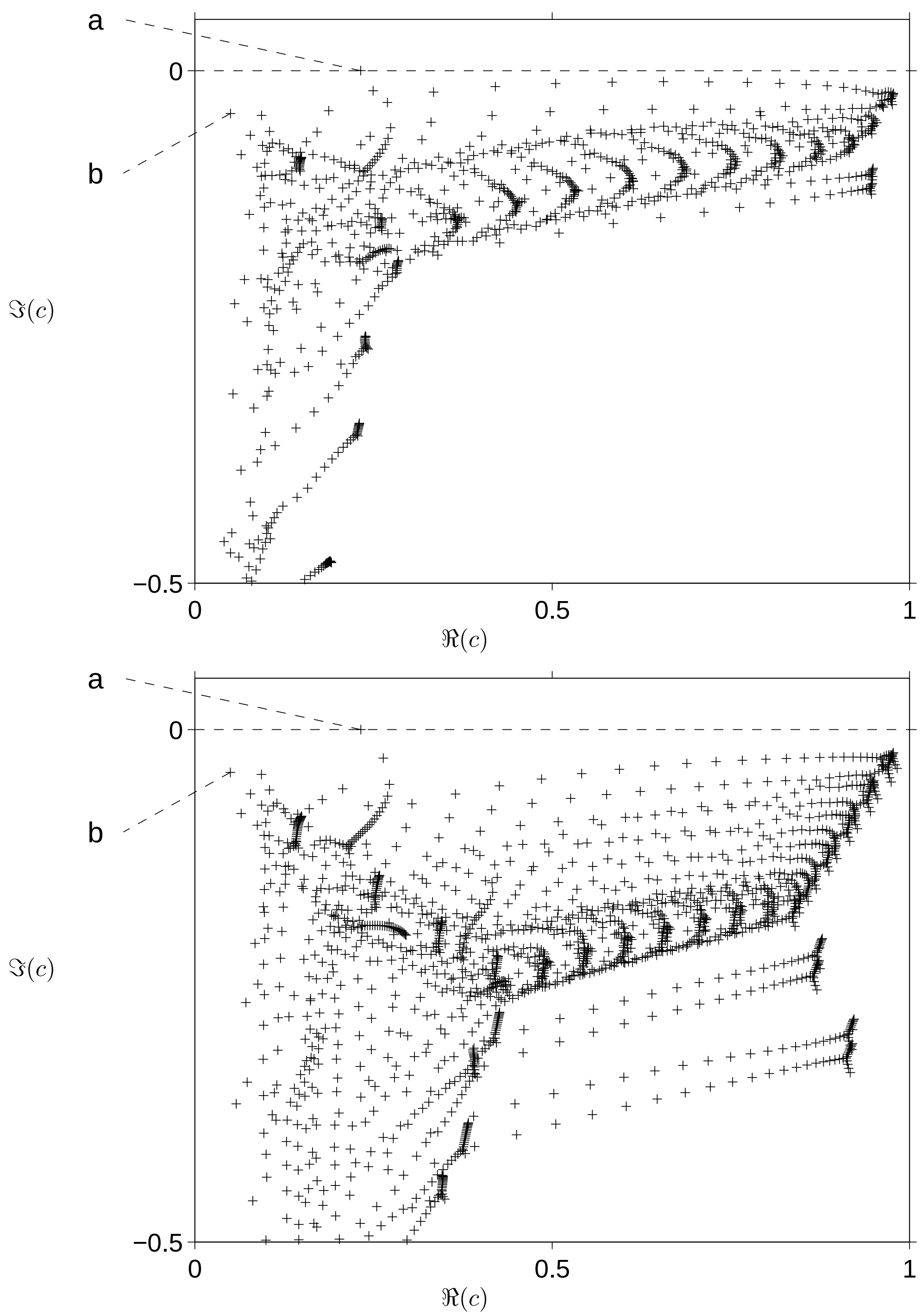

Figure 5.5: Eigenvalue spectrum for isothermal flow in a rectangular duct with aspect ratio $A = 5$, $Re = 10400$, $\alpha = 0.91$ and solution parity I. The results are obtained with the Galerkin method. The truncation level was N_y=20, N_z=30 (top), N_y=30, N_z=45 (bottom). Eigenvalues marked "a" and "b" are further referenced in the text and below.

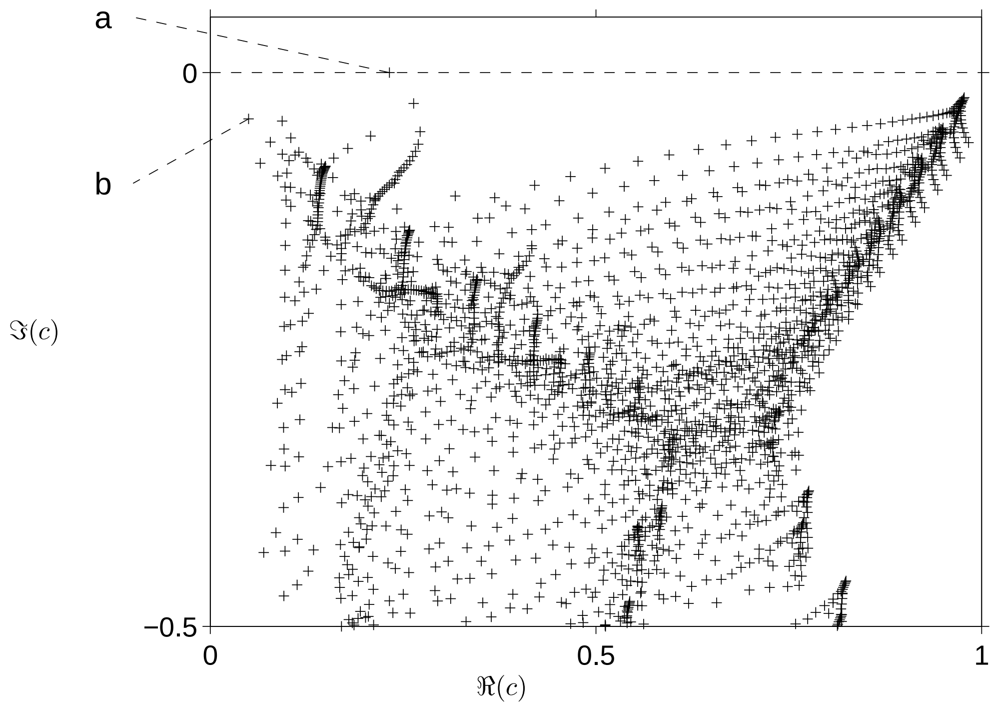

Figure 5.6: As figure 5.5, but the truncation level is N_y=40, N_z=60.

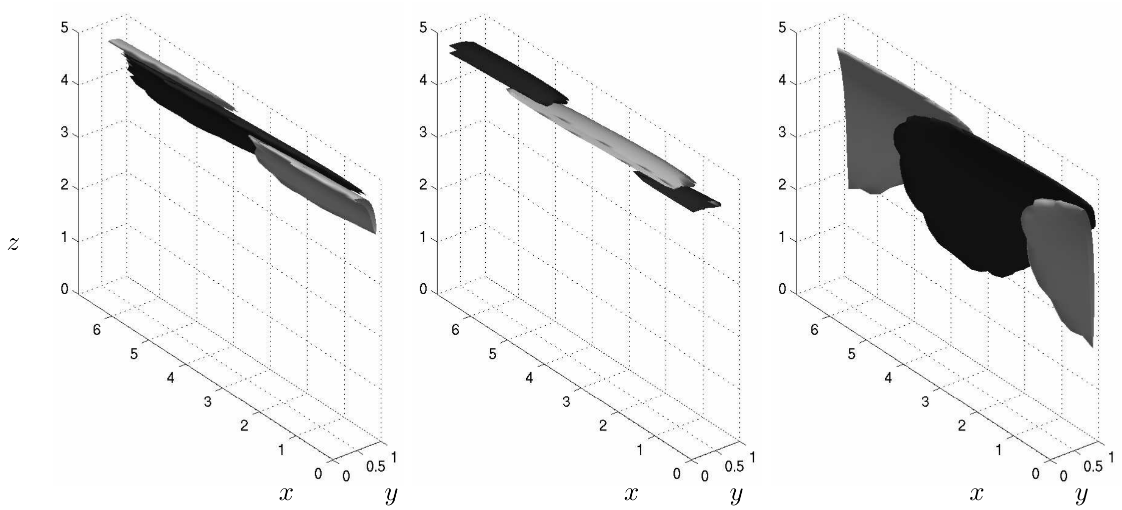

Figure 5.7: Eigenfunction corresponding to the eigenvalue marked "a" in figures 5.5-5.6, computed at a truncation level of N_y=25, N_z=35. Isosurfaces at 40% of the maximum value over one streamwise period of u (left), v (center), w (right). The phase is arbitrary. Only one quadrant of the cross-section is shown. Light shading corresponds to negative perturbations, dark shading to positive values.

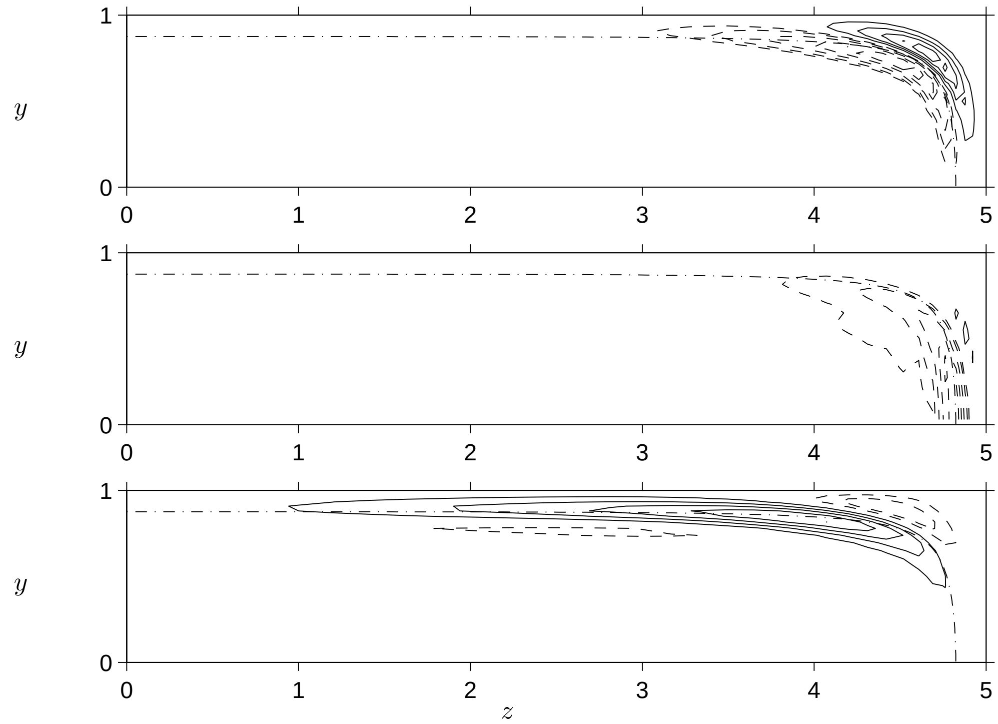

Figure 5.8: As figure 5.7, but showing only a cross-section of the eigenfunction (arbitrary phase) with u (top), v (center), w (bottom). The dashed contour lines correspond to negative perturbations, the solid lines to positive perturbations. The chain-dotted line is the critical line, i.e. the isocontour with $\bar{U} = 0.2324$.

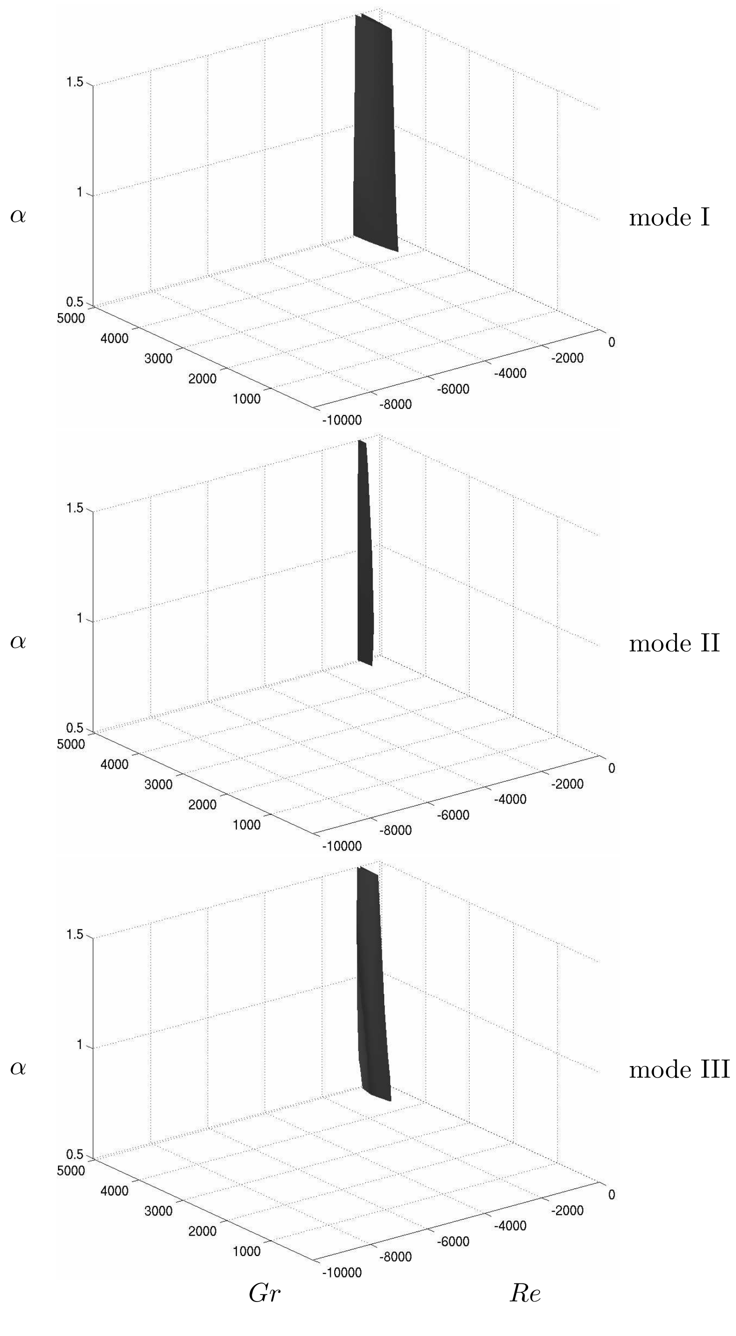

Figure 5.9: Neutral surface in Gr-Re-α-space for aspect ratio $A = 1$ and $Pr = 7$. These results were obtained at a truncation level of $N_y = N_z = 20$. The parameter space was scanned at 15, 15, 11 discrete values of Gr, Re, α, respectively.

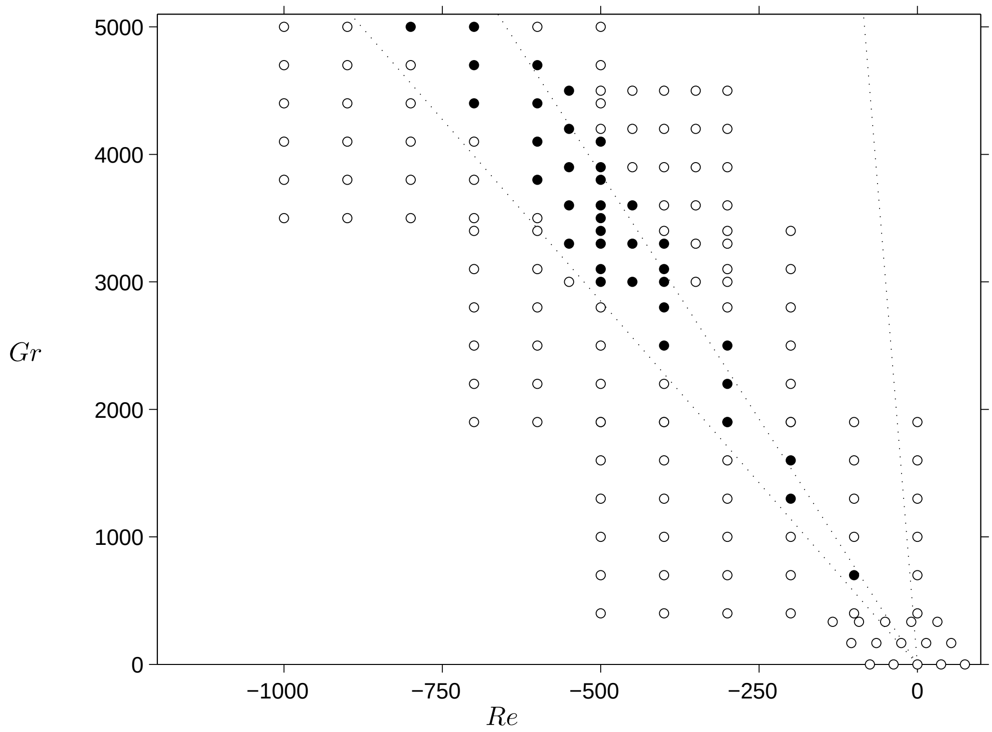

Figure 5.10: Stability diagram in the Gr-Re-plane for aspect ratio $A = 1$ and streamwise wavenumber $\alpha = 1$ at $Pr = 7$ and considering the symmetry mode I; the truncation level being $N_y = N_z = 25$. Solid circles refer to positive or zero growth rate, open symbols to negative growth. The straight dotted lines correspond to the bounds of the appearance of additional inflection lines and reverse flow, respectively (cf. figure 2.9).

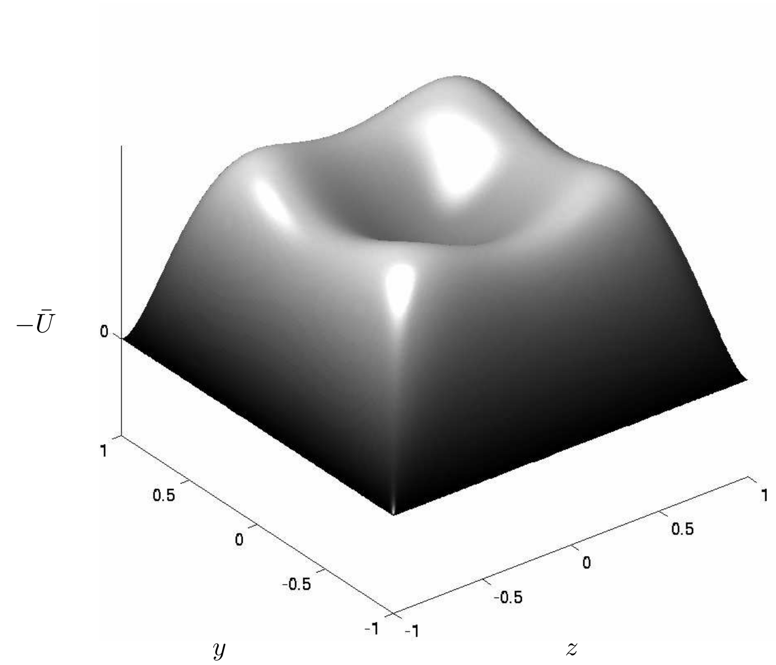

Figure 5.11: Mean flow for $A = 1$, $Gr = 5050$ and $Re = -714.3$. $-95.062 \leq \bar{U} \leq 0$. The flow has 16 disjoint inflection lines.

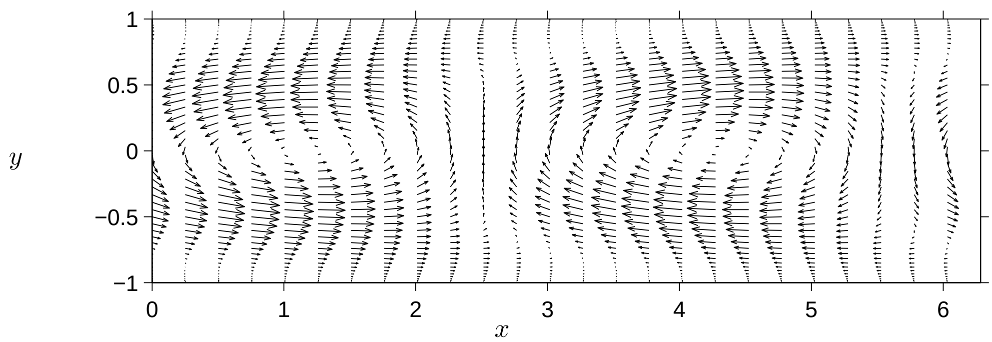

Figure 5.12: Vector plot of the flow in the (x,y)-plane corresponding to one streamwise period of the most unstable eigenfunction at the following parameter point: $A = 1$, $Pr = 7$, $Gr = 5050$, $Re = -714.3$, $\alpha = 1$, mode I. The complex phase velocity for this disturbance is: $c = -91.205 + 6.543\,I$.

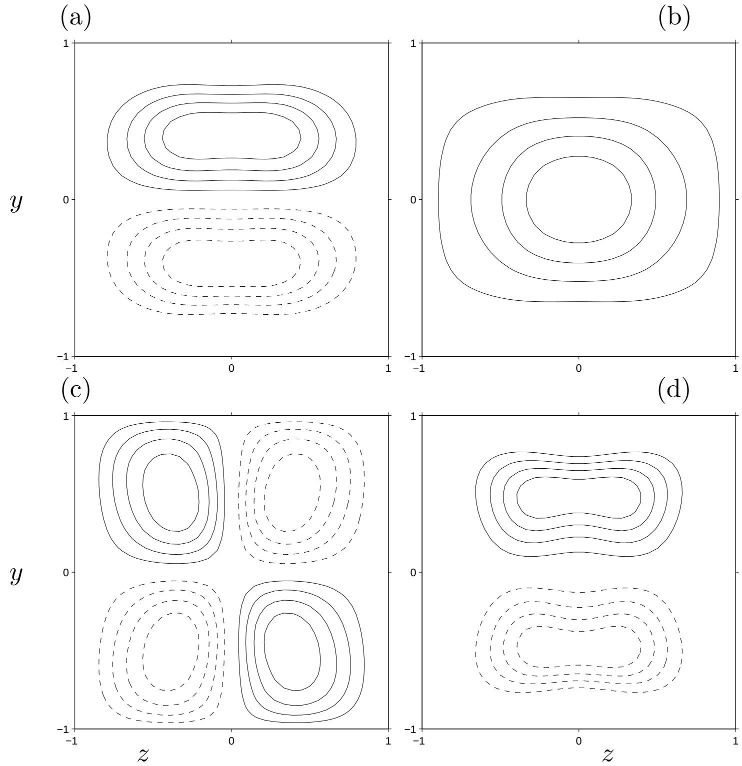

Figure 5.13: Uniformly-spaced isocontours (negative values dashed) of the normalized eigenfunction at arbitrary phase corresponding to the following parameter point: $A = 1$, $Pr = 7$, $Gr = 5050$, $Re = -714.3$, $\alpha = 1$, mode I. The complex phase velocity for this disturbance is: $c = -91.205 + 6.543\,I$. The different graphs show (a) u, (b) v, (c) w, (d) θ.

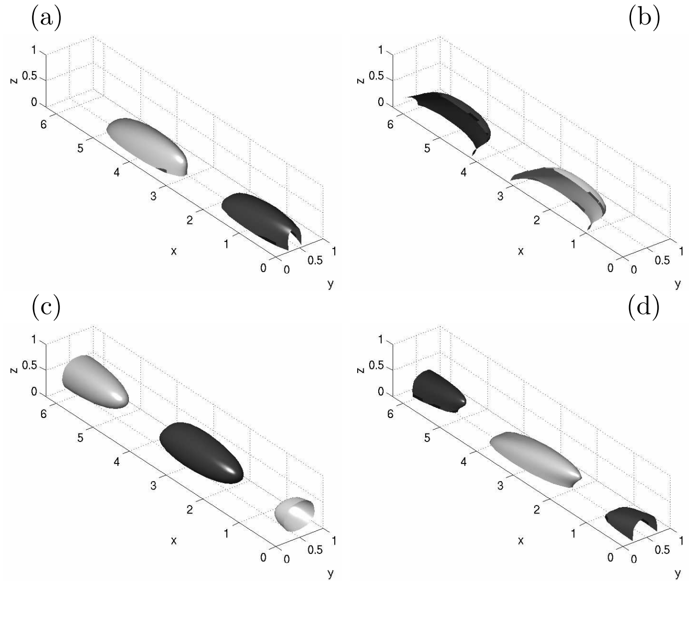

Figure 5.14: As figure 5.13, but showing iso-surfaces of (a) u, (b) v, (c) w, (d) ϕ at ± 0.5 of the respective maximum values. Note that the second quadrant of the (y,z)-cross-section is shown.

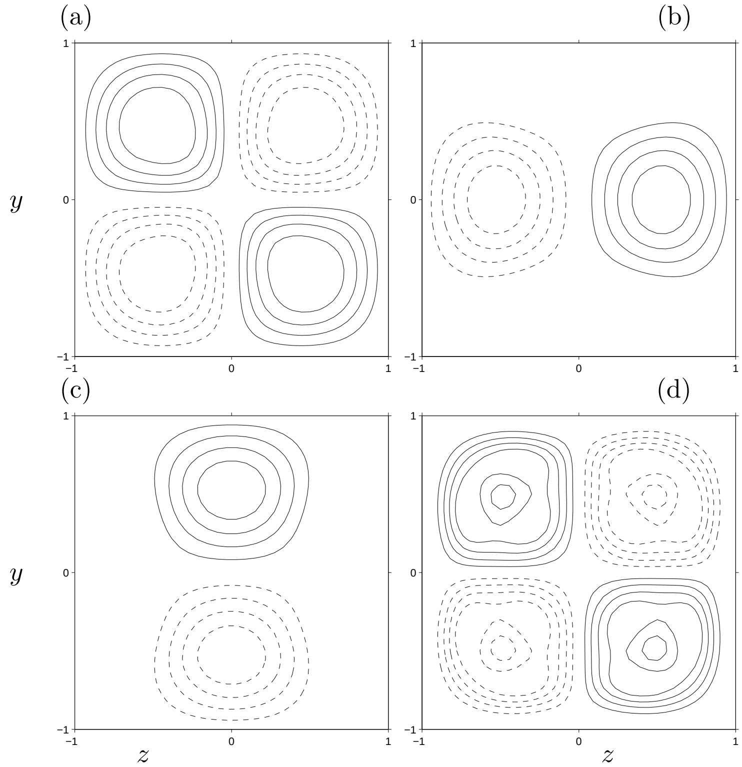

Figure 5.15: As figure 5.13, but showing mode II. The complex phase velocity for this disturbance is: $c = -95.834 + 2.214\,I$.

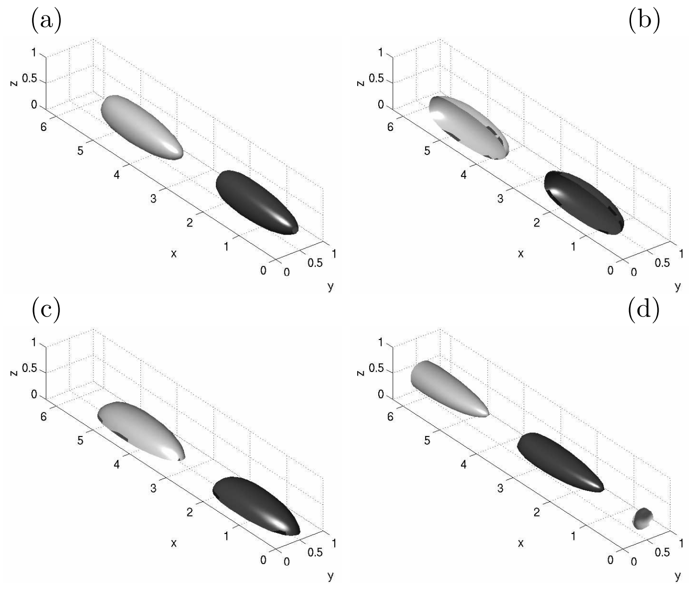

Figure 5.16: As figure 5.15, but showing iso-surfaces of (a) u, (b) v, (c) w, (d) ϕ at ± 0.5 of the respective maximum values. Note that the second quadrant of the (y,z)-cross-section is shown.

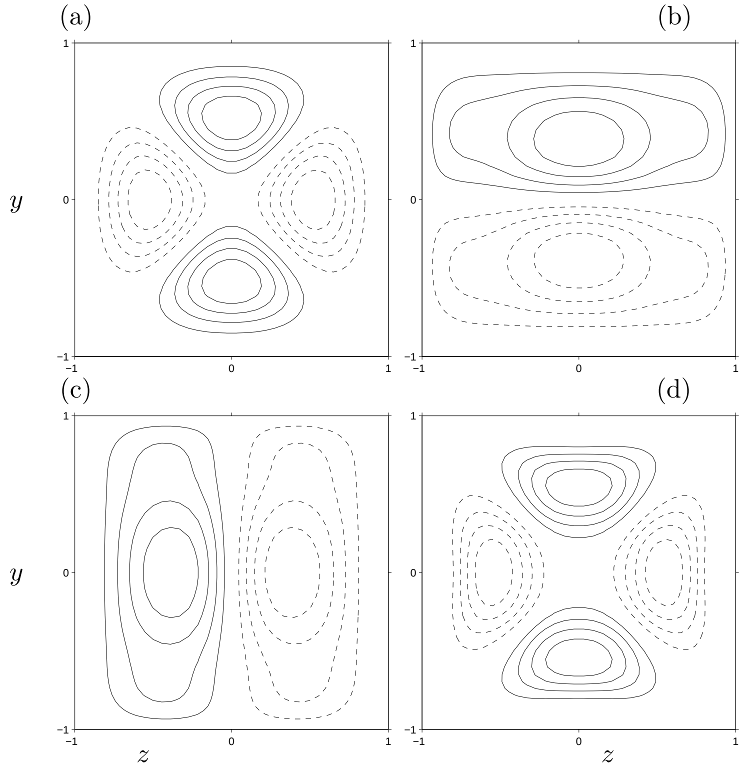

Figure 5.17: As figure 5.13, but showing mode III. The complex phase velocity for this disturbance is: $c = -87.723 + 1.249\, I$.

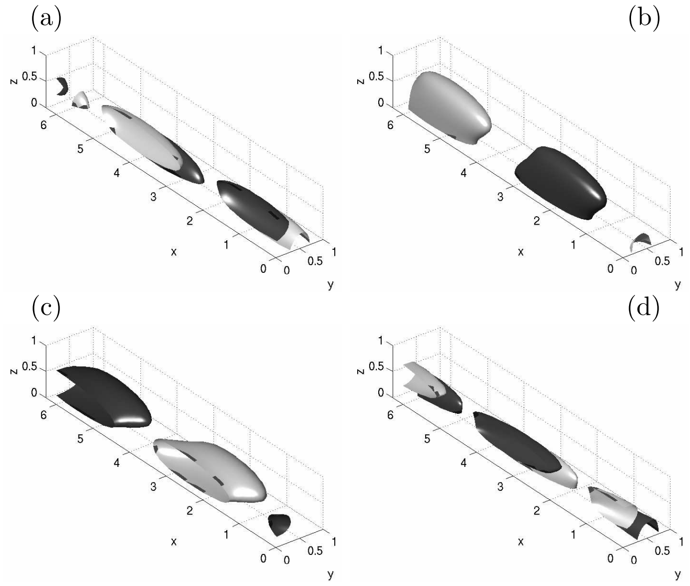

Figure 5.18: As figure 5.17, but showing iso-surfaces of (a) u, (b) v, (c) w, (d) ϕ at ± 0.5 of the respective maximum values. Note that the second quadrant of the (y,z)-cross-section is shown.

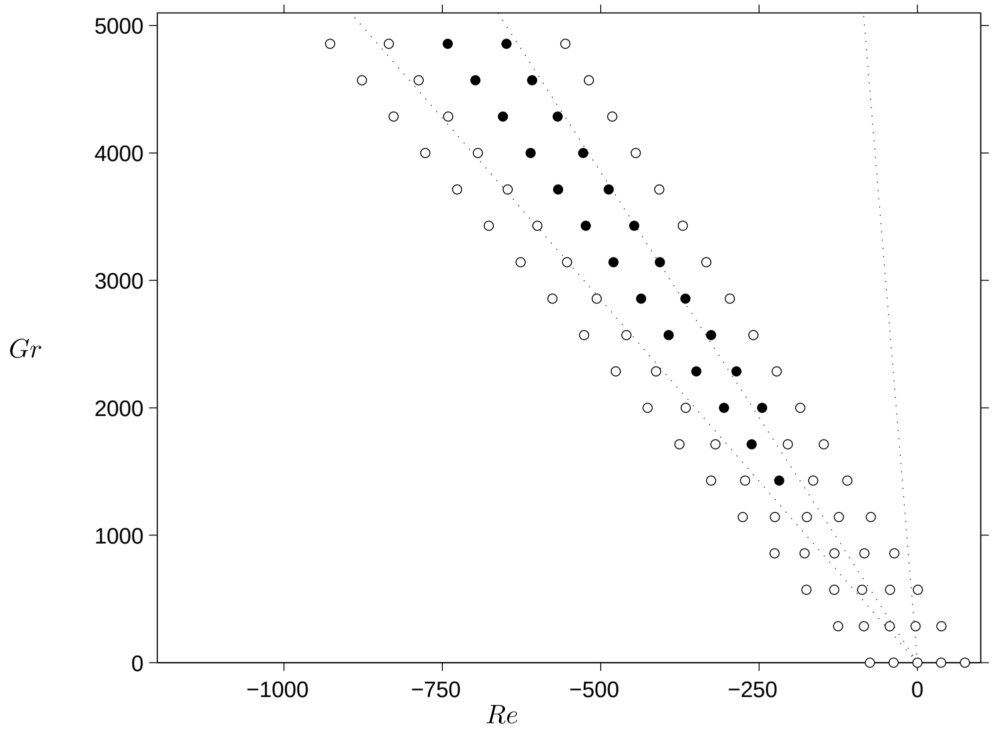

Figure 5.19: As figure 5.10, but for $Pr = 3$ and a truncation level of $N_y = N_z = 20$.

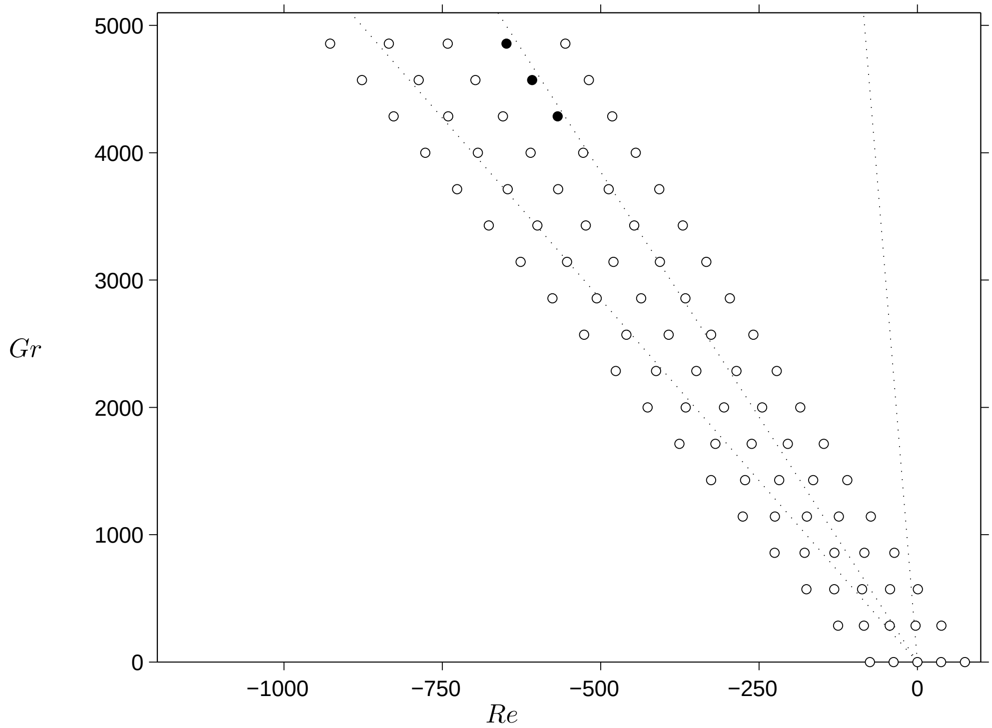

Figure 5.20: As figure 5.10, but for $Pr = 0.71$ and a truncation level of $N_y = N_z = 20$.

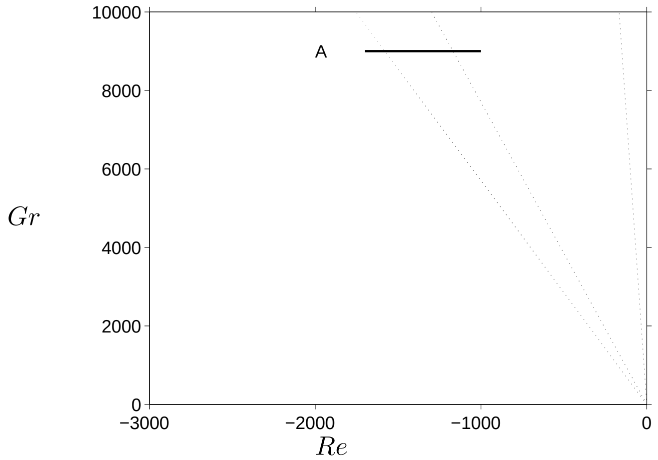

Figure 5.21: Diagram of (Gr,Re)-space indicating the bounds of the inflectional regions and the range of the sweep (marked “A”) performed in figure 5.22.

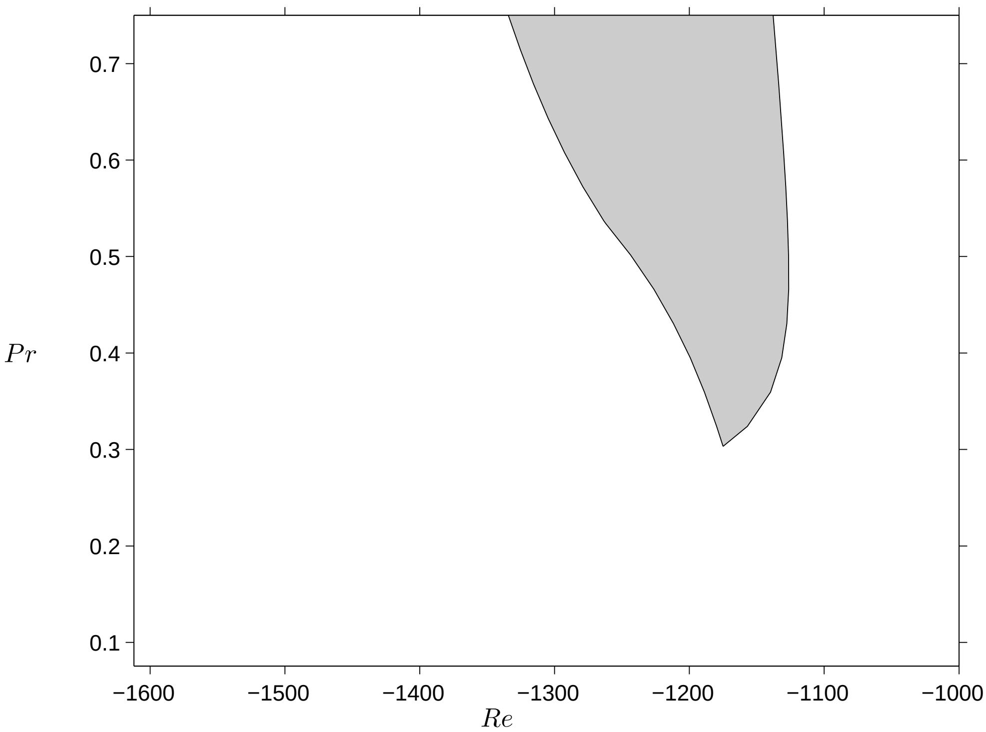

Figure 5.22: Neutral curve (the unstable region is shaded) for the square duct $A = 1$ at $\alpha = 1$ and high Grashof number $Gr = 9000$ in the (Pr, Re)-plane. Only mode I is unstable. This combination of values for the Reynolds and Grashof numbers corresponds to the line marked “A” in figure 5.21.

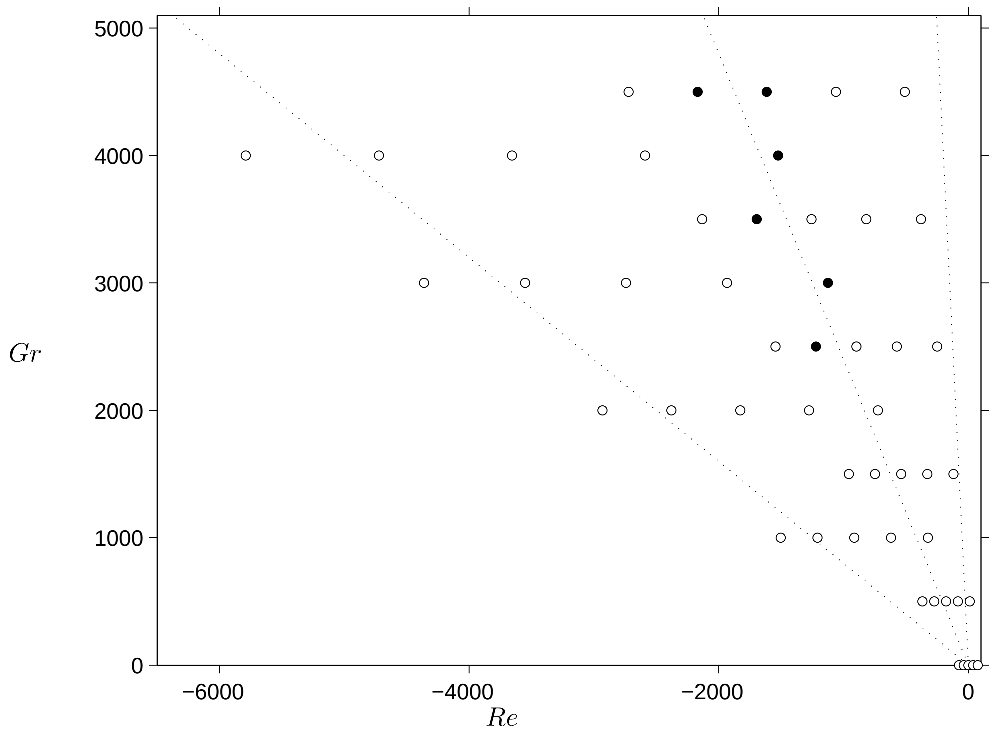

Figure 5.23: Stability diagram in the Gr-Re-plane for aspect ratio $A = 4$ and streamwise wavenumber $\alpha = 1$ at $Pr = 7$ and considering the symmetry mode I; the truncation level being $N_y = 20$, $N_z = 30$. Solid circles refer to positive or zero growth rate, open symbols to negative growth. The straight dotted lines correspond to the bounds of the appearance of additional inflection lines and reverse flow, respectively. Please note the different scale w.r.t. the plots in figures 5.10, 5.19, 5.20.

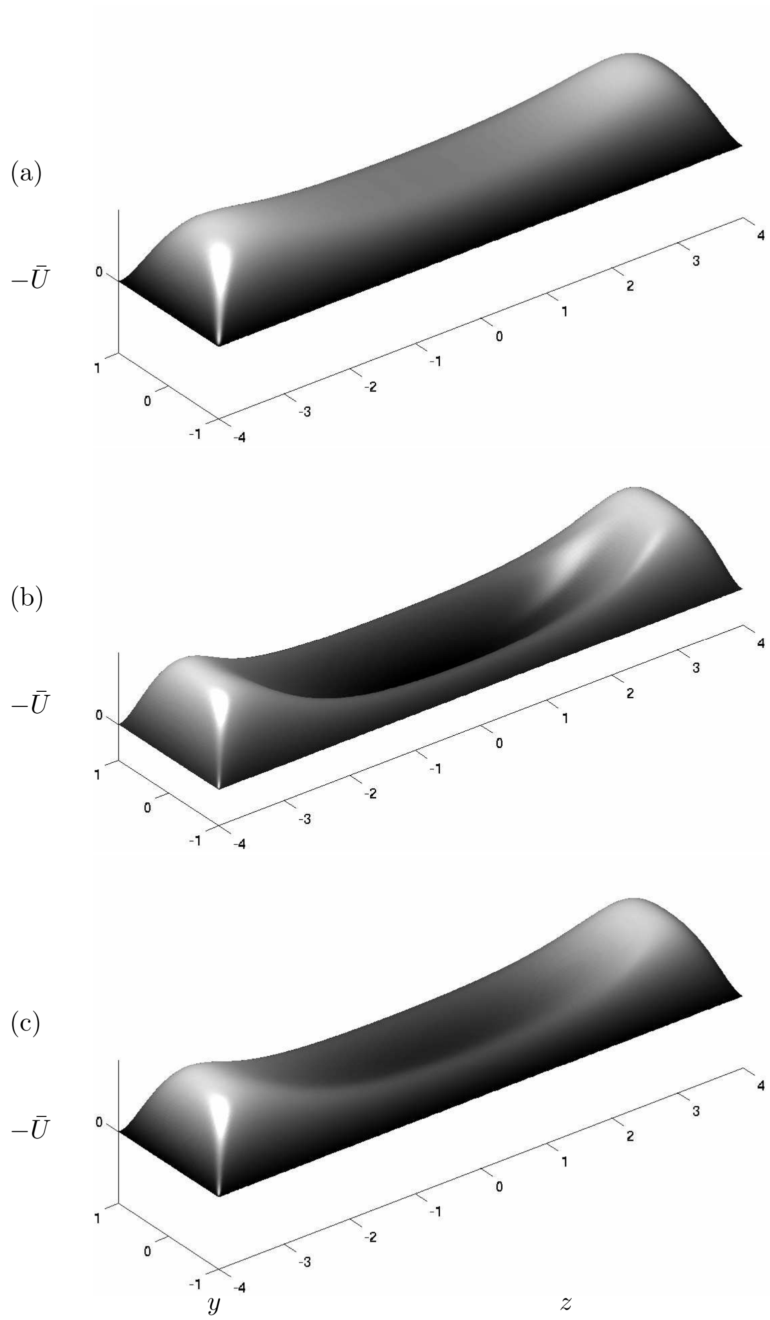

Figure 5.24: Mean flow for $A = 4$: (a) $Gr = 1479$ and $Re = -714.3$; $-178.004 \leq \bar{U} \leq 0$; 7 disjoint inflection lines; (b) $Gr = 3621$ and $Re = -1429$; $-219.515 \leq \bar{U} \leq 56.322$; 17 disjoint inflection lines; (c) $Gr = 5050$ and $Re = -2143$; $-400.124 \leq \bar{U} \leq 0$; 9 disjoint inflection lines.

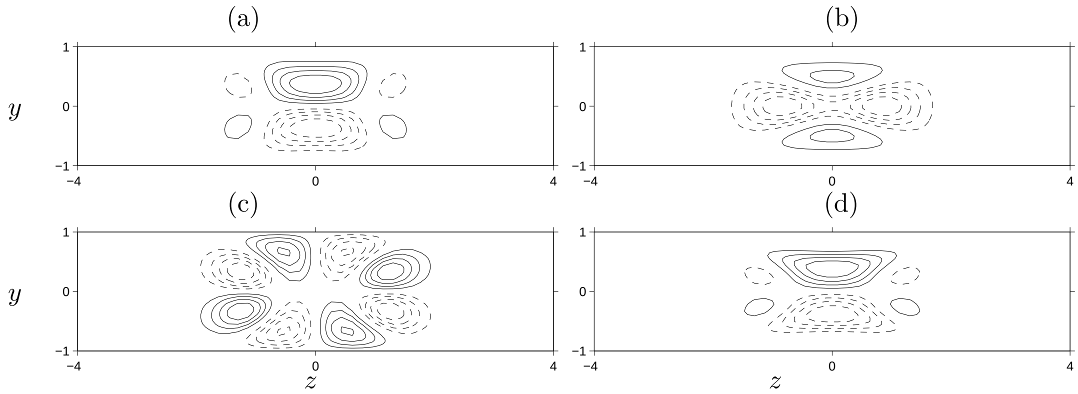

Figure 5.25: Uniformly-spaced isocontours (negative values dashed) of the normalized eigenfunction at arbitrary phase corresponding to the following parameter point: $A = 4$, $Pr = 7$, $Gr = 1479$, $Re = -714.3$, $\alpha = 1$, mode I. The complex phase velocity for this disturbance is: $c = -112.061 + 1.408\,I$. The different graphs show (a) u, (b) v, (c) w, (d) θ.

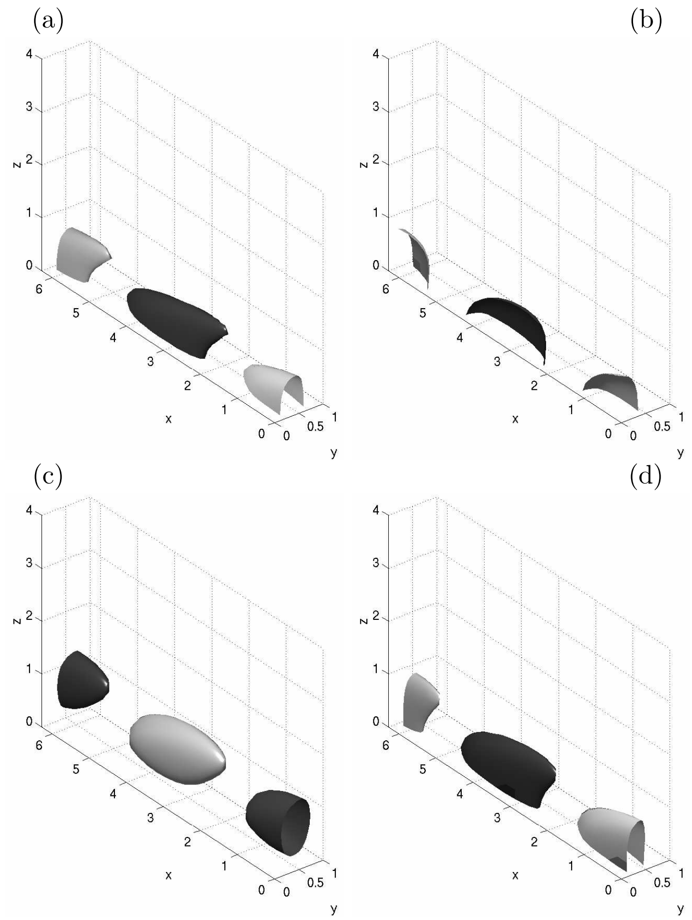

Figure 5.26: As figure 5.25, but showing iso-surfaces of (a) u, (b) v, (c) w, (d) ϕ at ± 0.5 of the respective maximum values. Note that the second quadrant of the (y,z)-cross-section is shown.

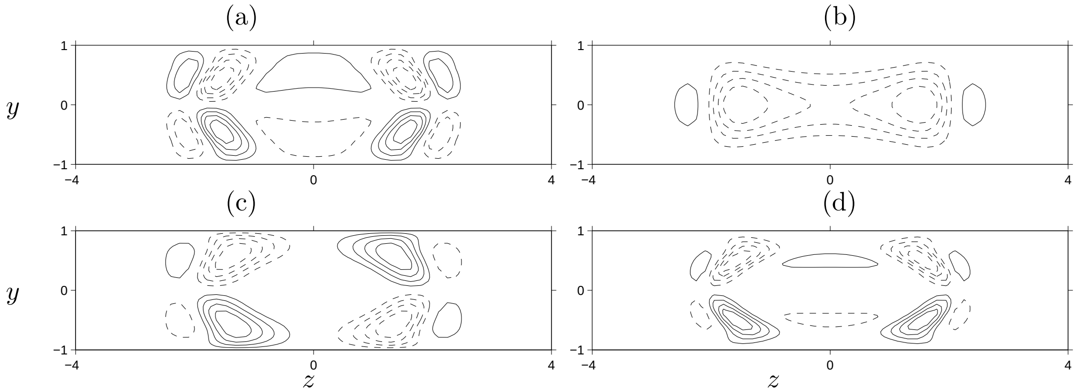

Figure 5.27: Uniformly-spaced isocontours (negative values dashed) of the normalized eigenfunction at arbitrary phase corresponding to the following parameter point: $A = 4$, $Pr = 7$, $Gr = 3621$, $Re = -1429$, $\alpha = 1$, mode I. The complex phase velocity for this disturbance is: $c = -49.908 + 10.020\,I$. The different graphs show (a) u, (b) v, (c) w, (d) θ.

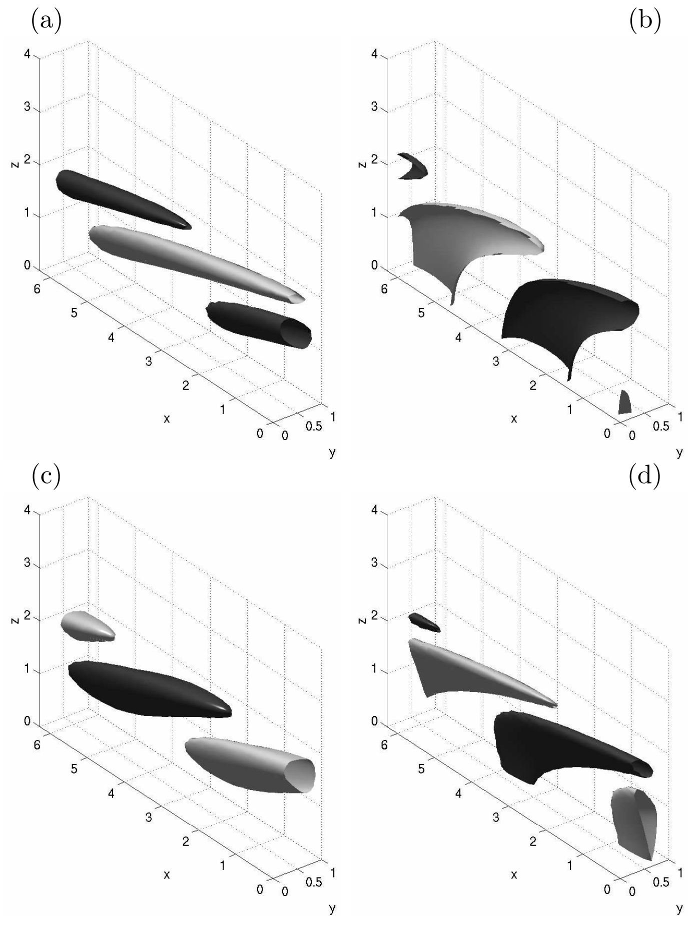

Figure 5.28: As figure 5.27, but showing iso-surfaces of (a) u, (b) v, (c) w, (d) ϕ at ± 0.5 of the respective maximum values. Note that the second quadrant of the (y,z)-cross-section is shown.

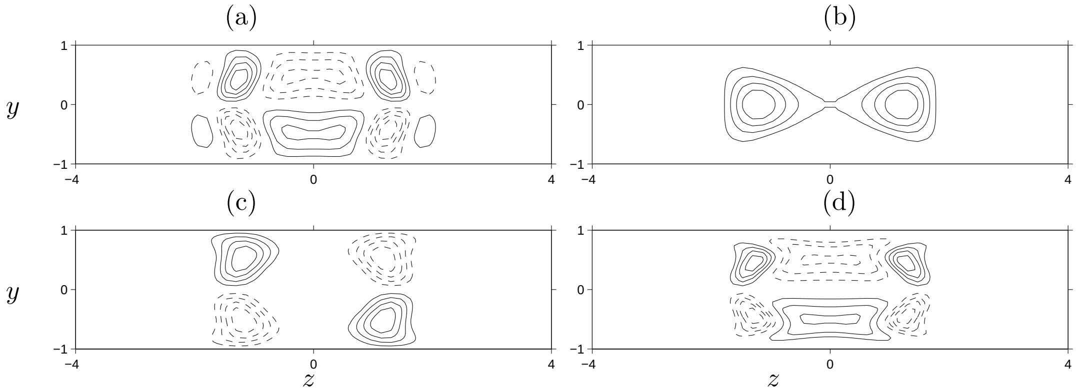

Figure 5.29: Uniformly-spaced isocontours (negative values dashed) of the normalized eigenfunction at arbitrary phase corresponding to the following parameter point: $A = 4$, $Pr = 7$, $Gr = 5050$, $Re = -2143$, $\alpha = 1$, mode I. The complex phase velocity for this disturbance is: $c = -146.833 + 12.349\,I$. The different graphs show (a) u, (b) v, (c) w, (d) θ.

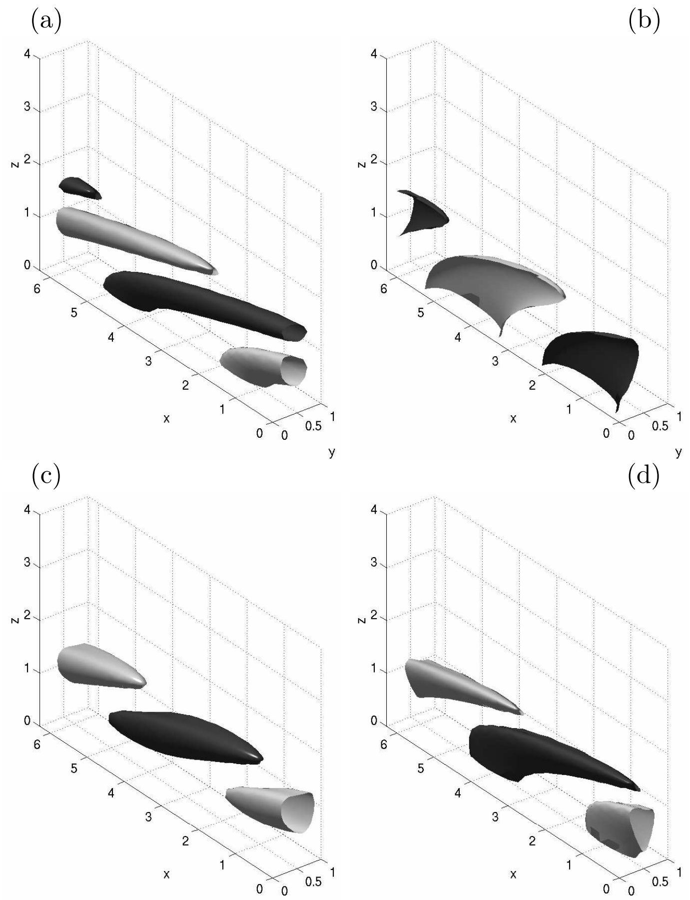

Figure 5.30: As figure 5.29, but showing iso-surfaces of (a) u, (b) v, (c) w, (d) ϕ at ± 0.5 of the respective maximum values. Note that the second quadrant of the (y,z)-cross-section is shown.

Appendix A

Mean flow for the isothermal case

The relation between the pressure gradient and the maximum velocity can be obtained by considering the mean flow for pure convection (cf. [5]), which is the solution of the following Poisson equation:

$$\partial_{\hat{y}\hat{y}}\hat{u} + \partial_{\hat{z}\hat{z}}\hat{u} = \frac{1}{\hat{\rho}\hat{\nu}}\partial_{\hat{x}}\hat{p} = cst. \tag{A.1}$$

Due to the linearity of the operator, the solution can be simply rescaled and we can write $\hat{u} = \hat{U}_{max}\, g(\hat{y},\hat{z})$, where $\hat{U}_{max}$ is the maximum mean velocity and $\max_{y,z}(g(\hat{y},\hat{z})) = 1$. The non-dimensional function $g(\hat{y},\hat{z})$ can simply be obtained from a solution of the Poisson problem $\partial_{yy}f + \partial_{zz}f = 1$ and subsequent rescaling, viz. $g = f/\max_{y,z}(f)$.

A balance between the wall shear stress and the streamwise pressure gradient in the flow then establishes the desired relation. For the configuration of figure 2.1 and considering a slice with infinitesimal streamwise length, we obtain:

$$\frac{\mathrm{d}\hat{p}}{\mathrm{d}\hat{x}} = \frac{\hat{\tau}_w}{4\hat{b}\hat{c}}\,, \tag{A.2}$$

where the shear stress can be evaluated as follows:

$$\begin{aligned} \hat{\tau}_w &= -\hat{\rho}\hat{\nu}\hat{U}_{max}\left\{\int_{-c}^{+c}\left([\partial_{\hat{y}}\hat{g}]_{\hat{y}=-\hat{b}} - [\partial_{\hat{y}}\hat{g}]_{\hat{y}=+\hat{b}}\right)\mathrm{d}\hat{z} + \int_{-b}^{+b}\left([\partial_{\hat{z}}\hat{g}]_{\hat{z}=-\hat{c}} - [\partial_{\hat{z}}\hat{g}]_{\hat{z}=+\hat{c}}\right)\mathrm{d}\hat{y}\right\}\,, \\ &= -\hat{\rho}\hat{\nu}\hat{U}_{max}\,\chi(A)\,. \end{aligned} \tag{A.3}$$

The dimensionless function χ depends only on the aspect ratio A of the duct. It can be evaluated from the mean velocity profile for pure pressure-driven convection as given analytically by Rosenhead [5]. We prefer to evaluate it from a numerical solution of the Poisson equation (A.1) by means of a two-dimensional Chebyshev expansion,

$$g(\hat{y},\hat{z}) = \sum_{i,j}\tilde{g}_{ij}\,T_i(\hat{y}/\hat{b})\,T_j(\hat{z}/\hat{c}) \quad . \tag{A.4}$$

Considering that the velocity profile is symmetric with respect to $\hat{y} = 0$ and $\hat{z} = 0$ and using the properties of Chebyshev derivatives at the end-points of the intervals and of Chebyshev integration,

$$T_k'(\pm 1) = (\pm 1)^{k+1}\,k^2\,, \tag{A.5a}$$

$$\int_{-1}^{+1} T_k(x)\mathrm{d}x = \begin{cases} 0 & \text{if} \quad k\ odd \\ \frac{-2}{k^2+1} & \text{if} \quad k\ even\,, \end{cases} \tag{A.5b}$$

we arrive at the following formula for the function $\chi(A)$:

$$\chi(A) = \sum_{\substack{i,j \\ i,j\ even}} \tilde{g}_{ij}\left[\frac{4Ai^2}{(j^2-1)} + \frac{4}{A}\frac{j^2}{(i^2-1)}\right] \quad . \tag{A.6}$$

Appendix B

Transform to modified Chebyshev space

For a function $v(x)$ which has even or odd parity on the interval $[-1,1]$ and which satisfies homogeneous Dirichlet and Neumann conditions we have the following three equivalent representations in terms of Chebyshev polynomials:

$$v(x) = \begin{cases} \sum_{k=0}^{N} \tilde{v}_k \cdot T_{2k}(x) & \text{if } v(x) \text{ even}\,, \\ \sum_{k=0}^{N} \tilde{v}_k \cdot T_{2k+1}(x) & \text{if } v(x) \text{ odd}\,, \end{cases} \tag{B.1}$$

$$v(x) = \begin{cases} \sum_{k=1}^{N} \hat{v}_k \cdot (T_{2k}(x) - T_0(x)) & \text{if } v(x) \text{ even}\,, \\ \sum_{k=1}^{N} \hat{v}_k \cdot (T_{2k+1}(x) - T_1(x)) & \text{if } v(x) \text{ odd}\,, \end{cases} \tag{B.2}$$

$$v(x) = \begin{cases} \sum_{k=2}^{N} \hat{\hat{v}}_k \cdot \big(T_{2k}(x) + (k^2-1)T_0(x) - k^2 T_2(x)\big) & \text{if } v(x) \text{ even}\,, \\ \sum_{k=2}^{N} \hat{\hat{v}}_k \cdot \left(T_{2k+1}(x) + (\frac{k^2+k}{2} - 1)T_1(x) - \frac{k^2+k}{2} T_3(x)\right) & \text{if } v(x) \text{ odd}\,. \end{cases} \tag{B.3}$$

B.1 Forward transform

Using the end-point conditions, i.e. $v(x = \pm 1) = v'(x = \pm 1) = 0$, the following identities can be shown:

$$\begin{aligned} \hat{v}_k &= \tilde{v}_k & \forall \quad k = 1, \ldots, N\,, \\ \hat{\hat{v}}_k &= \hat{v}_k = \tilde{v}_k & \forall \quad k = 2, \ldots, N\,. \end{aligned} \tag{B.4}$$

This means that a forward transform from physical space (v) to modified space ($\hat{\hat{v}}$) consists of a classical Chebyshev transform ($v \to \tilde{v}$) and then a simple deletion of the first two elements ($\tilde{v} \to \hat{v} \to \hat{\hat{v}}$).

B.2 Backward transform

During the back-transform, we need to reconstruct the deleted coefficients, viz:

$$\begin{aligned}
\hat{v}_1 &= \begin{cases} -\sum_{k=2}^{N} \hat{\hat{v}}_k \cdot k^2 & \text{if } v(x) \text{ even}\,, \\ \sum_{k=2}^{N} \hat{\hat{v}}_k \left(\dfrac{1-(2k+1)^2}{8} \right) & \text{if } v(x) \text{ odd}\,, \end{cases} \\
\tilde{v}_0 &= -\sum_{k=1}^{N} \hat{v}_k \,.
\end{aligned} \tag{B.5}$$

It should be noted that in the present case of a two-dimensional transform, i.e. $v(y,z) \to \tilde{v}_{ij} \to \hat{v}_{ij} \to \hat{\hat{v}}_{ij}$, additional care needs to be taken that the reconstructed "constant mode" satisfies:

$$\tilde{v}_{00} = -\sum_{i=1}^{N_y} \sum_{j=0}^{N_z} \tilde{v}_{ij} - \sum_{j=1}^{N_z} \tilde{v}_{0j} \,. \tag{B.6}$$

which ensures that $v(\pm 1, \pm 1) = 0$.

Appendix C

Further details of the collocation method

C.1 Transform and derivative matrices

Suppose we have a variable which satisfies $v(x=\pm 1) = v'(x=\pm 1) = 0$ and has either even or odd symmetry. It is known at the collocation points

$$x_j = \cos(\pi j/(2N+1)) \qquad \forall\ 2 \leq j \leq N\,. \tag{C.1}$$

Its truncated expansion is in terms of the modified Chebyshev series:

$$v(x_j) = \begin{cases} \displaystyle\sum_{k=2}^{N} \hat{\hat{v}}_k \cdot \left(T_{2k}(x_j) + (k^2-1)T_0(x_j) - k^2 T_2(x_j)\right) & \text{if } v(x) \text{ even}\,, \\ \displaystyle\sum_{k=2}^{N} \hat{\hat{v}}_k \cdot \left(T_{2k+1}(x_j) + (\frac{k^2+k}{2} - 1)T_1(x_j) - \frac{k^2+k}{2} T_3(x_j)\right) & \text{if } v(x) \text{ odd}\,. \end{cases} \tag{C.2}$$

Let us first reconstruct the variable's value at the first interior grid point (x_1) using the end-point conditions and the parity. We have

$$v_{1,N} = R \cdot v_{2,N} \quad , \tag{C.3}$$

where $v_{1,N} = [v(x_1), v(x_2), \ldots, v(x_N)]^T$, $v_{2,N} = [v(x_2), \ldots, v(x_N)]^T$ and R the $N \cdot (N-1)$ matrix with the following entries:

$$\begin{aligned} R_{1,j} &= (D_{\tilde{N}})_{0,j} \cdot (D_{\tilde{N}})_{\tilde{N},1} - (D_{\tilde{N}})_{\tilde{N},j} \cdot (D_{\tilde{N}})_{0,1} \\ &\quad \pm \left((D_{\tilde{N}})_{0,\tilde{N}-j} \cdot (D_{\tilde{N}})_{\tilde{N},1} - (D_{\tilde{N}})_{\tilde{N},\tilde{N}-j} \cdot (D_{\tilde{N}})_{0,1}\right) \quad \forall\ 2 \leq j \leq N \qquad \text{(C.4a)} \\ R_{i,j} &= \delta_{i,j} \quad \forall\ 2 \leq i \leq N\,, \quad 2 \leq j \leq N \qquad \text{(C.4b)} \end{aligned}$$

where $(D_N)_{i,j}$ is an element of the standard Chebyshev-Gauss-Lobatto first-derivative matrix [14, p.69] and we have used $\tilde{N} = 2N+1$. The "+"-sign in equation (C.4a) corresponds to v even, the negative sign to an odd function.

Next, using $v_{1,N}$ (and knowing that $v(x_0) = 0$) we can determine the $N+1$ coefficients of the series of odd/even Chebyshev polynomials

$$v(x_j) = \begin{cases} \displaystyle\sum_{k=0}^{N} \tilde{v}_k \cdot T_{2k}(x_j) & \text{if } v(x) \text{ even} \\ \displaystyle\sum_{k=0}^{N} \tilde{v}_k \cdot T_{2k+1}(x_j) & \text{if } v(x) \text{ odd} \end{cases} \tag{C.5}$$

as follows:

$$\tilde{v}_{0,N} = P \cdot v_{1,N} \quad , \tag{C.6}$$

with the transform matrix P given by

$$P_{kj} = \frac{2}{(2N+1)\bar{c}_{\tilde{k}}} \cos\left(\frac{\pi j \tilde{k}}{2N+1}\right) \quad \forall\, 0 \le k \le N\,, \quad 1 \le j \le N \quad , \tag{C.7}$$

and

$$\tilde{k} = \begin{cases} 2k & \text{if } v \text{ even} \\ 2k+1 & \text{if } v \text{ odd} \end{cases} \quad , \tag{C.8}$$

and

$$\bar{c}_k = \begin{cases} 1 & \text{if} \quad k = 0, 2N+1 \\ 2 & \text{if} \quad 1 \le k \le 2N \end{cases} \quad . \tag{C.9}$$

In a further step we can compute the desired order-α derivative at selected collocation points, viz.

$$v^{(\alpha)}_{j_f,N} = S^{(\alpha)}_{j_f,N} \cdot \tilde{v}_{0,N}\,, \tag{C.10}$$

for evaluation at all collocation points x_j in the range $j_f \le j \le N$. Here, $S^{(\alpha)}_{j_f,N}$ is a $(N - j_f + 1) \cdot (N+1)$ matrix wich can be computed as follows. Recalling (B.4), we have:

$$v^{(\alpha)}(x_j) = \begin{cases} \displaystyle\sum_{k=2}^{N} \tilde{v}_k \cdot \left(T^{(\alpha)}_{2k}(x_j) + (k^2-1)T^{(\alpha)}_0(x_j) - k^2 T^{(\alpha)}_2(x_j)\right) & \text{if } v(x) \text{ even}\,, \\ \displaystyle\sum_{k=2}^{N} \tilde{v}_k \cdot \left(T^{(\alpha)}_{2k+1}(x_j) + (\frac{k^2+k}{2} - 1)T^{(\alpha)}_1(x_j) - \frac{k^2+k}{2} T^{(\alpha)}_3(x_j)\right) & \text{if } v(x) \text{ odd}\,. \end{cases} \tag{C.11}$$

Therefore, an element of the matrix $S^{(\alpha)}_{j_f,N}$ reads

$$\left(S^{(\alpha)}_{j_f,N}\right)_{jk} = T^{(\alpha)}_{2k}(x_j) + (k^2-1)T^{(\alpha)}_0(x_j) - k^2 T^{(\alpha)}_2(x_j)\,, \tag{C.12}$$

which can be evaluated by referring to the identities given in (D.2) and substituting the present definition of the collocation points (C.1).

Finally, collecting the above sequence of transformations we obtain:

$$v^{(\alpha)}_{j_f,N} = \underbrace{S^{(\alpha)}_{j_f,N} \cdot P \cdot R}_{D_{(\alpha)}} \cdot v_{2,N}\,. \tag{C.13}$$

The matrix called $D_{(\alpha)}$ here corresponds to the derivative matrices in the discretized equation given in the main text (3.12). More specifically, when setting $N = N_y$, $j_f = 2$ and $\alpha = 2$ in (C.13) we obtain matrix D^v_{yy} of the main text. Likewise, $N = N_y$, $j_f = 1$ and $\alpha = 1$ gives $D^{v \to w}_y$, etc. Furthermore, with $N = N_y$, the matrix R given by (C.4) corresponds to $R^{v \to w}_y$ in the main text, and analogously for the remaining reconstruction matrices.

Appendix D

Chebyshev identities

D.1 Identities involving derivatives

Using the recursion formula

$$2T_n(x) = \frac{1}{n+1}\,T'_{n+1}(x) - \frac{1}{n-1}\,T'_{n-1}(x) \quad , \tag{D.1}$$

one can derive the following identities relating the αth derivative of a Chebyshev polynomial to a series of the polynomial:

$$\frac{\partial^\alpha T_n(x)}{\partial x^\alpha} = a \cdot n \cdot \sum_{\substack{k=0 \\ n+k\,\text{condition}}}^{n-\alpha} \frac{T_k(x)}{c_k} \cdot b \quad \forall\, n \geq \alpha \tag{D.2}$$

with the coefficients and the condition of even/oddness of $n+k$ given in table D.1.

D.2 End-point derivatives

$$T_k(\pm 1) = (\pm 1)^k\,, \tag{D.3a}$$

$$T'_k(\pm 1) = (\pm 1)^{k+1} k^2\,, \tag{D.3b}$$

$$T''_k(\pm 1) = (\pm 1)^k\,\frac{k^4 - k^2}{3}\,. \tag{D.3c}$$

α	a	condition	b
1	2	odd	1
2	1	even	$n^2 - k^2$
3	$\frac{1}{4}$	odd	$(k+1+n)(n-1-k)(n-1+k)(n+1-k)$
4	$\frac{1}{24}$	even	$(k+2+n)(k+n)(k+n-2)(k+2-n)(n-k)(k-2-n)$
5	$\frac{1}{192}$	odd	$(n+3-k)(n+3+k)(n+1-k)(n+1+k)(n-1-k)\cdot$ $\cdot(n-1+k)(n-3-k)(n-3+k)$
6	$\frac{1}{1440}$	even	$(n+4-k)(n+4+k)(n+2-k)(n+2+k)(n-k)(n+k)\cdot$ $\cdot(n-2-k)(n-2+k)(n-4-k)(n-4+k)$

Table D.1: Coefficients of the formula (D.2) in the text, relating the αth derivative of a Chebyshev polynomial of order n to a series of the polynomial.

Appendix E

Primitive variable formulation

For the sake of completeness we list the numerical methods which we employed for the solution of the primitive formulation of the linear stability problem (2.24). However, we did not succeed in obtaining physically meaningful solutions. These problems were probably due to the fact that the continuity equation reduces to the trivial condition $0 = 0$ at the four corner points. Subsequently, we chose the v-w formulation of reference [6] (cf. § 2.6) where pressure is eliminated and which has the advantage of a smaller system size.

E.1 Chebyshev collocation method

In the collocation approach, the governing equations are enforced at each of the collocation points of the numerical grid in physical space. Those locations are taken as the Chebyshev-Gauss-Lobatto points, i.e.

$$y_i = \cos\left(\frac{\pi i}{N_y}\right) \quad \forall\, 0 \leq i \leq N_y\,, \quad \eta_j = \cos\left(\frac{\pi j}{N_z}\right) \quad \forall\, 0 \leq j \leq N_z\,, \tag{E.1}$$

and $z_j = A \cdot \eta_j$.

Let us introduce the notation a_N for the matrix of grid-point values of a variable a, with the elements given by $(a_N)_{ij} = a(y_i, z_j)$. Then, the Chebyshev collocation approximation to system (2.24) can be written as follows:

$$I\alpha c u_N = I\alpha \bar{U}_N \boxtimes u_N + \alpha^2 u_N - D_y^2 u_N - \frac{1}{A^2} u_N (D_z^2)^T + (\bar{U}_{,y})_N \boxtimes v_N + (\bar{U}_{,z})_N \boxtimes w_N + I\alpha p_N \tag{E.2a}$$

$$I\alpha c v_N = I\alpha \bar{U}_N \boxtimes v_N + \alpha^2 v_N - D_y^2 v_N - \frac{1}{A^2} v_N (D_z^2)^T + D_y p_N \tag{E.2b}$$

$$I\alpha c w_N = I\alpha \bar{U}_N \boxtimes w_N + \alpha^2 w_N - D_y^2 w_N - \frac{1}{A^2} w_N (D_z^2)^T + \frac{1}{A} p_N (D_z)^T \tag{E.2c}$$

$$0 = I\alpha u_N + D_y v_N + \frac{1}{A} w_N (D_z)^T\,. \tag{E.2d}$$

Here, D_y and D_z are the collocation derivative matrices in the y and z direction given e.g. in [14, p.69] and D_y^2 is the matrix product $D_y \cdot D_y$. $a \boxtimes b$ is the pointwise product of the matrices a,b, i.e. if we set $c = a \boxtimes b$ then the elements are $(c)_{ij} = (a)_{ij} \cdot (b)_{ij}$ (no summation). It is understood that $(\bar{U}_{,y})_N$ is the evaluation of $\bar{U}_{,y}$ at the collocation points.

The system (E.2) is first re-written in the form of a generalized eigenvalue system

$$\mathbf{A}\,\mathbf{q}_N = c\,\mathbf{B}\,\mathbf{q}_N \quad , \tag{E.3}$$

with $\mathbf{q}_N$ the *vector* of all four variables at all collocation points, i.e.

$$\mathbf{q}_N = \left[u(y_0,z_0), u(y_1,z_0), u(y_2,z_0), \ldots u(y_{N_y}, z_{N_z}), v(y_0,z_0), \ldots w(y_0,z_0) \ldots p(y_{N_y}, z_{N_z})\right]^T \quad . \tag{E.4}$$

The system matrices $\mathbf{A}$, $\mathbf{B}$ are of size $(4(N_y+1)\cdot(N_z+1))^2$. Note that the re-shaping of the two-dimensional matrices u_N,v_N,w_N,p_N into the vector $\mathbf{q}_N$ implies that the indexing of the matrix equations (E.2) has to be re-worked in order to construct the matrices $\mathbf{A}$, $\mathbf{B}$.

The boundary conditions are then explicitly written into system (E.3) by setting

$$A_{ij} = \delta_{ij}\,, \quad B_{ij} = 0\,, \quad \forall\, 0 \le j \le (N_y+1)(N_z+1) \tag{E.5}$$

for all lines i corresponding to the variables u,v,w and a collocation point located at $y = \pm 1$ and/or $z = \pm A$.

E.2 Galerkin-tau method

The trial space is given by the mapped two-dimensional Chebyshev series:

$$u(y,z) \;=\; \sum_{i=0}^{N_y}\sum_{j=0}^{N_z} \hat{u}_{ij}\cdot T_i(y)\cdot T_j(\eta(z))\,, \tag{E.6}$$

and analogously for v, w and p. Taking the weighted scalar product of equations (2.24) with the basis functions, i.e.

$$\int_{-1}^{1}\int_{-1}^{1}(2.24)\,\frac{T_i(y)}{\sqrt{1-y^2}}\mathrm{d}y\frac{T_j(\eta)}{\sqrt{1-\eta^2}}\mathrm{d}\eta\,, \quad \forall\ 0\le i\le N_y-2 \quad \cup \quad 0\le j\le N_z-2\,, \tag{E.7}$$

leads to:

$$\begin{aligned}
I\alpha c\sum_{k=0}^{N_y}\sum_{l=0}^{N_z}\hat{u}_{kl}M_{ikjl} \;&=\; \sum_{k=0}^{N_y}\sum_{l=0}^{N_z}\hat{u}_{kl}\left[\alpha^2 M_{ikjl} - K^{2Y}_{ikjl} - \frac{1}{A^2}K^{2Z}_{ikjl} + I\alpha T^0(\bar{U})_{ikjl}\right] && \text{(E.8a)}\\
&\quad + \sum_{k=0}^{N_y}\sum_{l=0}^{N_z}\hat{v}_{kl}T^{1Y}(\bar{U})_{ikjl} + \sum_{k=0}^{N_y}\sum_{l=0}^{N_z}\hat{w}_{kl}\frac{1}{A}T^{1Z}(\bar{U})_{ikjl} + \sum_{k=0}^{N_y}\sum_{l=0}^{N_z}\hat{p}_{kl}I\alpha M_{ikjl}\\
I\alpha c\sum_{k=0}^{N_y}\sum_{l=0}^{N_z}\hat{v}_{kl}M_{ikjl} \;&=\; \sum_{k=0}^{N_y}\sum_{l=0}^{N_z}\hat{v}_{kl}\left[\alpha^2 M_{ikjl} - K^{2Y}_{ikjl} - \frac{1}{A^2}K^{2Z}_{ikjl} + I\alpha T^0(\bar{U})_{ikjl}\right] && \text{(E.8b)}\\
&\quad + \sum_{k=0}^{N_y}\sum_{l=0}^{N_z}\hat{p}_{kl}K^{1Y}_{ikjl}\\
I\alpha c\sum_{k=0}^{N_y}\sum_{l=0}^{N_z}\hat{w}_{kl}M_{ikjl} \;&=\; \sum_{k=0}^{N_y}\sum_{l=0}^{N_z}\hat{w}_{kl}\left[\alpha^2 M_{ikjl} - K^{2Y}_{ikjl} - \frac{1}{A^2}K^{2Z}_{ikjl} + I\alpha T^0(\bar{U})_{ikjl}\right] && \text{(E.8c)}\\
&\quad + \sum_{k=0}^{N_y}\sum_{l=0}^{N_z}\hat{p}_{kl}\frac{1}{A}K^{1Z}_{ikjl}\\
0 \;&=\; I\alpha\sum_{k=0}^{N_y}\sum_{l=0}^{N_z}\hat{u}_{kl}M_{ikjl} + \sum_{k=0}^{N_y}\sum_{l=0}^{N_z}\hat{v}_{kl}K^{1Y}_{ikjl} + \sum_{k=0}^{N_y}\sum_{l=0}^{N_z}\hat{w}_{kl}\frac{1}{A}K^{1Z}_{ikjl}\,, && \text{(E.8d)}
\end{aligned}$$

with $0 \le i \le Ny-2$, $0 \le j \le Nz-2$ (the remaining equations being generated by the boundary conditions). The integrals in the formulation (E.8) have the form of double (M, K^{1Y}, K^{1Z}, K^{2Y}, K^{2Z}) and triple (T^0, T^{1Y}, T^{1Z}) integrals of Chebyshev polynomials. Whereas the former are readily evaluated with the help of the orthogonality property of Chebyshev polynomials, the latter are first reduced to sums of double integrals by the following simple product rule [1]:

$$2\,T_m(x)\,T_n(x) = T_{m+n}(x) + T_{|m-n|}(x)\,, \tag{E.9}$$

before integration. Therefore, the following expressions are obtained for the individual terms:

$$M_{ikjl} = \int_{-1}^{1}\int_{-1}^{1} \frac{T_i(y)T_k(y)}{\sqrt{1-y^2}}\mathrm{d}y\frac{T_j(\eta)T_l(\eta)}{\sqrt{1-\eta^2}}\mathrm{d}\eta = \delta_{ik}\delta_{jl}\frac{c_i c_j \pi^2}{4}\,, \tag{E.10}$$

$$K^{1Y}_{ikjl} = \int_{-1}^{1}\int_{-1}^{1} \frac{T_i(y)T'_k(y)}{\sqrt{1-y^2}}\mathrm{d}y\frac{T_j(\eta)T_l(\eta)}{\sqrt{1-\eta^2}}\mathrm{d}\eta = \delta_{jl}\frac{c_j\pi}{2}\cdot\left\{\begin{array}{lll} \pi k & \text{if} & (i+k)\,odd \\ & & \text{and} \\ & & i \le k-1 \\ 0 & \text{else} & \end{array}\right\}, \tag{E.11}$$

$$K^{1Z}_{ikjl} = \int_{-1}^{1}\int_{-1}^{1} \frac{T_i(y)T_k(y)}{\sqrt{1-y^2}}\mathrm{d}y\frac{T_j(\eta)T'_l(\eta)}{\sqrt{1-\eta^2}}\mathrm{d}\eta = \delta_{ik}\frac{c_i\pi}{2}\cdot\left\{\begin{array}{lll} \pi l & \text{if} & (j+l)\,odd \\ & & \text{and} \\ & & j \le l-1 \\ 0 & \text{else} & \end{array}\right\}, \tag{E.12}$$

$$K^{2Y}_{ikjl} = \int_{-1}^{1}\int_{-1}^{1} \frac{T_i(y)T''_k(y)}{\sqrt{1-y^2}}\mathrm{d}y\frac{T_j(\eta)T_l(\eta)}{\sqrt{1-\eta^2}}\mathrm{d}\eta = \delta_{jl}\frac{c_j\pi}{2}\cdot\left\{\begin{array}{lll} \frac{k(k^2-i^2)\pi}{2} & \text{if} & (i+k)\,even \\ & & \text{and} \\ & & i \le k-2 \\ 0 & \text{else} & \end{array}\right\}, \tag{E.13}$$

$$K^{2Z}_{ikjl} = \int_{-1}^{1}\int_{-1}^{1} \frac{T_i(y)T_k(y)}{\sqrt{1-y^2}}\mathrm{d}y\frac{T_j(\eta)T''_l(\eta)}{\sqrt{1-\eta^2}}\mathrm{d}\eta = \delta_{ik}\frac{c_i\pi}{2}\cdot\left\{\begin{array}{lll} \frac{l(l^2-j^2)\pi}{2} & \text{if} & (j+l)\,even \\ & & \text{and} \\ & & j \le l-2 \\ 0 & \text{else} & \end{array}\right\}, \tag{E.14}$$

$$\begin{aligned} T^0(\bar{U})_{ikjl} &= \sum_{m=0}^{n_y}\sum_{n=0}^{N_z}\hat{\bar{U}}_{mn}\int_{-1}^{1}\int_{-1}^{1} \frac{T_i(y)T_k(y)T_m(y)}{\sqrt{1-y^2}}\mathrm{d}y\frac{T_j(\eta)T_l(\eta)T_n(\eta)}{\sqrt{1-\eta^2}}\mathrm{d}\eta \\ &= \sum_{m=0}^{n_y}\sum_{n=0}^{N_z}\hat{\bar{U}}_{mn}\frac{c_k c_l \pi^2}{16}(\delta_{i+m,k}+\delta_{|i-m|,k})\cdot(\delta_{j+n,l}+\delta_{|j-n|,l})\,, \end{aligned} \tag{E.15}$$

$$\begin{aligned} T^{1Y}(\bar{U})_{ikjl} &= \sum_{m=0}^{n_y}\sum_{n=0}^{N_z}\hat{\bar{U}}_{mn}\int_{-1}^{1}\int_{-1}^{1} \frac{T_i(y)T_k(y)T'_m(y)}{\sqrt{1-y^2}}\mathrm{d}y\frac{T_j(\eta)T_l(\eta)T_n(\eta)}{\sqrt{1-\eta^2}}\mathrm{d}\eta \\ &= \sum_{m=0}^{n_y}\sum_{n=0}^{N_z}\hat{\bar{U}}_{mn}\frac{c_k c_l \pi^2 m}{8}(\delta_{j+n,l}+\delta_{|j-n|,l})\sum_{\substack{s=0\\ s+m\,odd}}^{m-1}\frac{1}{c_s}(\delta_{i+s,k}+\delta_{|i-s|,k})\,, \end{aligned} \tag{E.16}$$

$$\begin{aligned} T^{1Z}(\bar{U})_{ikjl} &= \sum_{m=0}^{n_y}\sum_{n=0}^{N_z}\hat{\bar{U}}_{mn}\int_{-1}^{1}\int_{-1}^{1} \frac{T_i(y)T_k(y)T_m(y)}{\sqrt{1-y^2}}\mathrm{d}y\frac{T_j(\eta)T_l(\eta)T'_n(\eta)}{\sqrt{1-\eta^2}}\mathrm{d}\eta \\ &= \sum_{m=0}^{n_y}\sum_{n=0}^{N_z}\hat{\bar{U}}_{mn}\frac{c_k c_l \pi^2 n}{8}(\delta_{i+m,k}+\delta_{|i-m|,k})\sum_{\substack{s=0\\ s+n\,odd}}^{n-1}\frac{1}{c_s}(\delta_{j+s,l}+\delta_{|j-s|,l})\,, \end{aligned} \tag{E.17}$$

The usual definition for the normalization factor was used:

$$c_i = \left\{\begin{array}{lll} 2 & \text{if} & i=0 \\ 1 & \text{else} & . \end{array}\right. \tag{E.18}$$

The boundary conditions (2.25) need to be reformulated in Chebyshev space. For this purpose, the expansions (E.6) are substituted into (2.25), viz.

$$\sum_{i=0}^{N_y}\sum_{j=0}^{N_z}\hat{\phi}_{ij}\cdot(\pm 1)^i\cdot T_j(\eta) \quad = \quad 0 \tag{E.19a}$$

$$\sum_{i=0}^{N_y}\sum_{j=0}^{N_z}\hat{\phi}_{ij}\cdot(\pm 1)^j\cdot T_i(y) \quad = \quad 0 \tag{E.19b}$$

$$\sum_{i=0}^{N_y}\sum_{j=0}^{N_z}\hat{\phi}_{ij}\cdot(\pm 1)^i\cdot(\pm 1)^j \quad = \quad 0 \tag{E.19c}$$

where ϕ stands for either u, v or w. Note that the third condition (E.19c) imposes the homogeneous Dirichlet value at the four corners. The former two conditions are further transformed by taking the weighted scalar product with $T_k(\eta)$ in the second coordinate direction and $T_k(y)$ in the first direction, respectively. The final result (with $\phi = \{u, v, w\}$) is the following:

$$\sum_{i=0}^{N_y}\hat{\phi}_{ij}(\pm 1)^i \quad = \quad 0 \quad \forall\, 0 \leq j \leq N_z - 2 \tag{E.20a}$$

$$\sum_{j=0}^{N_z}\hat{\phi}_{ij}(\pm 1)^j \quad = \quad 0 \quad \forall\, 0 \leq i \leq N_y - 2 \tag{E.20b}$$

$$\sum_{i=0}^{N_y}\sum_{j=0}^{N_z}\hat{\phi}_{ij}(\pm 1)^i(\pm 1)^j \quad = \quad 0\,. \tag{E.20c}$$

We obtain a generalized eigenvalue system

$$\mathbf{A}\,\hat{\mathbf{q}} = c\,\mathbf{B}\,\hat{\mathbf{q}} \quad , \tag{E.21}$$

by re-arranging the equations (E.6) and (E.20) again in such a way that the vector of unknowns has the following order:

$$\hat{\mathbf{q}} = \left[\hat{u}_{00}, \hat{u}_{10}, \hat{u}_{20}, \ldots \hat{u}_{N_y N_z}, \hat{v}_{00}, \ldots \hat{w}_{00} \ldots \hat{p}_{N_y N_z}\right]^T \quad . \tag{E.22}$$

E.3 Full Galerkin method

The expansion reads:

$$\Phi(y,z) = \sum_{i=i_f}^{N_y}\sum_{j=j_f}^{N_z}\hat{\Phi}_{ij}\cdot B_{ij}^{(\Phi)}(y,\eta(z))\,, \tag{E.23}$$

where Φ stands for either one of the variables u, v, w, p and i_f, j_f are lower index bounds depending on the choice of the basis.

E.3.1 Modified Chebyshev basis

Since the velocity components all fulfill homogeneous Dirichlet conditions at the end-points of each interval direction *and* have either even or odd symmetry, we can represent them by means of a modified Chebyshev basis. Pressure, on the other hand, does not fulfill any *a priori* conditions at the end-points and will therefore be expanded in terms of even or odd Chebyshev polynomials. The table E.1 sums up the base functions used for representing the four variables depending on the soultion mode under consideration. Here we make use of the following one-dimensional basis

	u	v	w	p
mode	$B^u_{ij}(y,\eta(z))$	$B^v_{ij}(y,\eta(z))$	$B^w_{ij}(y,\eta(z))$	$B^p_{ij}(y,\eta(z))$
I	$\phi^{\bar{o}}_i(y)\cdot\phi^{\bar{e}}_j(\eta(z))$	$\phi^{\bar{e}}_i(y)\cdot\phi^{\bar{e}}_j(\eta(z))$	$\phi^{\bar{o}}_i(y)\cdot\phi^{\bar{o}}_j(\eta(z))$	$\phi^{o}_i(y)\cdot\phi^{e}_j(\eta(z))$
II	$\phi^{\bar{o}}_i(y)\cdot\phi^{\bar{o}}_j(\eta(z))$	$\phi^{\bar{e}}_i(y)\cdot\phi^{\bar{o}}_j(\eta(z))$	$\phi^{\bar{o}}_i(y)\cdot\phi^{\bar{e}}_j(\eta(z))$	$\phi^{o}_i(y)\cdot\phi^{o}_j(\eta(z))$
III	$\phi^{\bar{e}}_i(y)\cdot\phi^{\bar{e}}_j(\eta(z))$	$\phi^{\bar{o}}_i(y)\cdot\phi^{\bar{e}}_j(\eta(z))$	$\phi^{\bar{e}}_i(y)\cdot\phi^{\bar{o}}_j(\eta(z))$	$\phi^{e}_i(y)\cdot\phi^{e}_j(\eta(z))$
IV	$\phi^{\bar{e}}_i(y)\cdot\phi^{\bar{o}}_j(\eta(z))$	$\phi^{\bar{o}}_i(y)\cdot\phi^{\bar{o}}_j(\eta(z))$	$\phi^{\bar{e}}_i(y)\cdot\phi^{\bar{e}}_j(\eta(z))$	$\phi^{e}_i(y)\cdot\phi^{o}_j(\eta(z))$

Table E.1: Basis functions for the full Galerkin method, verifying the boundary conditions and the solution parity.

functions:

$$\phi^e_i(x_\alpha) = T_{2i}(x_\alpha) \quad \forall\, 0 \le i \le N_{x_\alpha} \tag{E.24a}$$
$$\phi^{\bar{e}}_i(x_\alpha) = T_{2i}(x_\alpha) - T_0(x_\alpha) \quad \forall\, 1 \le i \le N_{x_\alpha} \tag{E.24b}$$
$$\phi^o_i(x_\alpha) = T_{2i+1}(x_\alpha) \quad \forall\, 0 \le i \le N_{x_\alpha} \tag{E.24c}$$
$$\phi^{\bar{o}}_i(x_\alpha) = T_{2i+1}(x_\alpha) - T_1(x_\alpha) \quad \forall\, 1 \le i \le N_{x_\alpha} \tag{E.24d}$$

with x_α being replaced by either y or z and therefore N_{x_α} by the corresponding N_y or N_z.

Appendix F

Poloidal-toroidal decomposition

We now introduce the poloidal-toroidal decomposition (cf. [21, 22]) of the perturbation field, viz:

$$\mathbf{u}' = \boldsymbol{\delta}\,\phi + \boldsymbol{\epsilon}\,\psi\,. \tag{F.1}$$

The operators $\boldsymbol{\delta}$ and $\boldsymbol{\epsilon}$ are defined as follows:

$$\begin{aligned} \boldsymbol{\delta}(\cdot) &= \nabla\times(\nabla\times\boldsymbol{k}(\cdot)) && \text{(F.2a)}\\ \boldsymbol{\epsilon}(\cdot) &= \nabla\times\boldsymbol{k}(\cdot) && \text{(F.2b)} \end{aligned}$$

which means that the velocity components are given by the following formulas:

$$\mathbf{u}' = (\phi_{,xz}+\psi_{,y}, \phi_{,yz}-\psi_{,x}, -\Delta_2\phi)\,, \tag{F.3}$$

where $\Delta_2 = \partial_{xx}+\partial_{yy}$. The representation of the velocity vector by means of the two scalars ϕ, ψ automatically satisfies the continuity equation. When operating with $\mathbf{k}\cdot\nabla\times(\cdot)$ and $\mathbf{k}\cdot\nabla\times(\nabla\times(\cdot))$ on our perturbation equations (2.19), the pressure-gradient term is eliminated and the following two scalar equations are obtained:

$$\begin{aligned} \partial_t\Delta_2\psi + ADV_\psi &= \nabla^2\Delta_2\psi\,, && \text{(F.4a)}\\ \partial_t\nabla^2\Delta_2\phi + ADV_\phi &= \nabla^4\Delta_2\phi\,. && \text{(F.4b)} \end{aligned}$$

The advection terms take the following form:

$$\begin{aligned} ADV_\psi = {}& \bar{U}\partial_x\Delta_2\psi + (\partial_y\bar{U})(\partial_x(\phi_{,xz}+\psi_{,y}) + \partial_y(\phi_{,yz}-\psi_{,x}))\\ &+(\partial_{yy}\bar{U})(\phi_{,yz}-\psi_{,x}) - (\partial_z\bar{U})(\partial_y\Delta_2\phi) - (\partial_{yz}\bar{U})(\Delta_2\phi)\,, \end{aligned} \tag{F.5}$$

and

$$\begin{aligned} ADV_\phi = {}& \bar{U}(\partial_x\nabla^2\Delta_2\phi) + (\partial_y\bar{U})(2\partial_{xz}(\phi_{,yz}-\psi_{,x}) + 2\phi_{,yyyx}) + (\partial_{yy}\bar{U})(\partial_x\Delta_2\phi)\\ &-(\partial_{zz}\bar{U})(\partial_x\Delta_2\phi) + (\partial_{zy}\bar{U})(2\partial_x(\phi_{,yz}-\psi_{,x}))\,. \end{aligned} \tag{F.6}$$

Please note that the advection terms reduce to the following form if the mean flow is a function of one cross-stream direction only, as it is in plane channel flow with the walls located at $z=\pm 1$ (cf. [8]):

$$\begin{aligned} \underline{\bar{\mathbf{U}} = \mathbf{i}\bar{U}(z)}: \qquad ADV_\psi &= \bar{U}\partial_x\Delta_2\psi - (\partial_z\bar{U})(\partial_y\Delta_2\phi) && \text{(F.7a)}\\ ADV_\phi &= \bar{U}(\partial_x\nabla^2\Delta_2\phi) - (\partial_{zz}\bar{U})(\partial_x\Delta_2\phi) && \text{(F.7b)} \end{aligned}$$

The no-slip boundary conditions on the two sets of side-walls of the rectangular duct are satisfied by the following conditions for the poloidal and toroidal scalars:

$$\begin{array}{llll} \underline{y=\pm 1}: & \phi=0,\quad \phi_{,y}=0,\quad \phi_{,yy}=0, & \underline{z=\pm c/b}: & \phi=0,\quad \phi_{,z}=0,\\ & \psi=0,\quad \psi_{,y}=0, & & \psi=0. \end{array} \tag{F.8}$$

The different number of boundary conditions for the planes of constant y and constant z stem from the fact that equations (F.4) are 6th (4th) order equations for ϕ (ψ) in the x and y direction, but only 4th (2nd) order equations in z.

F.1 Normal mode analysis

Upon substitution of the normal mode expansion

$$\phi(\mathbf{x},t) = \Re\{\Phi(y,z)\exp(I\alpha(x-ct))\}, \tag{F.9a}$$
$$\psi(\mathbf{x},t) = \Re\{\Psi(y,z)\exp(I\alpha(x-ct))\}, \tag{F.9b}$$

into (F.4), the perturbation equations take the following form:

$$\begin{aligned}
&\left\{-I\bar{U}\alpha^3-\alpha^4-I\alpha\bar{U}_{,yy}+\alpha^2\partial_{zz}+2\alpha^2\partial_{yy}+I\alpha\bar{U}\partial_{yy}-\partial_{zzyy}-\partial_{yyyy}\right\}\Psi\\
&\quad+\left\{\alpha^2\bar{U}_{,zy}-\alpha^2\bar{U}_{,y}\partial_z+\alpha^2\bar{U}_{,z}\partial_y-\bar{U}_{,zy}\partial_{yy}+\bar{U}_{,yy}\partial_{zy}\right.\\
&\quad\left.+\bar{U}_{,y}\partial_{zyy}-\bar{U}_{,z}\partial_{yyy}\right\}\Phi = c\left\{-I\alpha^3+I\alpha\partial_{yy}\right\}\Psi
\end{aligned} \tag{F.10a}$$

$$\begin{aligned}
&\left\{I\alpha^3\bar{U}_{,zz}+I\alpha^5\bar{U}-I\alpha^3\bar{U}_{,yy}+\alpha^6-2I\alpha^3\bar{U}_{,y}\partial_y-I\alpha^3\bar{U}\partial_{zz}-2\alpha^4\partial_{zz}\right.\\
&\quad+I\alpha\bar{U}_{,yy}\partial_{yy}-3\alpha^4\partial_{yy}-2I\alpha^3\bar{U}\partial_{yy}-I\alpha\bar{U}_{,zz}\partial_{yy}+2I\alpha\bar{U}_{,zy}\partial_{zy}\\
&\quad+2I\alpha\bar{U}_{,y}\partial_{zzy}+2I\alpha\bar{U}_{,y}\partial_{yyy}+\alpha^2\partial_{zzzz}+I\alpha\bar{U}\partial_{yyyy}+3\alpha^2\partial_{yyyy}\\
&\quad\left.+I\alpha\bar{U}\partial_{zzyy}+4\alpha^2\partial_{zzyy}-\partial_{yyyyyy}-2\partial_{zzyyyy}-\partial_{zzzzyy}\right\}\Phi\\
&\quad+\left\{2\alpha^2\bar{U}_{,zy}+2\alpha^2\bar{U}_{,y}\partial_z\right\}\Psi = c\left\{I\alpha^5-I\alpha^3\partial_{zz}+I\alpha\partial_{yyyy}+I\alpha\partial_{zzyy}-2I\alpha^3\partial_{yy}\right\}\Phi
\end{aligned} \tag{F.10b}$$

Note that the terms enclosed in the second pair of curly brackets on the left-hand-side of both (F.10a) and (F.10b) represent the coupling between Ψ and Φ. The boundary conditions for the two-dimensional functions $\Psi(y,z)$, $\Phi(y,z)$ are:

$$\begin{array}{llll}
\underline{y=\pm 1}: & \Phi=0,\quad \Phi_{,y}=0,\quad \Phi_{,yy}=0, & \underline{z=\pm c/b}: & \Phi=0,\quad \Phi_{,z}=0,\\
 & \Psi=0,\quad \Psi_{,y}=0, & & \Psi=0.
\end{array} \tag{F.11}$$

F.1.1 Bases for a full Galerkin method

The expansion of the variables takes the following form here:

$$\Phi(y,z) = \sum_{i=0}^{N_y-6}\sum_{j=0}^{N_z-4}\hat{\Phi}_{ij}\cdot B_{ij}^{(\Phi)}(y,\eta(z)), \tag{F.12a}$$
$$\Psi(y,z) = \sum_{i=0}^{N_y-4}\sum_{j=0}^{N_z-2}\hat{\Psi}_{ij}\cdot B_{ij}^{(\Psi)}(y,\eta(z)). \tag{F.12b}$$

F.1.1.1 Heinrichs-type Chebyshev basis

The product-technique adapted to our higher order boundary conditions leads to the following basis functions:

$$B_{ij}^{(\Phi)}(y,\eta(z)) = T_i(y)\cdot T_j(\eta)\cdot(1-y^2)^3\cdot(1-\eta^2)^2, \tag{F.13a}$$
$$B_{ij}^{(\Psi)}(y,\eta(z)) = T_i(y)\cdot T_j(\eta)\cdot(1-y^2)^2\cdot(1-\eta^2). \tag{F.13b}$$

F.1.1.2 Shen-type Chebyshev basis

One possiblity for a linear combination of Chebyshev polynomials which satisfies the desired boundary conditions, obtained by using the identities (D.3), is the following:

$$
\begin{aligned}
B_{ij}^{(\Phi)}(y,\eta(z)) &= \left(T_i(y) - \frac{3(i+2)}{i+4}T_{i+2}(y) + \frac{3(i+1)}{i+5}T_{i+4}(y) - \frac{2+3i+i^2}{9i+i^2+20}T_{i+6}(y)\right) \\
&\quad \cdot \left(T_j(\eta) - \frac{2(j+2)}{j+3}T_{j+2}(\eta) + \frac{j+1}{j+3}T_{j+4}(\eta)\right) , \qquad \text{(F.14a)} \\
B_{ij}^{(\Psi)}(y,\eta(z)) &= \left(T_i(y) - \frac{2(i+2)}{i+3}T_{i+2}(y) + \frac{i+1}{i+3}T_{i+4}(y)\right) \cdot \left(T_j(\eta) - T_{j+2}(\eta)\right) . \qquad \text{(F.14b)}
\end{aligned}
$$